BEILSTEIN JOURNAL OF NANOTECHNOLOGY

Superconducting artificial neural networks and quantum circuits

Edited by Anatolie S. Sidorenko

Imprint

Beilstein Journal of Nanotechnology
www.bjnano.org
ISSN 2190-4286
Email: journals-support@beilstein-institut.de

The *Beilstein Journal of Nanotechnology* is published by the Beilstein-Institut zur Förderung der Chemischen Wissenschaften.

Beilstein-Institut zur Förderung der
Chemischen Wissenschaften
Trakehner Straße 7–9
60487 Frankfurt am Main
Germany
www.beilstein-institut.de

BEILSTEIN JOURNAL OF NANOTECHNOLOGY

Transfer function of an asymmetric superconducting Gauss neuron

Fedor A. Razorenov*[1,2], Aleksander S. Ionin[1,2,3], Nikita S. Shuravin[1], Liubov N. Karelina[1], Mikhail S. Sidel'nikov[1], Sergey V. Egorov[1] and Vitaly V. Bol'ginov[1]

Full Research Paper

Open Access

Address:
[1]Osipyan Institute of Solid State Physics RAS, Chernogolovka, Moscow District, 2 Academician Osipyan str., 142432, Russian Federation, [2]Moscow Institute of Physics and Technology, 9 Institutskiy per., Dolgoprudny, Moscow Region, 141701, Russian Federation and [3]Joint Venture Quantum Technologies, 121205, Moscow, Russian Federation

Email:
Fedor A. Razorenov* - razorenov.fa@phystech.edu

* Corresponding author

Keywords:
Josephson interferometers; superconducting neural network; superconductivity

Beilstein J. Nanotechnol. **2025,** *16,* 1160–1170.
https://doi.org/10.3762/bjnano.16.85

Received: 10 March 2025
Accepted: 03 July 2025
Published: 21 July 2025

This article is part of the thematic issue "Superconducting artificial neural networks and quantum circuits".

Guest Editor: A. S. Sidorenko

Abstract

The Gauss neuron is a nonlinear signal converter, whose transfer function (TF) is described by the derivative of some sigmoidal dependence. A superconducting Gauss neuron can be implemented as a two-junction interferometer shunted symmetrically by an additional inductance. This work analyzes three cases of asymmetry that can occur in the experimental samples of Gauss neurons, that is, unequal critical currents of the interferometer's Josephson junctions, asymmetric inductive shunting, and asymmetry of the input signal supply. We illustrate the modifications in equations and the shape of the TF compared to the symmetric case. The analysis performed provides an explanation for the key features observed in a previously conducted experiment.

Introduction

Over the past decade, artificial neural networks have demonstrated their effectiveness and versatility in tasks related to processing large volumes of data, prediction, pattern recognition, and image and video generation. The increasing number of tasks and the growing volume of processed information highlight the relevance of using superconducting elements, which offer the advantages of high clock frequency and energy efficiency [1,2]. Studies [3-6] describe neuromorphic elements based on superconducting interferometers that emulate the signal response of biological neurons in various real-world scenarios. In [1,7-15], adiabatic neuromorphic interferometers were presented, whose energy consumption can be reduced to the fundamental limit of $kT{\cdot}\ln 2$ [16]. These devices contain one or two Josephson junctions (JJs) enclosed in a superconducting loop with three inductive elements. Such devices' design is much simpler than that of a neuromorphic CMOS element, that contains about 20 transistors per cell [7,8], which also speaks in favor of superconducting neuromorphic devices.

The subject of this study is the Gauss neuron [1,7-9,11,12,14], schematically depicted in Figure 1. It consists of three arms connected at a common point O and grounded to a shared electrode (Gnd). Two arms ("Josephson" or "input" ones) each contain a Josephson junction $\mathrm{JJ}_{\mathrm{A,B}}$ and an inductance $L_{\mathrm{A,B}}$, which is also used for receiving input signal. It is assumed that the input arms of the neuron are identical, including equal sensitivity to the input signal. These arms form the two-junction interferometer, and each of them is shunted by the third (output) arm. The latter consists of an inductive element L_{out}, which generates a magnetic flux $\Phi_{\mathrm{out}} = L_{\mathrm{out}} I_{\mathrm{out}}$ when a current I_{out} flows through it (currents in the input arms are denoted as $I_{\mathrm{A,B}}$ in Figure 1). The input signal of the neuron is the magnetic flux Φ_{in}, created using a control line (CL, shown as a dashed line in Figure 1), an external solenoid, or another method. An additional magnetic flux Φ_{b} is also introduced into the neuron, influencing the shape of the neuron's transfer function (TF) [1,12,14].

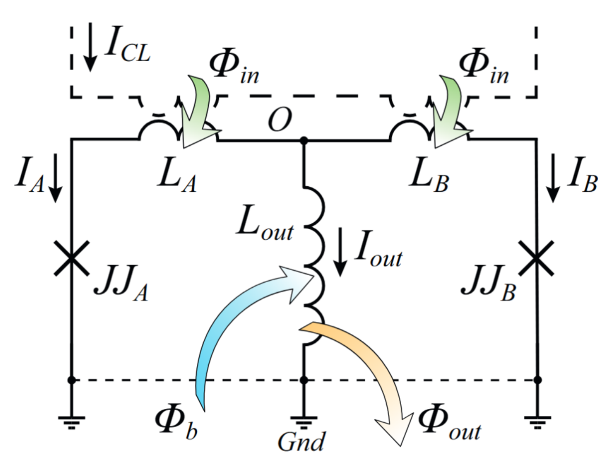

Figure 1: Schematic representation of a Gauss neuron, adapted from [14] (see details in the text).

When developing experimental superconducting neurons [17,18], it is essential to understand how the TF transforms when certain basic assumptions are violated. This can be important for improving device design and diagnosing potential faults. In this work, we consider three possible violations of the equivalence principle ("symmetry") of the input arms of the Gauss neuron. The most expected violation is the imbalance of the critical currents of the JJs, i.e., $I_{\mathrm{cA}} \neq I_{\mathrm{cB}}$. Indeed, during the fabrication of Josephson devices, variations in critical currents of around 5% are observed, even among leading manufacturers [19]. We will refer to this violation as Josephson asymmetry (it can also be called critical current asymmetry or Josephson inductance asymmetry). Another possible violation involves asymmetry in the input arm inductances with $L_{\mathrm{A}} \neq L_{\mathrm{B}}$. This asymmetry may be referred to as "inductive" or "geometric" as it arises from differences in the shape of the input arms due to, for example, defects in the thin-film structure. The third type of asymmetry may be associated with unequal signal supply into the input arms of the neuron. Below, we analyze the transformation of the TF in each of these cases and compare it with experimental results [18].

Symmetric Gauss Neuron

For clarity and systematic exposition, let us first consider the case of a symmetric Gauss neuron [8,12,14]. The equations of state consist of Kirchhoff's law in the node O (Equation 1) and two phase balance equations in the partial loops of the neuron:

$$I_{\mathrm{cA}} \sin \varphi_{\mathrm{A}} + I_{\mathrm{cB}} \sin \varphi_{\mathrm{B}} + I_{\mathrm{out}} = 0, \tag{1}$$

$$\frac{\Phi_0}{2\pi} \varphi_{\mathrm{A}} + L_{\mathrm{A}} I_{\mathrm{cA}} \sin \varphi_{\mathrm{A}} + \Phi_{\mathrm{in}} = \Phi_{\mathrm{out}} + \Phi_{\mathrm{b}}, \tag{2}$$

$$\frac{\Phi_0}{2\pi} \varphi_{\mathrm{B}} + L_{\mathrm{B}} I_{\mathrm{cB}} \sin \varphi_{\mathrm{B}} - \Phi_{\mathrm{in}} = \Phi_{\mathrm{out}} + \Phi_{\mathrm{b}}. \tag{3}$$

Here, $\varphi_{\mathrm{A,B}}$ is the phase difference across the junctions $\mathrm{JJ}_{\mathrm{A,B}}$, $I_{\mathrm{cA,B}}$ are the critical currents, and Φ_0 is the magnetic flux quantum. Equation 2 is written for the left input loop, consisting of the left input and output arms (see Figure 1); Equation 3 is for the loop consisting of the right input and output arms (right input loop). The positive directions of currents (indicated by arrows in Figure 1) and the directions of loop traversal (counterclockwise and clockwise for the left and right loops, respectively) are chosen according to [14]. The phase balance equation for the full input loop, consisting of both input arms, is obtained by subtracting Equation 2–Equation 3. The symmetric case assumes $L_{\mathrm{A}} = L_{\mathrm{B}} = L$ and $I_{\mathrm{cA}} = I_{\mathrm{cB}} = I_{\mathrm{c}}$.

The next step is to adopt dimensionless units: the magnetic flux is normalized by $\Phi_0/2\pi$, the current is normalized by the critical current I_{c}, and the inductance is normalized by the Josephson inductance $L_{\mathrm{J}} = \Phi_0/2\pi I_{\mathrm{c}}$. Thus,

$$\frac{2\pi}{\Phi_0} \Phi_{\mathrm{in}} = \phi_{\mathrm{in}}, \quad \frac{2\pi}{\Phi_0} \Phi_{\mathrm{out}} = \phi_{\mathrm{out}}, \quad \frac{2\pi}{\Phi_0} \Phi_{\mathrm{b}} = \phi_{\mathrm{b}}, \tag{4}$$

$$L / L_{\mathrm{J}} = l, \quad L_{\mathrm{out}} / L_{\mathrm{J}} = l_{\mathrm{out}}, \quad L_{\mathrm{J}} = \Phi_0 / 2\pi I_{\mathrm{c}}. \tag{5}$$

The normalized system of equations takes the form [14]:

$$\sin \varphi_{\mathrm{A}} + \sin \varphi_{\mathrm{B}} + \phi_{\mathrm{out}} / l_{\mathrm{out}} = 0, \tag{6}$$

$$\varphi_A + l\sin\varphi_A + \phi_{in} = \phi_{out} + \phi_b, \tag{7}$$

$$\varphi_B + l\sin\varphi_B - \phi_{in} = \phi_{out} + \phi_b. \tag{8}$$

By solving this system for the input and output fluxes, we obtain the TF of the Gauss neuron $\phi_{out}(\phi_{in})$, which can be written as a two-parameter dependence:

$$\phi_{in} = \frac{\varphi_B - \varphi_A}{2} + \frac{l}{2}\left(\sin\varphi_B - \sin\varphi_A\right), \tag{9}$$

$$\phi_{out} = \frac{\varphi_A + \varphi_B}{2} + \frac{l}{2}\left(\sin\varphi_A + \sin\varphi_B\right) - \phi_b, \tag{10}$$

$$\phi_b = \frac{\varphi_A + \varphi_B}{2} + \left(l_{out} + \frac{l}{2}\right)\left(\sin\varphi_A + \sin\varphi_B\right). \tag{11}$$

Equation 10 and Equation 9 are derived as the sum and the difference of Equation 7 and Equation 8, respectively. Equation 11 is obtained by substituting Equation 10 into Equation 6 to eliminate the output signal ϕ_{out}. By using the common method of introducing half-sum and half-difference of phases [1,8,9,12,14], $\varphi_+ = (\varphi_A + \varphi_B)/2$, $\varphi_- = (\varphi_B - \varphi_A)/2$, the system of Equation 10 and Equation 11 can be represented as:

$$\phi_{in} = \varphi_- + l g_-, \tag{12}$$

$$\phi_{out} = \frac{2l_{out}}{l + 2l_{out}}\left(\varphi_+ - \phi_b\right), \tag{13}$$

$$\frac{\phi_b - \varphi_+}{l + 2l_{out}} - g_+ = 0, \tag{14}$$

where, for brevity, we have introduced the notation $g_\pm = \sin\varphi_\pm\cos\varphi_\mp$. Equation 12 and Equation 13 determine the dependence of the input and output fluxes on the parameters $\varphi_\pm$, while Equation 14 links these parameters. One may also note the linear relationship between the output signal and the mean phase φ_+ according to Equation 13.

The TF (Equation 12–Equation 14) is obviously periodic with respect to ϕ_{in}. Within the first period, the TF of the Gauss neuron represents a symmetric bell-shaped curve that "rests" on a horizontal line (Figure 2a). The symmetry of the TF allows for the use of such neurons in radial basis function networks [20], with the position of the baseline being taken as the zero value of the TF when designing neural networks based on this element. This value can be determined from the system of Equation 12–Equation 14 as the value of ϕ_{out} at zero ϕ_{in}. By symmetry, we obtain $\varphi_- = 0$ according to Equation 12 and

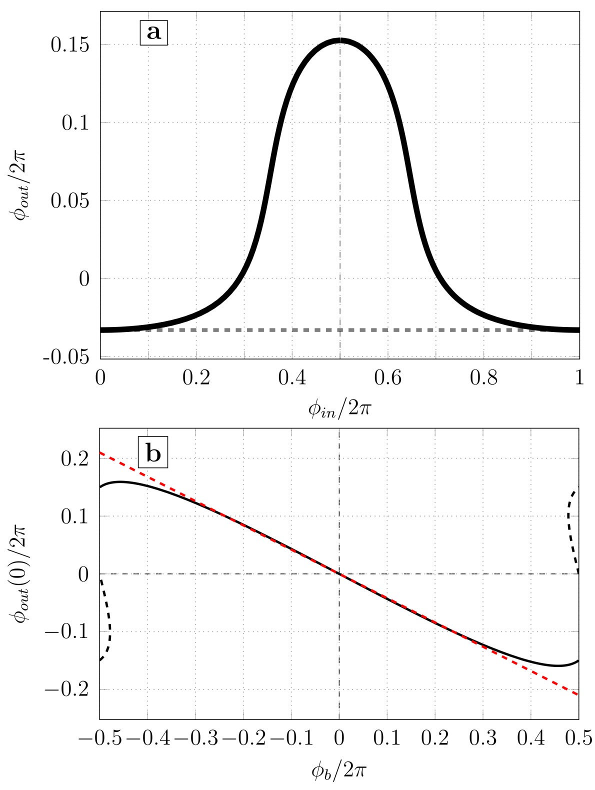

Figure 2: (a) Transfer function of the symmetric Gauss neuron according to Equation 12–Equation 14 for l = 0.29, l_{out} = 0.48, and ϕ_b = 0.155π. The calculation parameters correspond to the experimental work [18]. (b) Dependence of the baseline $\phi_{out}(0)$ on the bias flux ϕ_b for the same sample (solid black line). The red dashed line shows the linear approximation of the central part of the dependence (see discussions in Sections *Symmetric Gauss Neuron* and *Results (C)*). The black dashed line shows the secondary solution that does not provide a bell-shaped response.

$$f\left(\phi_{out}\right) = \frac{\phi_{out}}{2l_{out}} + \sin\left(\phi_b + \frac{l + 2l_{out}}{2l_{out}}\phi_{out}\right) = 0, \tag{15}$$

according to Equation 13 and Equation 14. The solution of this transcendental equation can be represented as a parameterized integral [8]:

$$\phi_{out}(0) = \int_0^{-\pi\,\mathrm{sgn}\,\phi_b} \theta\left[f\left(\phi_{out}\right)\mathrm{sgn}\left(\phi_b\right)\right]\mathrm{d}\phi_{out}, \tag{16}$$

where $\theta(x)$ is the Heaviside step function. The numerical solution of Equation 15 is shown in Figure 2b. The solution is 2π-periodic, and the dashed black line depicts the secondary branch of the solution that does not allow for a bell-shaped TF and cannot be obtained from Equation 16. Such a solution appears for sufficiently large ϕ_b when $(l + 2l_{out}) > 1$. The calculation parameters correspond to the experimental sample investigated in our previous work [18]. It can be seen that in a sufficiently wide range, the graph is close to linear: deviations from the linear approximation are observed only for sufficiently large $|\phi_b| \gtrsim 0.6\pi$.

Results

A. Josephson asymmetry

Now, let us assume that, for whatever reason, the critical currents of the neuron's JJs have become unequal, $I_{cA} \neq I_{cB}$. First of all, a difficulty arises when introducing dimensionless parameters in the system of Equation 1–Equation 3 as it is unclear which value of $I_{cA,B}$ should be used for normalization in Equation 5. We begin by normalizing the magnetic flux and dividing Equation 2 and Equation 3 (which have the corresponding dimensions) by the quantity $\Phi_0/2\pi$. They will immediately take the normalized form (similar to Equation 7 and Equation 8) if we define

$$l_{A,B} = \frac{L}{L_{J_{A,B}}}, \quad L_{J_{A,B}} = \frac{\Phi_0}{2\pi I_{cA,B}}. \tag{17}$$

Thus, it can be said that in the case of Josephson asymmetry, the system of Equation 1–Equation 3 allows for the normalization of the inductances of the input arms to individual Josephson inductances $L_{J_{A,B}}$. Note that the quantities $l_{A,B}$ can also be introduced in Equation 1. To do this, we multiply it by the inductance L and notice that $LI_{cA,B}\sin\varphi_{A,B}$ are the magnetic fluxes created by the Josephson currents in the elements $L_{A,B}$. Therefore, the resulting equation should also be divided by the unit of magnetic flux $\Phi_0/2\pi$. The normalized system of equations thus takes the form

$$l_A \sin\varphi_A + l_B \sin\varphi_B + \phi_{out} / \tilde{l}_{out} = 0, \tag{18}$$

$$\varphi_A + l_A \sin\varphi_A + \phi_{in} = \phi_{out} + \phi_b, \tag{19}$$

$$\varphi_B + l_B \sin\varphi_B - \phi_{in} = \phi_{out} + \phi_b, \tag{20}$$

where $\tilde{l}_{out} = L_{out} / L$. By performing transformations similar to those in Section *Symmetric Gauss Neuron*, we obtain

$$\phi_{in} = \frac{\varphi_B - \varphi_A}{2} + \frac{1}{2}\left(l_B \sin\varphi_B - l_A \sin\varphi_A\right), \tag{21}$$

$$\phi_{out} = \frac{\varphi_B + \varphi_A}{2} + \frac{1}{2}\left(l_B \sin\varphi_B + l_A \sin\varphi_A\right) - \phi_b, \tag{22}$$

$$\frac{\varphi_B + \varphi_A}{2} + \frac{1 + 2\tilde{l}_{out}}{2}\left(l_B \sin\varphi_B + l_A \sin\varphi_A\right) = \phi_b. \tag{23}$$

The transition to the half-sum and half-difference of phases in Equation 21–Equation 23 naturally exposes the "asymmetry angle" α according to

$$\tan\alpha = \frac{l_A}{l_B} = \frac{I_{cA}}{I_{cB}}. \tag{24}$$

The normalized inductances of the arms are expressed through the asymmetry angle as follows:

$$l_A = \ell \sin\alpha, \quad l_B = \ell\cos\alpha, \quad \ell = \sqrt{l_A^2 + l_B^2}. \tag{25}$$

Thus, the parameter $\ell / \sqrt{2}$ characterizes the effective inductance of the input circuit, and $\tan\alpha$ represents the imbalance of the critical currents. Introducing (φ_+, φ_-) and performing some simple trigonometric transformations, we obtain the two-parameter solution in the form:

$$\phi_{in} = \varphi_- + \frac{\ell}{\sqrt{2}}\left[g_- \cos\tilde{\alpha} - g_+ \sin\tilde{\alpha}\right], \tag{26}$$

$$\phi_{out} = \frac{2\tilde{l}_{out}}{1 + 2\tilde{l}_{out}}\left(\varphi_+ - \phi_b\right), \tag{27}$$

$$\frac{2\tilde{l}_{out}}{1 + 2\tilde{l}_{out}}\left(\varphi_+ - \phi_b\right) + \sqrt{2}\ell\tilde{l}_{out}\left[g_+ \cos\tilde{\alpha} - g_- \sin\tilde{\alpha}\right] = 0. \tag{28}$$

Here, for brevity, we introduce the notation $\tilde{\alpha} = \alpha - \pi/4$. In general, the system of Equation 26–Equation 28 resembles the form of the solution in Equation 12–Equation 14 with the exception of the terms containing $\sin\tilde{\alpha}$. Equation 27 coincides with Equation 13. This is possible because in Equation 22 and Equation 23, the coefficients before the sine terms in the parentheses are the same. Josephson asymmetry leads to the replacement of g_+ and g_- in Equation 12–Equation 14 with linear combinations of the $g_\pm$ terms, as indicated in the square brackets in Equation 26–Equation 28. The functions of Equation 12–Equation 14 and Equation 26–Equation 28 coincide when $\alpha = \pi/4$, which occurs in the symmetric case $I_{cA} = I_{cB}$. The range of variation for the parameter $\tilde{\alpha}$ is $\pm\pi/4$ when, for example, I_{cA} changes within $0 \le I_{cA} < \infty$. Exceeding these limits is possible if one of the Josephson junctions is a π-junction with a negative sign of the current–phase relation (see, for example, [21,22]).

The use of π-junctions in the context of developing adiabatic Josephson logic is discussed, for example, in [23,24].

Figure 3 shows the calculated TF for different cases of Josephson asymmetry. The calculation parameters ($\tilde{l}_{\text{out}}$, l_{B}, ϕ_{b}) were chosen according to the experimental work in [18]. It is assumed that the parameter I_{cA} changes while I_{cB} remains constant. It can be seen that as tanα increases, the curve becomes asymmetric, that is, the left part becomes flatter, and the right one steeper (Figure 3a). For sufficiently large asymmetry ($\tan\alpha \gtrsim 1.4$ for the parameters in Figure 3a), the transfer function becomes multivalued, and hysteresis should be observed during the experiment. In the case of reverse asymmetry (tanα < 1), the right wing of the transfer function becomes flatter (Figure 3b). The baseline remains horizontal ($\phi_{\text{out}}(0) = \phi_{\text{out}}(2\pi)$), but it may intersect the distorted transfer function. Note that a significant distortion of the bell-shaped transfer function is observed when the critical currents diverge by a factor of 1.3 or more, while an asymmetry of the order of 1.05 is unlikely to be noticeable to the naked eye. The difference between Figure 3a and Figure 3b is due to the different meaning of zero and infinite tanα limits: the first one corresponds to the break of the junction JJ_{A}, while the second corresponds to shorting of the junction JJ_{A}. In the first case, the inductance l_{A} turns to infinity and the neuron becomes a single-junction SQUID, whose multistability condition is $(L + L_{\text{out}}) < L_{J_{\text{B}}}$. The screening current circulates mainly in the JJ_{B}–L–L_{out} partial loop. In the case of infinite tanα, the Gauss neuron becomes a shunted single-junction interferometer (in fact, a Sigma neuron [7]), whose multistabitity condition can be expressed as $(L + \text{L}L_{\text{out}}/(L + L_{\text{out}})) < L_{\text{J}}$ (see [13,17]). In that case, the screening current circulates mainly in the JJ_{A}–L–L_{out} circuit, which defines the side the TF is tilted to.

Characterizing the Josephson asymmetry through the ratio of critical currents or the angle α is not the only possible approach. Using the definitions in Equation 24 and Equation 25, we get:

$$\cos\tilde{\alpha} = \sqrt{2}l_{+} / \ell, \quad \sin\tilde{\alpha} = -\sqrt{2}l_{-} / \ell, \qquad (29)$$

where $l_{\pm}$ are defined as:

$$l_{\pm} = \left(l_{\text{B}} \pm l_{\text{A}}\right)/2, \quad l_{\text{A,B}} = l_{+} \mp l_{-}. \qquad (30)$$

Using these definitions (and also the definition of the coefficient $\tilde{l}_{\text{out}}$), the transfer function of the Gauss neuron with Josephson asymmetry takes the form:

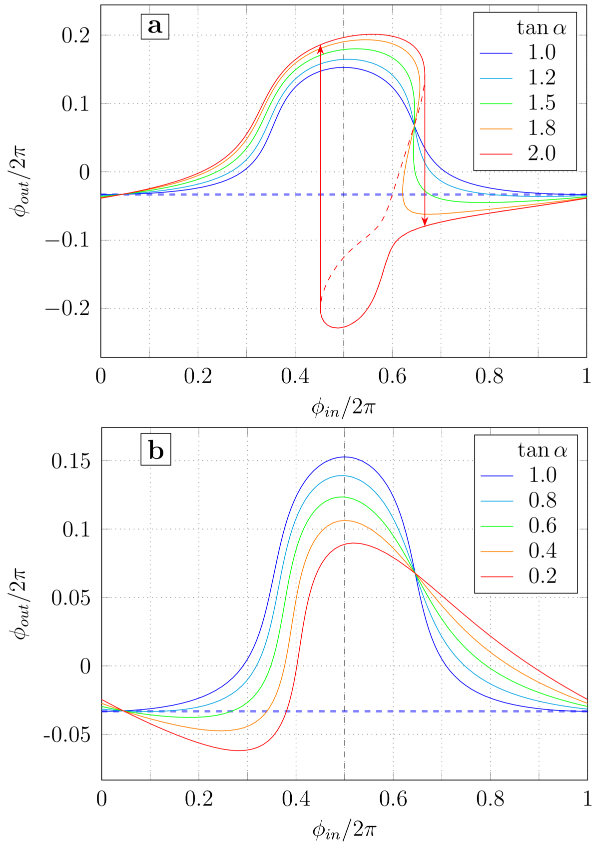

Figure 3: Transfer function of the Gauss neuron according to Equation 26–Equation 28 at different values of the Josephson asymmetry parameter $\tan\alpha = I_{\text{cA}}/I_{\text{cB}}$ for $\tan\alpha \geq 1$ (panel a) and $\tan\alpha \leq 1$ (panel b). The parameters are $\tilde{l}_{\text{out}} = 1.66$, $l_{\text{B}} = 0.29$, and $\phi_{\text{b}} = 0.155\pi$.

$$\phi_{\text{in}} = \left[\varphi_{-} + l_{+}g_{-}\right] + l_{-}g_{+}, \qquad (31)$$

$$\phi_{\text{out}} = \left[\frac{2\tilde{l}_{\text{out}}}{1+2\tilde{l}_{\text{out}}}\left(\varphi_{+} - \phi_{\text{b}}\right)\right], \qquad (32)$$

$$\left[\frac{\phi_{\text{b}} - \varphi_{+}}{1+2\tilde{l}_{\text{out}}} - l_{+}g_{+}\right] - l_{-}g_{-} = 0. \qquad (33)$$

The form of Equation 31–Equation 33 is closest to Equation 12–Equation 14 (the matching terms are highlighted in square brackets). The parameter l_{+} characterizes the effective inductance of the input circuit, while l_{-} represents the imbalance in the normalized inductances of the Josephson circuits. Note the complete coincidence of Equation 13 and Equation 32, which define the linear relationship between the output signal and the sum phase. The influence of Josephson asymmetry reduces to the appearance of conjugate terms of the form $l_{-}g_{\pm}$ in

Equation 12 and Equation 14. The transition to the symmetric case occurs when $l_A = l_B = l_+$, $l_- = 0$.

B. Inductive asymmetry

Now let us consider the case of asymmetry in the self-inductances $L_A \neq L_B$ (“inductive asymmetry”). We will assume that the Josephson inductances are the same: $L_{J_A} = L_{J_B} = L_J$. This allows us to apply the standard normalization of the inductances of the Gauss neuron elements described in Section *Symmetric Gauss Neuron*. The normalized equations of the states described in Equation 1–Equation 3 take the form

$$\sin\varphi_A + \sin\varphi_B + \phi_{out}/l_{out} = 0, \tag{34}$$

$$\varphi_A + l_A\sin\varphi_A + \phi_{in} = \phi_{out} + \phi_b, \tag{35}$$

$$\varphi_B + l_B\sin\varphi_B - \phi_{in} = \phi_{out} + \phi_b. \tag{36}$$

It differs from the “symmetric” system (Equation 6–Equation 8) only by the different values of inductances l_A and l_B in Equation 35 and Equation 36. By adding and subtracting Equation 35 and Equation 36, we obtain the system of equations in the following form:

$$\phi_{in} = \frac{\varphi_B - \varphi_A}{2} + \frac{1}{2}\left(l_B\sin\varphi_B - l_A\sin\varphi_A\right), \tag{37}$$

$$\phi_{out} = \frac{\varphi_B + \varphi_A}{2} - \phi_b + \frac{1}{2}\left(l_B\sin\varphi_B + l_A\sin\varphi_A\right), \tag{38}$$

$$\frac{\varphi_B + \varphi_A}{2} + \left(\left(l_{out} + \frac{l_B}{2}\right)\sin\varphi_B + \left(l_{out} + \frac{l_A}{2}\right)\sin\varphi_A\right) = \phi_b. \tag{39}$$

A transition to phases φ_+ and φ_- is hindered by the fact that the coefficients in front of the Josephson currents $\sin\varphi_{A,B}$ in Equation 39 differ from the coefficients in Equation 37 and Equation 38 (unlike in the system of Equation 21–Equation 23). In this case, using the asymmetry angle appears unreasonable. By introducing the quantities $l_\pm$ according to the definition in Equation 30, we obtain the following system after simple transformations:

$$\phi_{in} = \left[\varphi_- + l_+ g_-\right] + l_- g_+, \tag{40}$$

$$\phi_{out} = \frac{2l_{out}}{l_+ + 2l_{out}}\left(\left[\varphi_+ - \phi_b\right] + l_- g_-\right), \tag{41}$$

$$\left[\frac{\phi_b - \varphi_+}{l_+ + 2l_{out}} - g_+\right] - \frac{l_-}{l_+ + 2l_{out}} g_- = 0. \tag{42}$$

The terms inside square brackets are those present in the “symmetric” system (Equation 12–Equation 14). Note that in the case of inductive asymmetry, the linear relationship between ϕ_{out} and φ_+ is not preserved (unlike in the Josephson asymmetry case). The condition relating the parameters of the phase differences $\varphi_\pm$ is also different (compared to the system of Equation 31–Equation 33). The symmetric case is obtained when $l_A = l_B = l_+$, and $l_- = 0$.

Figure 4 shows the family of transfer functions for different values of l_A/l_B. The calculation parameters (l_B, l_{out}, ϕ_b) correspond to the sample studied experimentally in [18]. It is assumed that L_A changes while L_B remains constant. As in the previous section, inductive asymmetry causes a tilt of the transfer function, bending one wing of the transfer function and

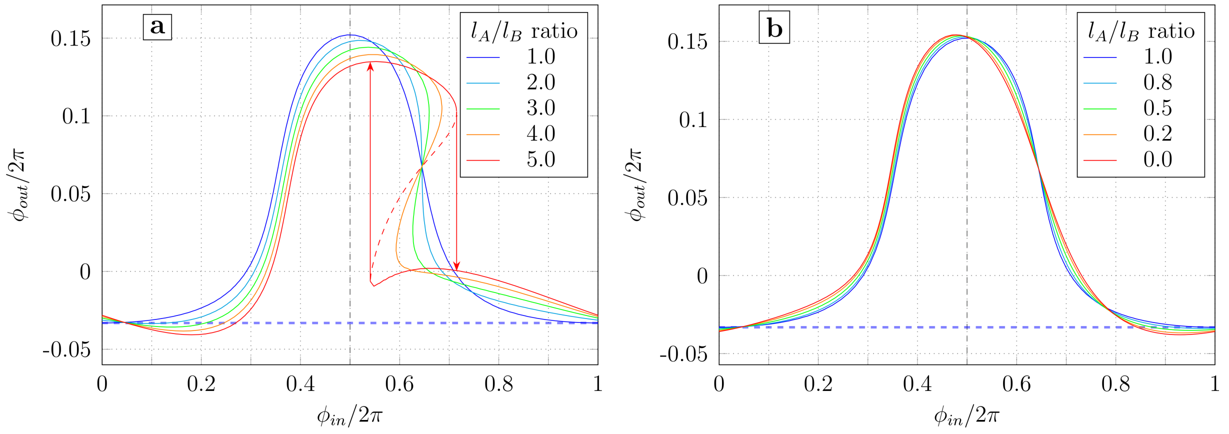

Figure 4: Transfer function of the Gauss neuron with different inductance ratios for the receiving arms (given in the legend) at a constant value of l_B in case of increasing (panel a) or decreasing (panel b) l_A.

widening the other. As l_A/l_B increases, the distortion of the transfer function increases (Figure 4a), which leads to its multivaluedness (and hence to hysteresis). This is related to the increase in the inductance of the overall receiving circuit $2l_+$ as l_A increases. The opposite change (reducing l_A while keeping l_B constant) weakly affects the shape of the transfer function, mainly leading to a slight distortion of the right half of the graph (Figure 4b). The difference between Figure 4a and Figure 4b can be understood by analogy with Josephson asymmetry. Note that all the distortions in Figure 3 and Figure 4 have slightly different shapes, which allows them to be distinguished during the initial analysis of experimental data.

In recent years, a number of superconducting devices have been proposed based on very thin superconducting films whose kinetic inductance may be comparable to the magnetic one [11,25,26]. Indeed, the inductance of a superconducting film carrying an electric current consists of two components, namely, the magnetic inductance (originating from the magnetic field energy) and the kinetic inductance (originating from the kinetic energy of the superconducting electrons). Should one want to account for the kinetic inductance, the initial Equation 1–Equation 3 remain unchanged, as it is the total inductance value that determines the phase balance conditions in Equation 2 and Equation 3. However, the value of ϕ_{out} in Equation 13 has then the meaning of the phase difference across the output arm, which cannot be directly measured in an experiment. The measurable output signal is defined only by the component of ϕ_{out} that originates from the magnetic flux generated by the output current I_{out}. To account for this, one can simply rescale ϕ_{out} in Equation 2 and Equation 3 by the factor $L_{\text{out}}^{(\text{M})}/L_{\text{out}}$, where $L_{\text{out}}^{(\text{M})}$ is the magnetic part of total inductance L_{out}. Therefore, the use of ultrathin superconducting films is not a promising approach for implementing a superconducting Gauss neuron.

C. Input asymmetry

One more possible type of asymmetry is related to the unequal input signal supply to the neuron's receiving arms. To parameterize this asymmetry, we introduce the parameter t, such that the magnetic fluxes in the left and right partial loops of the neuron are $(1 \pm t)\Phi_{\text{in}}$. Then the total flux in the neuron is $2\Phi_{\text{in}}$ (as in previous sections), and $\Phi_{\text{in}} = \Phi_{\text{in}}^{+}$ is simply the half-sum of the input fluxes in the partial loops. The imbalance (half-difference) of the input fluxes is the asymmetry term $\Phi_{\text{in}}^{-} = t\Phi_{\text{in}}^{+}$. In a practical situation, the magnetic flux is supplied into the neuron via a CL, inductively coupled to the receiving elements in some manner. Therefore, input asymmetry effectively means that the mutual inductances $M_{\text{in}}^{\text{A,B}}$ between the CL and the Josephson arms of the neuron are different. In this case, we can express the coefficient t through these inductances. Writing the input fluxes in the partial loops as $\Phi_{\text{in}}^{\text{A,B}} = M_{\text{in}}^{\text{A,B}} I_{\text{CL}}$ (where I_{CL} is the current in the CL), we get

$$t = \frac{\Phi_{\text{in}}^{-}}{\Phi_{\text{in}}^{+}} = \frac{M_{\text{in}}^{\text{A}} - M_{\text{in}}^{\text{B}}}{M_{\text{in}}^{\text{A}} + M_{\text{in}}^{\text{B}}}. \qquad (43)$$

Let us assume that the arms of the neuron are symmetric, meaning that there is no inductive or Josephson asymmetry. Then, the system of equations of state for the Gauss neuron in the standard normalization can be written as

$$l_{\text{out}}\left(\sin\varphi_{\text{A}} + \sin\varphi_{\text{B}}\right) + \phi_{\text{out}} = 0, \qquad (44)$$

$$\varphi_{\text{A}} + l\sin\varphi_{\text{A}} + (1+t)\phi_{\text{in}} = \phi_{\text{out}} + \phi_{\text{b}}, \qquad (45)$$

$$\varphi_{\text{B}} + l\sin\varphi_{\text{B}} - (1-t)\phi_{\text{in}} = \phi_{\text{out}} + \phi_{\text{b}}. \qquad (46)$$

Upon transformations analogous to those made in Section *Symmetric Gauss Neuron*, the first equation of the new system (compare with the system of Equation 12–Equation 14) remains unchanged. The other two acquire new terms proportional to the asymmetry term $t\phi_{\text{in}}$:

$$\phi_{\text{in}} = \left[\varphi_{-} + lg_{-}\right], \qquad (47)$$

$$\phi_{\text{out}} = \left[\frac{2l_{\text{out}}}{l + 2l_{\text{out}}}\left(\varphi_{+} - \phi_{\text{b}}\right)\right] + \frac{2l_{\text{out}}}{l + 2l_{\text{out}}} t\phi_{\text{in}}, \qquad (48)$$

$$\left[\frac{\phi_{\text{b}} - \varphi_{+}}{l + 2l_{\text{out}}} - g_{+}\right] - \frac{1}{l + 2l_{\text{out}}} t\phi_{\text{in}} = 0. \qquad (49)$$

One may note the mixing of the asymmetry term to the output flux according to Equation 47–Equation 49. If $t = 0$, the system of Equation 47–Equation 49 transforms into Equation 12–Equation 14.

The TF plots for different values of the asymmetry parameter t are shown in Figure 5. The calculation parameters (l, l_{out}, ϕ_{b}) correspond to the sample studied experimentally in [18]. For $t = 0$, the TF is a (blue) bell on a horizontal baseline, as demonstrated in Section *Symmetric Gauss Neuron*. However, for nonzero t, the baseline becomes slanted and the transfer function essentially acquires a "linear component". This behavior can be understood by noticing that the input signal is essentially

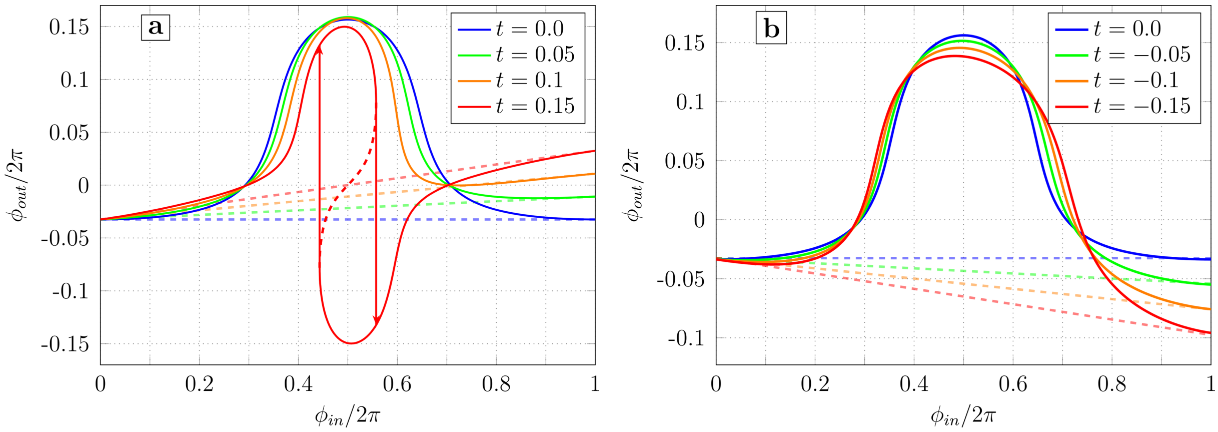

Figure 5: Transfer function of the neuron according to Equation 47–Equation 49 with different imbalance coefficients of the input signal *t* (positive on panel a and negative on panel b). Dashed lines represent the asymptotic baselines.

"mixed" into the bias flux: to obtain Equation 47–Equation 49 from Equation 12–Equation 14, one should make a substitution $\phi_b \rightarrow \phi_b - t\phi_{in}$. This can be seen in Equation 44–Equation 46 by moving the asymmetry terms to the right-hand side. In other words, when ϕ_{in} is swept in the positive direction, the effective bias flux $\tilde{\phi}_b = \phi_b - t\phi_{in}$ (which determines the imbalance of the magnetic flux in the receiving loops ofthe Gauss neuron) decreases for $t > 0$. The decrease in $\tilde{\phi}_b$, in turn, leads to a shift in the TF's baseline value linearly with $\tilde{\phi}_b$ (Figure 2b) for sufficiently small $\tilde{\phi}_b$. Linearity requires correspondingly small t ($|t| \lesssim 0.2$ for Figure 5) since within one period of the input signal, the shift of ϕ_b reaches $2\pi t$.

The increase in the slope of the baseline as t grows (in absolute value) makes the left branch of the transfer function ($\phi_{in} \leq 0.5$) flatter, and the right branch ($\phi_{in} \geq 0.5$) steeper. As t increases, the right branch becomes vertical, and at $t \approx 0.13$, the transfer function becomes hysteretic (see the red curve in Figure 5a). The slope of the linear component is inverted when the sign of t is changed (Figure 5b).

Discussion

All the asymmetry types considered are "independent", meaning they cannot be reduced to one another through algebraic transformations. This statement is evident for input asymmetry, which leads to a slope of the baseline, unlike the other two cases. As for Josephson and inductive asymmetries, the corresponding equations of state (Equation 18–Equation 20 and Equation 34–Equation 36) differ only in the form of the first equation in the system (which originates from Kirchhoff's law) and can be reduced to a common form only in the case $l_A = l_B$ (that is, for a symmetric Gauss neuron). Moreover, the three types of symmetry breaking for the Gauss neuron presented here exhaust the list of possible asymmetries of its arms. Indeed, each receiving arm of the Gauss neuron (Figure 6) is formed by two elements (a JJ and an inductance) and is characterized by three quantities, namely, its own (geometric) inductance, the critical current of the JJ (Josephson inductance), and the sensitivity to the input signal (i.e., mutual inductance with the CL). The fluxes ϕ_{out} and ϕ_b cannot be a direct source of asymmetry in our model, since they are generated through a single element L_{out}, common to both receiving loops. Nevertheless, L_{out} can lead to an effective asymmetry of the input signal supply, as will be shown below.

Let us try to apply the results obtained above to the experimental data presented in our work [18]. The experimental curve (see Figure 6a) represents a flat bell over a slanted baseline, which indicates the presence of input asymmetry. This is surprising because both receiving areas of the Gauss neuron are identical in shape (Figure 6b). However, the effective input asymmetry may arise due to direct interaction of the input and readout elements (which does not involve the neuron as a non-linear converter) as was shown in [27]. Despite the use of a superconducting screen in experiments [17,18], such an interaction can occur due to the finite size of the screen. The interaction is mediated by circulating currents in the screen, which may be non-zero even at a significant distance from the CL [17,28].

To take this effect into consideration, one should consider the method of measuring the output flux Φ_{out} by stabilizing the magnetic flux Φ_{sq} via the measuring SQUID. The latter consists of an inductive element L_{sq}, closed onto a superconducting screen through JJs $JJ_{I,II}$ (an asymmetric two-junction SQUID, Figure 6b). The output signal is the current in the feedback loop of the SQUID I_{fb} that compensates the change in the output flux

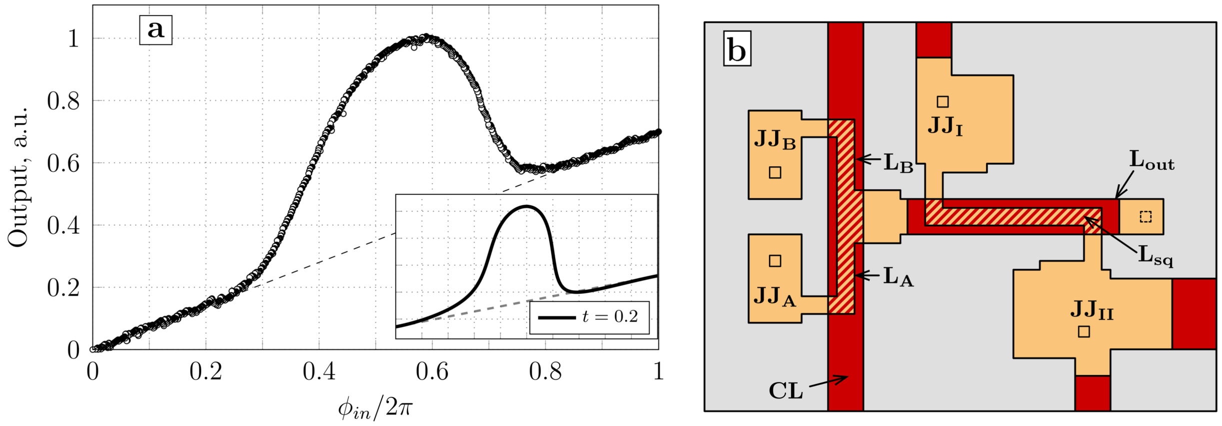

Figure 6: (a) Experimental transfer function of the superconducting Gauss neuron prototype according to [18]. The dashed lines show the baseline (see discussion in Sections *Symmetric Gauss Neuron* and *Results (C)*). The inset shows the calculated TF with $t = 0.2$ and $\phi_b = 0.3\pi$. The dashed lines show the baseline (see discussion in Sections *Symmetric Gauss Neuron* and *Results (C)*). (b) Schematic of the structure of the studied sample. $L_{A,B}$ denote receiving arms, L_{out} is the output arm, $\mathrm{JJ}_{A,B}$ are the JJs of the neuron, $\mathrm{JJ}_{I,II}$ are the JJs of the measuring element (i.e.,SQUID), and L_{sq} is the loop of the measuring element. Different colors represent elements in different layers of the multilayer structure. Hatching indicates the areas of inductive coupling with the input and readout elements. The boundaries of the drawing coincide with the boundaries of the superconducting screen, shown in gray.

while sweeping Φ_{in}. In other words, the current $I_{\text{fb}} = I^{(0)}_{\text{sq}} - I_{\text{sq}}$ represents the difference between the initial and current values of the current flowing through the loop of the measuring element. So, the transfer function of the experimental sample has a somewhat different (“current”) representation compared to the earlier proposed (“flux”) one. The relationship between I_{fb} and Φ_{out} is given by

$$\Phi_{\text{out}} = L_{\text{out}} I_{\text{out}} + M_{\text{out}} \left(I^{(0)}_{\text{sq}} - I_{\text{fb}} \right), \qquad (50)$$

where M_{out} is the mutual inductance between the SQUID and the output element. The variable I_{out} can be eliminated from Equation 50 using the invariance condition for the magnetic flux in the SQUID [17]:

$$\Phi_{\text{sq}} = M_{\text{out}} I_{\text{out}} + L_{\text{sq}} I_{\text{sq}} + M_{\text{sq}} I_{\text{CL}} = \text{const}\left(I_{\text{CL}} \right). \quad (51)$$

After some straightforward transformations, one can obtain:

$$\Phi_{\text{out}} = \frac{L_{\text{sq}} L^{*}_{\text{out}}}{M_{\text{out}}} I_{\text{fb}} + \left[\frac{L_{\text{out}}}{M_{\text{out}}} \Phi_{\text{sq}} - \frac{L_{\text{sq}} L^{*}_{\text{out}}}{M_{\text{out}}} I^{(0)}_{\text{sq}} \right] - \frac{L_{\text{out}} M_{\text{sq}}}{M_{\text{out}}} I_{\text{CL}}, \quad (52)$$

where

$$L^{*}_{\text{out}} = L_{\text{out}} - \frac{M^{2}_{\text{out}}}{L_{\text{sq}}}$$

is the inductance of the output element renormalized due to the interaction with the reading element [17,18,27].

Equation 52 defines the relation between “flux-type” and “current-type” output signals. It is linear but contains three terms. The first one illustrates a linear type of $I_{\text{fb}}(\Phi_{\text{out}})$ dependence. The second one represents a “shift term” that ensures a non-zero value of the bias flux even if $\Phi_b = 0$. This can be verified by substituting Equation 52 into Equation 2 and Equation 3. Note that no special signal line to provide a bias flux into output inductance was realized in the experimental work [18], which, however, did not prevent us from observing a noticeable output signal. However, the effective bias is hard to control during the experiment, so it was estimated as a fitting parameter in [18]. Finally, the third term in Equation 52 arises due to the direct interaction between the input (CL) and readout (SQUID) elements (Equation 51). Upon substitution into Equation 2–Equation 3, the third term will cause the appearance of terms characteristic of input asymmetry with $t = L_{\text{out}}M_{\text{sq}}/M_{\text{out}}M_{\text{in}}$ (with $M_{\text{in}} = M^{A}_{\text{in}} = M^{B}_{\text{in}}$). Substituting further the values $L_{\text{out}} = 7.2$ pH, $M_{\text{sq}} = 0.1$ pH, $M_{\text{out}} = 2.7$ pH, and $M_{\text{in}} = 2.4$ pH given in [17,18], we get $t = 0.2$. Calculations based on Equation 52 give a similar shape of the TF (compared to Figure 6a) at $\phi_b = 0.3\pi$. Thus, experimental results correspond to the expected ones, and a quantitative analysis shall be the subject of our subsequent publications.

The problem with cross-talk mentioned above (i.e., screen-mediated interaction) may become more and more severe when one connects more neurons together. This is why the search for the ways to suppress the cross-talk remains one of the main directions of the neuron's design optimization. It is worth noting that the expression for the t-factor implies that it is possible to change its value by changing L_{out}. However, the change of the output arm's length is not the best way to suppress the input asymmetry. Indeed, the unlimited decrease in L_{out} is impossible at constant values of M_{out} as its length cannot be smaller than the overlap region with the SQUID-sensor loop. Therefore, the t-factor can be just increased with no practical meaning. The most promising ways to dump the effective input asymmetry are the increase of input mutual inductance M_{in} and the suppression of the screen-mediated interaction (a decrease of the M_{sq} value). Some methods of suppressing this interaction are discussed in [26]. The simplest ones include increasing the size of the screen and creating a reverse CL that is not coupled to the neuron (except screen-mediated coupling) and carries the control current in the opposite direction. Calculations show that this decreases M_{sq} by about five times. It is also useful to eliminate sections of the SQUID that are parallel to the CL. This is the main direction of optimization of the Gauss neuron design at the present time.

Conclusion

In this work, the changes in the form of the transfer function (TF) of a Gauss neuron under various violations of the equivalence condition of its receiving loops were investigated. It was shown that the imbalance of the self or Josephson inductances of the neuron's receiving arms leads to a "tilt" in the TF. The distortion of the TF shape in these cases is somewhat different, which provides an opportunity for visual diagnostics of experimental sample faults. The imbalance of the input signal results in the tilting of the baseline, which is not observed in other cases. Comparison with the experiment indicates the presence of input imbalance, which can arise even in a symmetric sample design due to the direct interaction between the input and readout elements.

Acknowledgements

We thank V.N. Shilov and N.S. Stepakov for their help in making the samples and conducting the experiment. Equations 31–33 were obtained by postgraduate students of the Moscow Institute of Physics and Technology (National Research University) A.S. Ionin and F.A. Razorenov within their practical training program. Equation 15, Equation 16 and Figure 2b were obtained as a part of A.S. Ionin's collaboration with "Joint Venture Quantum Technologies".

Funding

The work was carried out at the Osipyan Institute of Solid State Physics, Russian Academy of Sciences, and was supported by the Russian Science Foundation, project no. 23-72-00053.

ORCID® iDs

Fedor A. Razorenov - https://orcid.org/0009-0008-2681-5722
Aleksander S. Ionin - https://orcid.org/0009-0004-0249-1234
Nikita S. Shuravin - https://orcid.org/0009-0004-2612-0366
Liubov N. Karelina - https://orcid.org/0000-0003-4981-6599
Mikhail S. Sidel'nikov - https://orcid.org/0000-0003-2215-6703
Sergey V. Egorov - https://orcid.org/0000-0003-4258-7172
Vitaly V. Bol'ginov - https://orcid.org/0000-0002-6948-7975

Data Availability Statement

All data that supports the findings of this study is available in the published article and/or the supporting information of this article.

References

1. Schegolev, A. E.; Klenov, N. V.; Soloviev, I. I.; Gudkov, A. L.; Tereshonok, M. V. *Nanobiotechnol. Rep.* **2021,** *16,* 811–820. doi:10.1134/s2635167621060227
2. Soloviev, I. I.; Klenov, N. V.; Bakurskiy, S. V.; Kupriyanov, M. Y.; Gudkov, A. L.; Sidorenko, A. S. *Beilstein J. Nanotechnol.* **2017,** *8,* 2689–2710. doi:10.3762/bjnano.8.269
3. Schegolev, A. E.; Klenov, N. V.; Gubochkin, G. I.; Kupriyanov, M. Y.; Soloviev, I. I. *Nanomaterials* **2023,** *13,* 2101. doi:10.3390/nano13142101
4. Skryabina, O. V.; Schegolev, A. E.; Klenov, N. V.; Bakurskiy, S. V.; Shishkin, A. G.; Sotnichuk, S. V.; Napolskii, K. S.; Nazhestkin, I. A.; Soloviev, I. I.; Kupriyanov, M. Y.; Stolyarov, V. S. *Nanomaterials* **2022,** *12,* 1671. doi:10.3390/nano12101671
5. Semenov, V. K.; Golden, E. B.; Tolpygo, S. K. *IEEE Trans. Appl. Supercond.* **2021,** *31,* 1302207. doi:10.1109/tasc.2021.3067231
6. Semenov, V. K.; Golden, E. B.; Tolpygo, S. K. *IEEE Trans. Appl. Supercond.* **2023,** *33,* 1400308. doi:10.1109/tasc.2023.3252495
7. Schegolev, A. E.; Klenov, N. V.; Soloviev, I. I.; Tereshonok, M. V. *Beilstein J. Nanotechnol.* **2016,** *7,* 1397–1403. doi:10.3762/bjnano.7.130
8. Klenov, N. V.; Schegolev, A. E.; Soloviev, I. I.; Bakurskiy, S. V.; Tereshonok, M. V. *IEEE Trans. Appl. Supercond.* **2018,** *28,* 1301006. doi:10.1109/tasc.2018.2836903
9. Soloviev, I. I.; Schegolev, A. E.; Klenov, N. V.; Bakurskiy, S. V.; Kupriyanov, M. Y.; Tereshonok, M. V.; Shadrin, A. V.; Stolyarov, V. S.; Golubov, A. A. *J. Appl. Phys.* **2018,** *124,* 152113. doi:10.1063/1.5042147
10. Klenov, N. V.; Kuznetsov, A. V.; Schegolev, A. E.; Soloviev, I. I.; Bakurskiy, S. V.; Kupriyanov, M. Yu.; Tereshonok, M. V. *Low Temp. Phys.* **2019,** *45,* 769–775. doi:10.1063/1.5111305
11. Bakurskiy, S.; Kupriyanov, M.; Klenov, N. V.; Soloviev, I.; Schegolev, A.; Morari, R.; Khaydukov, Y.; Sidorenko, A. S. *Beilstein J. Nanotechnol.* **2020,** *11,* 1336–1345. doi:10.3762/bjnano.11.118
12. Schegolev, A.; Klenov, N.; Soloviev, I.; Tereshonok, M. *Supercond. Sci. Technol.* **2021,** *34,* 015006. doi:10.1088/1361-6668/abc569
13. Bastrakova, M.; Gorchavkina, A.; Schegolev, A.; Klenov, N.; Soloviev, I.; Satanin, A.; Tereshonok, M. *Symmetry* **2021,** *13,* 1735. doi:10.3390/sym13091735

14. Schegolev, A. E.; Klenov, N. V.; Bakurskiy, S. V.; Soloviev, I. I.; Kupriyanov, M. Y.; Tereshonok, M. V.; Sidorenko, A. S. *Beilstein J. Nanotechnol.* **2022,** *13,* 444–454. doi:10.3762/bjnano.13.37
15. Bastrakova, M. V.; Pashin, D. S.; Rybin, D. A.; Schegolev, A. E.; Klenov, N. V.; Soloviev, I. I.; Gorchavkina, A. A.; Satanin, A. M. *Beilstein J. Nanotechnol.* **2022,** *13,* 653–665. doi:10.3762/bjnano.13.57
16. Takeuchi, N.; Yamanashi, Y.; Yoshikawa, N. *Sci. Rep.* **2014,** *4,* 6354. doi:10.1038/srep06354
17. Ionin, A. S.; Shuravin, N. S.; Karelina, L. N.; Rossolenko, A. N.; Sidel'nikov, M. S.; Egorov, S. V.; Chichkov, V. I.; Chichkov, M. V.; Zhdanova, M. V.; Shchegolev, A. E.; Bol'ginov, V. V. *J. Exp. Theor. Phys.* **2023,** *137,* 888–898. doi:10.1134/s1063776123120191
18. Ionin, A. S.; Karelina, L. N.; Shuravin, N. S.; Sidel'nikov, M. S.; Razorenov, F. A.; Egorov, S. V.; Bol'ginov, V. V. *JETP Lett.* **2023,** *118,* 766–772. doi:10.1134/s002136402360324x
19. Rapid Single Flux Quantum (RSFQ) – Design Rules for Nb/Al2O3-Al/Nb-Process at Leibniz IPHT. https://www.fluxonics.org/foundry/#process (accessed Feb 7, 2025).
20. Orr, M. J. Introduction to radial basis function networks, April 1996, Centre for Cognitive Science, University of Edinburgh, Edinburgh, Scotland. https://faculty.cc.gatech.edu/~isbell/tutorials/rbf-intro.pdf (accessed Feb 7, 2025).
21. Golubov, A. A.; Kupriyanov, M. Y.; Il'ichev, E. *Rev. Mod. Phys.* **2004,** *76,* 411–469. doi:10.1103/revmodphys.76.411
22. Stoutimore, M. J. A.; Rossolenko, A. N.; Bolginov, V. V.; Oboznov, V. A.; Rusanov, A. Y.; Baranov, D. S.; Pugach, N.; Frolov, S. M.; Ryazanov, V. V.; Van Harlingen, D. J. *Phys. Rev. Lett.* **2018,** *121,* 177702. doi:10.1103/physrevlett.121.177702
23. Khismatullin, G. S.; Klenov, N. V.; Soloviev, I. I. *JETP Lett.* **2023,** *118,* 220–229. doi:10.1134/s0021364023601331
24. Soloviev, I. I.; Khismatullin, G. S.; Klenov, N. V.; Schegolev, A. E. *J. Commun. Technol. Electron.* **2022,** *67,* 1479–1491. doi:10.1134/s106422692212021x
25. Neilo, A. A.; Bakurskiy, S. V.; Klenov, N. V.; Soloviev, I. I.; Kupriyanov, M. Yu. *JETP Lett.* **2025,** *121,* 58–66. doi:10.1134/s0021364024604391
26. Luomahaara, J.; Vesterinen, V.; Grönberg, L.; Hassel, J. *Nat. Commun.* **2014,** *5,* 4872. doi:10.1038/ncomms5872
27. Shuravin, N. S.; Karelina, L. N.; Ionin, A. S.; Razorenov, F. A.; Sidel'nikov, M. S.; Egorov, S. V.; Bol'ginov, V. V. *JETP Lett.* **2024,** *120,* 829–836. doi:10.1134/s0021364024603427
28. Ionin, A. S.; Egorov, S. V.; Sidelnikov, M. S.; Karelina, L. N.; Shuravin, N. S.; Khapaev, M. M.; Bolginov, V. V. *Phys. Solid State* **2024,** *66,* 987–993.

License and Terms

BEILSTEIN JOURNAL OF NANOTECHNOLOGY

Modeling magnetic properties of cobalt nanofilms used as a component of spin hybrid superconductor–ferromagnetic structures

Aleksey Fedotov*[1], Olesya Severyukhina[1], Anastasia Salomatina[1,2] and Anatolie Sidorenko[3,4]

Full Research Paper

Open Access

Address:
[1]Modeling Structures and Functional Materials Group, Institute of Mechanics, Udmurt Federal Research Center, Ural Division, Russian Academy of Sciences, Baramzinoy 34, Izhevsk 426067, Russia, [2]Nanotechnology and Microsystems Engineering Department, Kalashnikov Izhevsk State Technical University, Studencheskaya 7, Izhevsk 426069, Russia, [3]Institute of Electronic Engineering and Nanotechnologies, Technical University of Moldova, 3/3 Academiei St., Chisinau, 2028, Moldova and [4]Moscow Institute of Physics and Technology, 9, Institutskiy per., Dolgoprudny, 141701, Russia

Email:
Aleksey Fedotov* - alezfed@gmail.com

* Corresponding author

Keywords:
ferromagnetic properties; LAMMPS; mathematical modeling; MEAM; molecular dynamics; spin dynamics

Beilstein J. Nanotechnol. **2025,** *16,* 1557–1566.
https://doi.org/10.3762/bjnano.16.110

Received: 04 February 2025
Accepted: 08 August 2025
Published: 08 September 2025

Associate Editor: J. M. van Ruitenbeek

Abstract

The paper presents a mathematical model for studying the magnetic behavior of atoms, which takes into account spin and interatomic interactions. Two problems were solved by means of mathematical modeling. At the first stage, the problem of modeling a small nanoscale system (500 atoms) consisting of cobalt atoms was solved. The purpose of this stage of computational experiment was to check the convergence of the solution and compare the obtained data with the results of other studies. The performed calculations and satisfactory correspondence to the previously obtained data confirmed the adequacy of the applied mathematical model. The second stage of numerical studies was devoted to the analysis of the magnetic behavior of cobalt nanofilms of different thicknesses. It was shown that the film thickness has a significant influence on the magnetic parameters of the modeled nanoscale systems. It was found that the magnetic energy and magnetization norm of the system change in a nonlinear manner with increasing number of crystalline layers of the nanofilm. The peaks found on the graph of the magnetization rate change can be caused by surface effects in thin films and the formation of Neel domain walls.

Introduction

Thin film structures [1,2] are increasingly employed each year in a wide range of applications, serving as functional [3,4], reinforcing, light-reflecting, conductive, and dielectric materials. Their utilization extends to contacts, printed circuit boards, and integrated circuit elements in microelectronics, as well as to the fabrication of optical filters, the component base of optoelectronics, and advanced lithographic processes. Due to active experimental and theoretical research on thin films, significant progress has been made in recent years. Since the information in the field of thin film technologies is updated quite rapidly, there is a need for a thorough study and optimization of the main technological processes that are currently used, as well as fundamental features of the thin film formation processes with new composition and coatings of various types. These types of nanomaterials are very promising (in terms of computational performance and energy dissipation efficiency) for use in superconducting digital technologies [5-7] based on Josephson junctions.

It is well established that the properties of nanostructures can significantly differ from those of bulk samples. Currently, close attention is paid to thin-film magnetic structures, which include cobalt and iron [8-10]. Thus, in [1], the crystal structure and composition of Co–Ni–Fe films were evaluated, and it was found out how the deposition rate affects the conversion of a weak magnetic field into magnetic induction. In addition, thin-film structures based on Fe and Co are among the most promising materials that can be applied in the creation of magnetic heads for recording and reading information, memory cells, and other devices [11] which utilize magnetic properties of materials. Magnetic properties of nanofilms [12,13], in particular cobalt nanofilms, represent an important subject of research in both theoretical and practical fields of materials science. These properties depend not only on the composition, but also on factors such as film thickness, which in turn affects their application in microelectronics, spintronics, and other high-tech fields.

The aim of this article is to model the magnetic properties of cobalt nanofilms of different thicknesses and to reveal the main interdependence mechanisms of dimensional, structural, and magnetic subsystems. The proposed modeling methodology and the conducted studies make it possible to analyze the regularities determining the magnetic properties of thin films, which will further make it possible to optimize them for specific applications and tasks. The present work is a development of earlier publications by the authors [14-16].

The cobalt thin films studied in this work can be a component of superconductor–ferromagnetic hybrid nanostructures, which are the basis for the formation of Josephson contacts [13]. These nanomaterials are widely used [17-19] in the creation of individual qubits and quantum computers in general, superconducting microcircuits and interferometers, single photon detectors [20] and other devices of quantum electronics and spintronics.

Mathematical Model for Studying the Magnetic Behavior of Atoms

To conduct computational experiments, we used a mathematical model describing the coordinated motion of atoms and the change of their spin vectors. The spin vector of an atom in this case was understood as the intrinsic magnetic moment associated with the momentum of the atom, which was calculated as a vector sum of the spins of individual electrons included in its structure and their orbital moments.

The mathematical model of atomic displacement and changes in their magnetic moments is based on the Langevin [21] and Landau–Lifshitz–Hilbert [22,23] equations:

$$m_i \frac{\mathrm{d}\mathbf{v}_i}{\mathrm{d}t} = -\frac{\partial U^{\mathrm{MEAM}}(\mathbf{r})}{\partial \mathbf{r}_i} - \frac{\partial H^{\mathrm{ex}}(\mathbf{r})}{\partial \mathbf{r}_i} - \kappa \mathbf{v}_i + \boldsymbol{\chi}(t), \quad (1)$$

$$\frac{\mathrm{d}\mathbf{s}_i}{\mathrm{d}t} = \frac{1}{\left(1+\lambda^2\right)}\left(\left(\boldsymbol{\omega}_i + \boldsymbol{\eta}(t)\right)\times \mathbf{s}_i + \lambda \mathbf{s}_i \times \left(\boldsymbol{\omega}_i \times \mathbf{s}_i\right)\right), \quad i = 1,2,\ldots,N \quad (2)$$

where $U^{\mathrm{MEAM}}(\mathbf{r})$ is the force potential, the modified embedded atom method (MEAM) potential was used in this work; $H^{\mathrm{ex}}(\mathbf{r})$ is the exchange interaction energy of spins; $\mathbf{r} = \{\mathbf{r}_1, \mathbf{r}_2, \ldots, \mathbf{r}_N\}$ is the generalized variable showing the dependence on the whole set of radial vectors of atoms; κ,λ are viscous friction force parameter and damping spin coefficient, respectively; $\boldsymbol{\chi}(t)$, $\boldsymbol{\eta}(t)$ are white noise present in the description of atom motion processes and the behavior of their spins, respectively; and $\boldsymbol{\omega}_i$ is the multiplication value of the gyromagnetic ratio and the local magnetic field [22].

It has been known for quite a long time [24,25] that the fluctuations of thermal and magnetic energy of an atomistic system can be described in the framework of the Langevin theory. To solve stochastic differential equations, which are the basis of this theory, random forces $\boldsymbol{\chi}(t)$ and $\boldsymbol{\eta}(t)$, characterized by the following properties, are used:

$$\left\langle \boldsymbol{\chi}(t) \right\rangle = 0, \left\langle \chi_\alpha(t) \chi_\beta(t') \right\rangle = \frac{2k_\mathrm{B}T_l}{B} \delta_{\alpha\beta} \delta(t-t'), \quad (3)$$

$$\left\langle \boldsymbol{\eta}(t) \right\rangle = 0, \left\langle \eta_\alpha(t) \eta_\beta(t') \right\rangle = \frac{2\pi\lambda k_\mathrm{B}T_s}{\hbar} \delta_{\alpha\beta} \delta(t-t'), \quad (4)$$

where t and t' are different time points; α and β are components of the random force vector, for the three-dimensional case $\{\alpha,\beta\} = \{x,y,z\}$; $\delta(t - t')$ is the Dirac delta measure; k_B is the Boltzmann constant; $\hbar$ is the reduced Planck constant; B is the mobility value of the Brownian particle; and T_l and T_s are values of the thermodynamic and spin temperatures, respectively [26,27].

The potential of the modified embedded atom method [28,29] was based on the electron density functional theory. The magnitude of the potential U^{MEAM} depends on the set of atomic positions, which makes the potential multi-body model:

$$U^{\text{MEAM}}(\mathbf{r}) = \sum_{i}\left(F_i\left(\bar{\rho}_i\right) + \frac{1}{2}\sum_{j,j\neq i}\phi_{ij}\left(r_{ij}\right)\right), \ i = 1,2,\ldots,N, \quad (5)$$

where F_i is the immersion function of each atom in the electron gas created by electrons of all other atoms of the system; $\phi_{ij}(r_{ij})$ is the pair potential function; $r_{ij} = |\mathbf{r}_{ij}| = |\mathbf{r}_j - \mathbf{r}_j|$ is the distance between two atoms with numbers $_i$ and $_j$; and $\bar{\rho}_i$ is the background electron density. When describing the electron density, different types of electron clouds of the atoms under consideration are taken into account, and a sufficiently large set of potential parameters is involved, which makes MEAM sufficiently accurate and allows it to be used in solving a wide range of atomistic modeling problems.

The exchange interaction energy of spins is used in mathematical models to describe the magnetic behavior of systems and allows us to reproduce their ferromagnetic and antiferromagnetic ordering. The total energy value is calculated according to the following expression:

$$H^{\text{ex}}(\mathbf{r}) = -\sum_{j,i\neq j}^{N} J\left(r_{ij}\right)\mathbf{s}_i \cdot \mathbf{s}_j, \quad (6)$$

where $J(r_{ij})$ is the exchange integral, the sign of which determines the type of interaction (ferromagnetic or antiferromagnetic); and $\mathbf{s}_i$ and $\mathbf{s}_j$ are spin vectors of individual atoms. Equation 6 provides a connection between the spatial and spin degrees of freedom of the system through the exchange integral in the form of the Bethe–Slater curve:

$$J\left(r_{ij}\right) = 4\varepsilon\left(\frac{r_{ij}}{\delta}\right)^2\left(1-\gamma\left(\frac{r_{ij}}{\delta}\right)^2\right)e^{-\left(\frac{r_{ij}}{\delta}\right)^2}\Theta\left(R_c - r_{ij}\right), \quad (7)$$

where ε,δ,γ are parametric coefficients of the model; $\Theta(R_c - r_{ij})$ is the piecewise constant of the Heaviside function; and R_c is the distance at which the exchange integral is clipped.

The processes of atomic motion and changes in their magnetic moments were modeled in the LAMMPS software package [30]. This software package was created by a team of authors from Sandia National Laboratories and is distributed under the GPL license (i.e., it is freely available in the form of source codes). The additional package LAMMPS SPIN allows to perform numerical studies of magnetic systems and calculate the spin dynamics of atoms [22,31].

Results and Discussion

The present paper deals with the solution of two problems related to the modeling of magnetic properties of cobalt nanostructures. The first problem was focused on confirming the adequacy of the used mathematical model and checking the convergence of the obtained numerical solutions. The second task investigated the self-organization of atomic spins in cobalt thin films and analyzed the dependence of nanofilm magnetic properties on their thickness. In both problems, there was no external magnetic field in the system, and the material structure corresponded to a face-centered cubic crystal lattice (fcc).

The size of the system in the first problem was small at 500 atoms (5 × 5 × 5 elementary crystal cells) and was due to the study of a similar system in [22]. The appearance of the modeled cobalt crystallite and the magnetic moments of its atoms are shown in Figure 1. Periodic boundary conditions were applied to the computational cell along all coordinate directions. The system was symmetric along all coordinate axes. The magnetic parameters of the exchange integral (Equation 7) were also chosen according to [22]. The magnetic behavior of the cobalt crystallite was considered in two stages. At the first stage (50 ps), relaxation of the system was performed, which resulted in mutual ordering of the spins of the atoms and orientation of the magnetization vector of the whole crystallite in

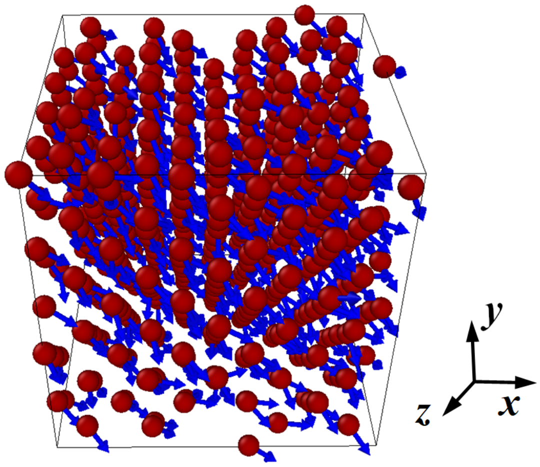

Figure 1: Appearance of a cobalt fcc crystallite (500 atoms) together with the orientation of atomic spins at the final relaxation stage for thermodynamic and spin temperatures of 300 K.

some specific direction. At the second stage (10 ps), fluctuations of the magnetic values of the system stabilized after the relaxation stage were analyzed.

For the stage of fluctuations of magnetic quantities, the graphs of changes in magnetic energy and reduced magnetization modulus (takes values from 0 to 1) of a cobalt crystallite for integration steps dt = 0.1–10.0 fs were plotted. These graphs are selectively illustrated in Figure 2. For the other integration steps, the dependences have similar behavior. The dotted line in Figure 2 shows the average values of energy and magnetization modulus for an integration step of 0.1 fs. For simplicity in comparing the results with previously known data of other authors, the magnetic energy and magnetization modulus analyzed in this work were normalized with respect to the total number of atoms in the system.

Analysis of the plots in Figure 2 shows that small integration steps are characterized by smaller fluctuations of magnetic energy and magnetization modulus. The steps dt = 0.1 fs and dt = 1.0 fs lead to changes in the instantaneous values of the magnetic parameters near the average values of $E = -4.5936$ eV and $|\mathbf{M}| = 0.8747$, respectively. Comparison of the average normalized magnetic energy and normalized magnetization modulus of a similar cobalt crystallite system from [22] gives values of $E = -4.4900$ eV and $|\mathbf{M}| = 0.9019$, which correspond to a relative error value of 2% for energy and 3% for the magnetization modulus. The level of deviation of the parameters may be related to the fact that in [22] the modeling was carried out within the framework of the microcanonical ensemble, while in the present work a stochastic approach based on the Landau–Lifshitz–Hilbert equation was used.

For further analysis of the convergence of the numerical solutions and the influence of the time step on the fluctuations of the magnetic properties of the system, the relative deviations of the normalized magnetic energy $\Delta E(\Delta t)$ and magnetization modulus $\Delta M(\Delta t)$ were calculated. At the same time, additional averaging over the already performed time steps was performed for the considered quantities:

$$\Delta E(\Delta t) = \frac{1}{N_{\text{step}}} \sum_{k=1}^{N_{\text{step}}} \left| \frac{E_k(\Delta t) - \langle E \rangle (\Delta t)}{\langle E \rangle (\Delta t)} \right|, \tag{8}$$

$$\Delta M(\Delta t) = \frac{1}{N_{\text{step}}} \sum_{k=1}^{N_{\text{step}}} \left| \frac{M_k(\Delta t) - \langle M \rangle (\Delta t)}{\langle M \rangle (\Delta t)} \right|, \; M = |\mathbf{M}|, \tag{9}$$

where N_{step} is the previously performed number of time steps; $E_k(\Delta t)$ and $M_k(\Delta t)$ are magnetic energy and magnetization modulus at the current time step; $\langle E \rangle(\Delta t)$ and $\langle M \rangle(\Delta t)$ are average values of the considered parameters over the entire time period.

The deviations of the magnetic parameters from Equation 8 and Equation 9 as a function of different integration steps are shown in Figure 3. For convenience in analyzing the data in Figure 3, the values along the abscissa and ordinate axes are given in logarithmic scale. The black dashed lines represent linear approximation functions, since the calculated points of the graphs are nearly a straight line. The approximation value for the deviation of magnetic energy $\Delta E(\Delta t)$ was $R^2 = 0.96$, for the deviation of magnetization modulus $\Delta M(\Delta t)$ was $R^2 = 0.93$.

A comparison of $\Delta E(\Delta t)$ and $\Delta M(\Delta t)$, obtained from the simulations in this work and the values from [22] indicates a satisfactory qualitative and quantitative agreement of the values. This analysis confirms that the modeling of magnetic properties and behavior of nanomaterials at the atomistic level should be

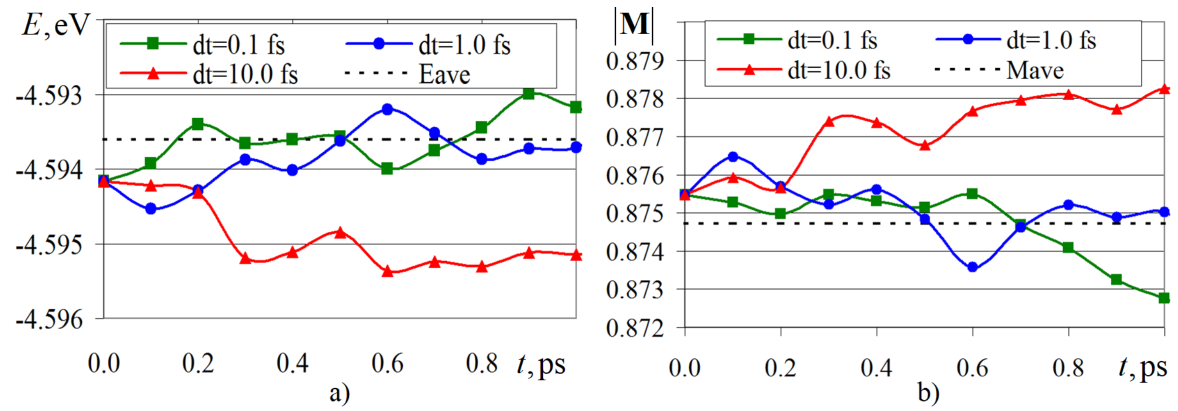

Figure 2: Variation of magnetic energy (a) and magnetization modulus (b) of a cobalt fcc crystallite (500 atoms) for different steps of integrating the systems of Equation 1 and Equation 2.

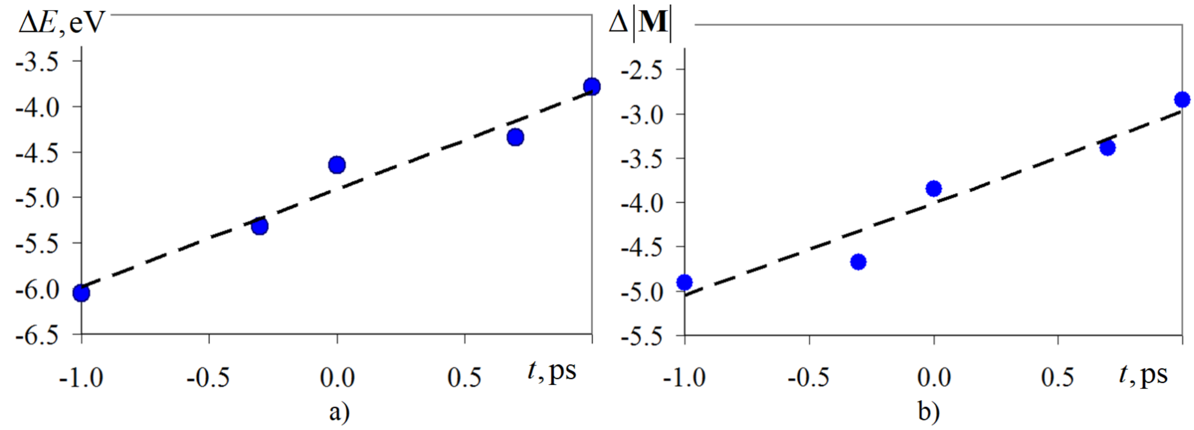

Figure 3: Dependences of the deviation of the relative normalized magnetic energy (a) and magnetization modulus (b) from different time steps of integration. The scales on the abscissa and ordinate axes are presented in decimal logarithm values.

carried out at integration time steps of no more than 1.0 fs. Typical spin dynamics models use a time step 0.1 fs, but the algorithm remains sufficiently accurate up to a time step of 10.0 fs. Therefore, for conducting computational experiments, an integration step of up to 10.0 fs can be used. According to [22], numerical results obtained with a time step of 0.1 fs show the greatest stability and robustness, since the characteristic time scales of changes in the magnetic moments of atoms are much smaller compared to their spatial counterparts. In the second problem, a unified integration step of 0.1 fs was used for all computational experiments.

In the second problem, crystalline cobalt (fcc) nanofilms containing 20 elementary crystal cells along the x and y axes were considered. The thickness of the films in the z-axis direction was varied in the range from 5 to 20 in steps of one elementary crystal cell. As studies show, the magnetic ordering in cobalt nanofilms with a thickness of less than 1.8 nm becomes unstable, and in the monolayer limit, it can be completely destroyed. When the film thickness is less than 1–2 monolayers (≈0.2–0.4 nm), the nanofilm ceases to be continuous, forming islands. This leads to random fluctuations in magnetization. Additionally, in monolayers and sub-monolayers, the number of nearest neighbors for cobalt atoms sharply decreases. This weakens the exchange interaction that stabilizes the ferromagnetic order. Disruption of lattice periodicity and a high density of defects exacerbate this problem. For these reasons, such studies are not included in this article. Thus, 16 computational experiments were realized in the second task, in which the thickness of the nanofilms was gradually increased and the investigated systems contained from 8,800 to 32,800 cobalt atoms. Along the horizontal axes (x and y), periodic boundary conditions were applied along the edges of the nanofilm, while vertically (z coordinate axis) the boundaries of the computational cell remained free.

The numerical realization of each individual computational experiment included two stages. At the first stage, the system proceeded through the stage of partial ordering of magnetic moments from the initial random distribution of spins and subsequent relaxation within 50 ps. This stage was necessary to exclude the influence of initial conditions on the magnetic characteristics further investigated. In the second stage, the magnetic properties of the previously energetically equilibrated cobalt nanofilm were investigated. The duration of the second stage was 10 ps. In both stages, there were no external influences on the system. The thermodynamic and spin temperatures were maintained at 300 K, with temperature damping parameters of $\tau_t = \tau_s = 0.01$ ps.

Magnetic energy and reduced magnetization modulus were considered as the investigated properties of cobalt nanofilms. As in the first problem, these quantities were normalized compared to the total number of atoms of the system for convenience of comparison. Figure 4 and Figure 5 are plots of the time variation of magnetic energy and magnetization modulus for the whole series of computational experiments. For clarity, the shade of the lines in the graphs is depicted in a darker color with increasing film thickness L_z, where L_z = 1.8 nm corresponds to five elementary crystal cells, and L_z = 7.1 nm to 20 elementary crystal cells.

As can be seen from the graphs in Figure 4 and Figure 5, the magnetic energy of the systems at this stage of the computational experiment stabilizes and does not significantly change over time; only its insignificant fluctuations are noticeable. In-

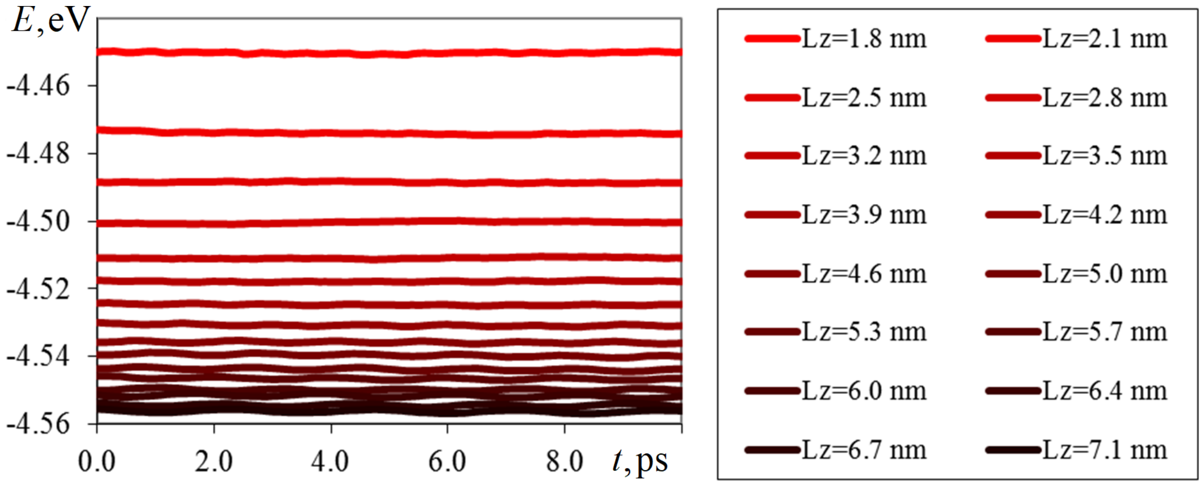

Figure 4: Variation of the magnetic energy of cobalt (fcc) normalized by the number of atoms in the system for nanofilms with thicknesses of 1.8–7.1 nm and thermodynamic and spin temperatures of 300 K.

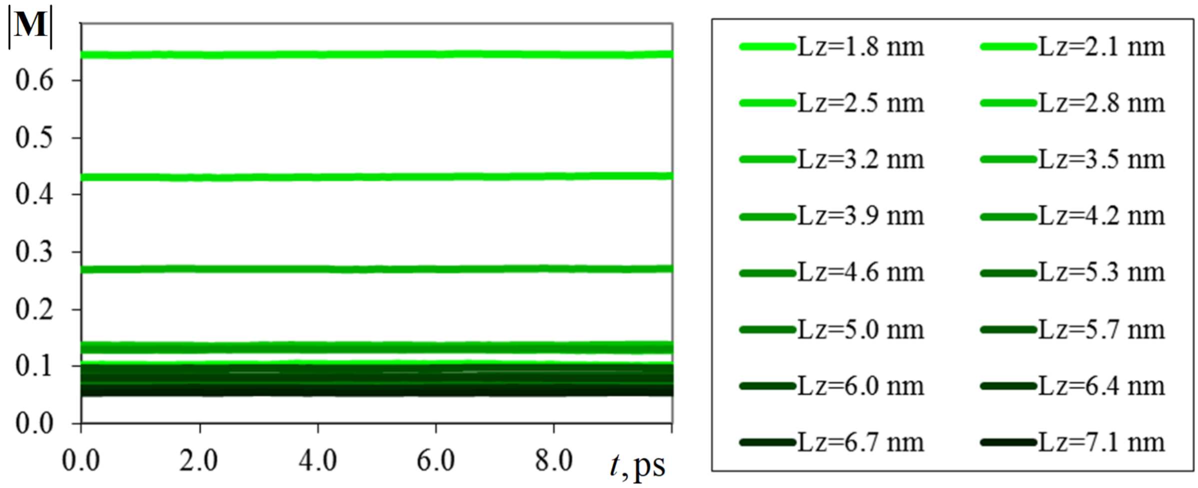

Figure 5: Variation of the magnetization modulus of cobalt (fcc) normalized by the number of atoms in the system, for nanofilms of thicknesses 1.8–7.1 nm and thermodynamic and spin temperatures of 300 K.

creasing the thickness of the nanofilm, in turn, leads to a decrease in the value of magnetic energy, in connection with which a gradient change of colors in the graphs in Figure 4 is observed. The most significant differences in the magnetic energy values were obtained for thin films L_z = 1.8–3.2 nm. For thicker cobalt nanofilms, the values of normalized magnetic energy are in the range of −4.56 to −4.53 eV. Such behavior of the magnetic energy can be related to the fact that with increasing thickness of the nanofilm, the fraction of its surface atoms decreases and the influence of various surface effects decreases. As the number of crystalline layers of the nanofilm increases, the modeled system approaches a bulk material in terms of its physical properties. That is why, from the point of view of functional characteristics, thin-film ferromagnetic nanostructures are of the greatest interest.

Analysis of the graphs in Figure 5 shows that for the whole series of computational experiments after the relaxation stage, the magnetization modulus value also slightly changes in time. The simulation results indicate that as the thickness of the nanofilm increases, there is a tendency to decrease the value of its magnetization modulus. Most of the values are concentrated in the range from 0.05 to 0.13. However, there are a number of exceptions to the smooth gradient variation of the magnetization modulus in Figure 5, indicating its nonlinear dependence on the thickness of the investigated nanofilm. Since on the basis of Figure 5 it is difficult to speak about the type of the obtained dependence, we have plotted graphs of changes in the individual components of the magnetization vector (in absolute values), which are presented in Figure 6. In a separate inset in Figure 6, the behavior of the magnetization modulus for cobalt nanofilms of different thicknesses is shown. As M_α in Figure 6, the time-averaged value of the components of the magnetization vector was used.

The study of the dependences plotted in Figure 6 indicates that the film thickness has a significant effect on the magnetization value. A three-modal distribution of the magnetization vector components with peaks is observed at nanofilm thicknesses of 6, 10, and 12 crystal cells. The intensity of the peaks decreases with increasing thickness of the cobalt layers, which is clearly visible in Figure 6. The value of each next mode decreased in absolute value by more than 50% compared to the previous one. It is also interesting to notice that all three modal values were obtained for nanofilms with an even value of crystalline layers. The influence of the nanofilm thickness on the magnetization value significantly decreases for film thicknesses above 4.5 nm. In this range of values, local oscillations of the magnetization vector components occur, but they do not significantly affect the final modulus value.

The presence of the obtained peaks of the magnetization vector components distribution in Figure 6 may be due to surface effects in thin films and the formation of domain walls. Depending on the symmetry of the modeled crystalline structures, the joint orientation of magnetic moments of atoms and their way of turning on the boundary, the types of domain walls may differ. For example, Bloch-type domain walls, Neel-type domain walls, walls with reduced angle, and cylindrical domain walls are known. Analysis of magnetic moments of atoms mutually ordered as a result of modeling has shown that, for some cases of calculations for thin films of cobalt, the formation of Neel domain walls is typical [32-34]. An illustration of the resulting Neel domain wall is given in Figure 7, which shows the orientation of atomic spins obtained by numerical simulation after the relaxation and equilibration of the system.

As can be seen in Figure 7, the reversal of the magnetic moments of individual atoms occurs in the plane of the nanofilm. After the reversal, the spins of the atoms are oriented in the opposite direction, which is demonstrated in the right part of Figure 7. For nanofilms with a thickness of 13–20 crystalline layers, the formation of Neel walls dividing the modeled sample into domains with opposite directions of magnetic moments is observed. As a result, the total magnetization of the nanofilm is formed in the range of 0.07–0.01. It is known that the Neel domain walls occur in thin films with a thickness of 100 nm or less, which agrees well with the simulation results obtained. Since it is typical for ferromagnetic materials to form domains and domain walls due to the strong interaction of spin moments of nearby atoms, the data of computational experiments confirm the ferromagnetic nature of the magnetic behavior of cobalt nanofilms.

For nanofilms with thicknesses of 6, 10, and 12 crystalline cells, which corresponded to the peaks and maximum values of the

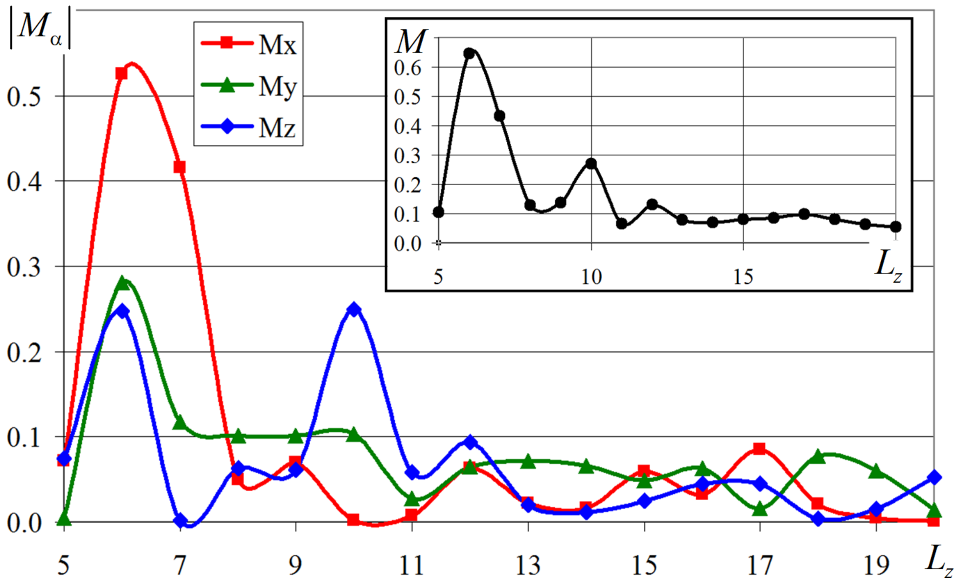

Figure 6: Variation of magnetization vector components (in absolute values) M_α,α = {*x*,*y*,*z*} as a function of cobalt nanofilm thickness measured in crystalline layers L_z, M = |**M**|.

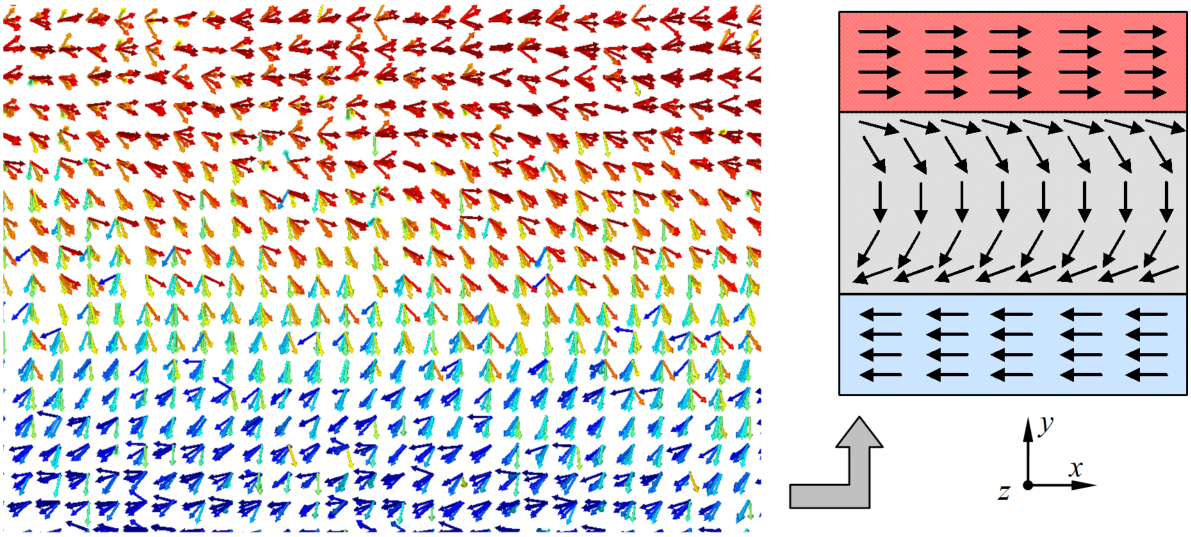

Figure 7: Formation of Neel domain walls in a cobalt nanofilm after the relaxation stage.

magnetization vector, the formation of domains of approximately the same size with antiparallel spin distribution was not observed. The predominant orientation of magnetic moments of cobalt atoms in a certain direction led to bursts and jumps in the values of individual components (x, y, z) of the magnetization vector and its modulus as a whole, which is clearly visible in the graphs in Figure 6. Due to the fact that it is difficult to assess the peculiarities of the connection between the magnetic energy of the modeled nanofilms and their thickness in Figure 4, the graph for these values was separately plotted.

Figure 8 shows a nonlinear dependence of the magnetic energy on the thickness of the modeled nanofilm. The given values of magnetic energy were pre-averaged over time for a period of 10 ps after the relaxation step. The smooth change of the graph in Figure 8 may be due to a gradual and uniform decrease in the fraction of surface atoms of the nanofilms as their thicknesses increase.

The graph of calculated magnetic energy values is well approximated by a polynomial dependence of the fifth degree (the

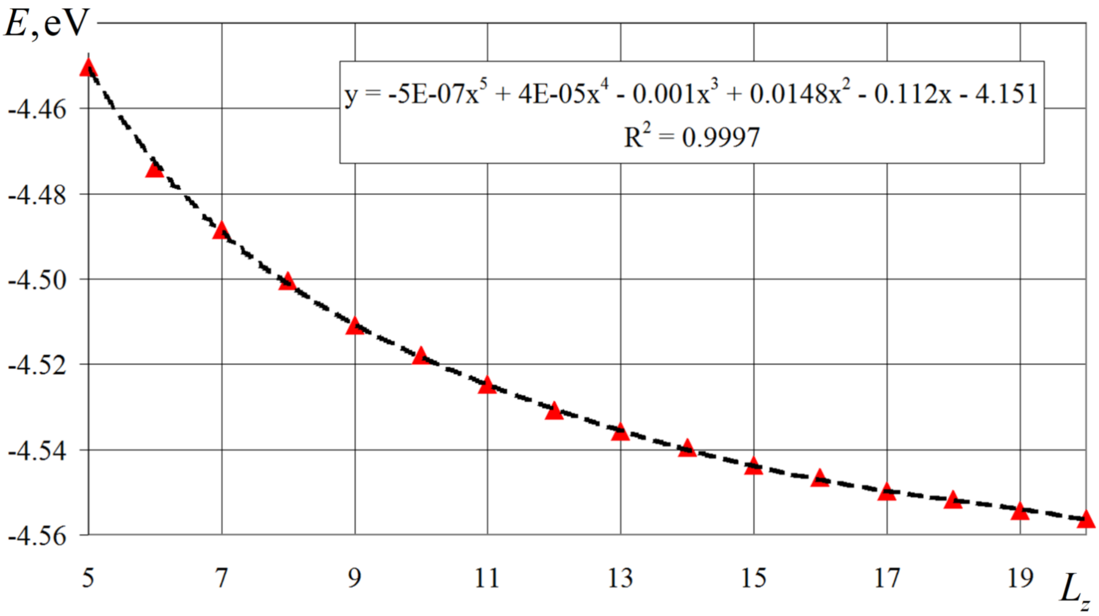

Figure 8: Variation of cobalt magnetic energy as a function of nanofilm thickness measured in crystalline layers.

equation is shown in the frame in Figure 8). The value of reliability of the constructed trend line is 0.9997. Simplification of the approximating function to a polynomial of the third degree (the coefficients in front of the 4th and 5th order terms are quite small) also brings about good results of the trend line at the reliability level of 0.9978. Linear approximation gives a lower indicator of the reliability level (i.e., 0.8848).

Conclusion

The mathematical model considered in this work allows us to investigate the magnetic behavior of a nanoscale system taking into account spin and interatomic interactions. The mathematical model is based on the joint solution of the Langevin and Landau–Lifshitz–Hilbert equations. In this work, the multi-particle potential of the modified immersed atom method, which is well established for solving such problems, is used to describe the interatomic interaction.

Numerical studies of the magnetic behavior of cobalt-based nanofilms were carried out in two stages. Analysis of the convergence of numerical solutions and evaluation of the time step effect on the fluctuations of the magnetic properties of the system showed that modeling of magnetic properties and behavior of nanomaterials at the atomistic level should be carried out at integration time steps of no more than 1.0 fs. A time step of 0.1 fs was used for the main series of computational experiments.

The study of the influence of the cobalt nanofilm thickness on the magnetic behavior of the system showed a decrease in the magnetic energy with increasing film thickness. It should be noted that the magnetic energy nonlinearly changes with increasing thickness of the cobalt nanofilm. The magnetization rate of the modeled systems also does not significantly change with time. The analyzed dependence of the magnetization norm on the thickness of the studied nanofilms illustrate the nonlinear change of this magnetic characteristic with peaks at nanofilm thicknesses of 6, 10, and 12 crystal cells. The effect of the nanofilm thickness on the magnetization value is leveled off at nm. The effects observed in the investigated films can be due to surface effects in thin films and the formation of Neel domain walls.

The dependence of the magnetic energy on the thickness of the modeled nanofilm has a nonlinear form and is well approximated by a polynomial of degree 5. Due to insignificant coefficients in front of the 4th and 5th order terms, the approximation function can be simplified to a 3rd order polynomial without significant decrease in the accuracy level. The gradual nonjump-like change of magnetic energy with increasing thickness of the studied cobalt nanofilms can be associated with a uniform and proportional decrease in the fraction of surface atoms in the thickened films.

Funding

The work was carried out within the framework of the state assignment No. FUUE-2025-0001 “Modeling and experimental studies of the structure and magnetic parameters of a Josephson contact from a multilayer nanostructure” (methodology for modeling magnetic properties) and with the financial support of the Russian Science Foundation (project No. 23-72-30004) (research at ultra-low temperatures) and the project No. 020201 of the Moldova State Program “Nanostructures and advanced materials for implementation in spintronics, thermoelectricity, and optoelectronics” (samples preparation and investigation of Nb/Co interfaces).

Author Contributions

Aleksey Fedotov: conceptualization; project administration; writing – review & editing. Olesya Severyukhina: formal analysis; investigation; writing – original draft. Anastasia Salomatina: software; validation; visualization. Anatolie Sidorenko: conceptualization; funding acquisition; writing – review & editing.

ORCID® iDs

Aleksey Fedotov - https://orcid.org/0000-0002-0463-3089
Olesya Severyukhina - https://orcid.org/0000-0001-6014-9462
Anatolie Sidorenko - https://orcid.org/0000-0001-7433-4140

Data Availability Statement

Data generated and analyzed during this study is available from the corresponding author upon reasonable request.

Preprint

A non-peer-reviewed version of this article has been previously published as a preprint: https://doi.org/10.3762/bxiv.2025.6.v1

References

1. Tikhonov, R. D.; Cheremisinov, A. A.; Tikhonov, M. R. *Perspect. Mater.* **2024,** *1,* 20–29. doi:10.30791/1028-978x-2024-1-20-29
2. Beagle, L. K.; Fang, Q.; Tran, L. D.; Baldwin, L. A.; Muratore, C.; Lou, J.; Glavin, N. R. *Mater. Today* **2021,** *51,* 427–448. doi:10.1016/j.mattod.2021.08.007
3. Shalygina, E.; Svalov, A.; Kharlamova, A.; Ganshina, E.; Doronin, D.; Kurlyandskaya, G. *Jpn. J. Appl. Phys.* **2016,** *55,* 07MF01. doi:10.7567/jjap.55.07mf01
4. Patrin, G. S.; Yakovchuk, V. Y.; Yarikov, S. A.; Shiyan, Y. G.; Furdyk, V. P. *Tech. Phys. Lett.* **2019,** *45,* 507–510. doi:10.1134/s1063785019050262
5. Likharev, K. K. *Phys. C (Amsterdam, Neth.)* **2012,** *482,* 6–18. doi:10.1016/j.physc.2012.05.016
6. Krylov, G.; Kawa, J.; Friedman, E. G. *IEEE Nanotechnol. Mag.* **2021,** *15,* 54–67. doi:10.1109/mnano.2021.3113218

7. Soloviev, I. I.; Bakurskiy, S. V.; Ruzhickiy, V. I.; Klenov, N. V.; Kupriyanov, M. Y.; Golubov, A. A.; Skryabina, O. V.; Stolyarov, V. S. *Phys. Rev. Appl.* **2021,** *16,* 044060. doi:10.1103/physrevapplied.16.044060
8. Shalygina, E.; Kharlamova, A.; Makarov, A.; Kurlyandskaya, G.; Svalov, A. *EPJ Web Conf.* **2018,** *185,* 03009. doi:10.1051/epjconf/201818503009
9. Kamashev, A. A.; Garif'yanov, N. N.; Validov, A. A.; Kataev, V.; Osin, A. S.; Fominov, Y. V.; Garifullin, I. A. *Beilstein J. Nanotechnol.* **2024,** *15,* 457–464. doi:10.3762/bjnano.15.41
10. Pashin, D. S.; Pikunov, P. V.; Bastrakova, M. V.; Schegolev, A. E.; Klenov, N. V.; Soloviev, I. I. *Beilstein J. Nanotechnol.* **2023,** *14,* 1116–1126. doi:10.3762/bjnano.14.92
11. Sidorenko, A. S.; Hahn, H.; Krasnov, V. *Beilstein J. Nanotechnol.* **2023,** *14,* 79–82. doi:10.3762/bjnano.14.9
12. Kamzin, A. S.; Wei, F.; Ganeev, V. R.; Valiullin, A. A.; Zaripova, L. D.; Tagirov, L. R. *Phys. Solid State* **2014,** *56,* 948–954. doi:10.1134/s1063783414050114
13. Voronova, N.; Grudinina, A.; Panico, R.; Trypogeorgos, D.; De Giorgi, M.; Baldwin, K.; Pfeiffer, L.; Sanvitto, D.; Ballarini, D. *Nat. Commun.* **2025,** *16,* 466. doi:10.1038/s41467-024-55119-8
14. Vakhrushev, A.; Fedotov, A.; Boian, V.; Morari, R.; Sidorenko, A. *Beilstein J. Nanotechnol.* **2020,** *11,* 1776–1788. doi:10.3762/bjnano.11.160
15. Vakhrushev, A.; Fedotov, A.; Severyukhina, O.; Sidorenko, A. *Beilstein J. Nanotechnol.* **2023,** *14,* 23–33. doi:10.3762/bjnano.14.3
16. Vakhrushev, A.; Fedotov, A.; Sidorenko, A. *Key Eng. Mater.* **2021,** *888,* 57–65. doi:10.4028/www.scientific.net/kem.888.57
17. Huang, Z.; Lotfizadeh, N.; Elfeky, B. H.; Kisslinger, K.; Cuniberto, E.; Yu, P.; Hatefipour, M.; Taniguchi, T.; Watanabe, K.; Shabani, J.; Shahrjerdi, D. *Appl. Phys. Lett.* **2022,** *121,* 243503. doi:10.1063/5.0135034
18. Pellegrino, F. M. D.; Falci, G.; Paladino, E. *Commun. Phys.* **2022,** *5,* 265. doi:10.1038/s42005-022-01042-7
19. Pal, B.; Chakraborty, A.; Sivakumar, P. K.; Davydova, M.; Gopi, A. K.; Pandeya, A. K.; Krieger, J. A.; Zhang, Y.; Date, M.; Ju, S.; Yuan, N.; Schröter, N. B. M.; Fu, L.; Parkin, S. S. P. *Nat. Phys.* **2022,** *18,* 1228–1233. doi:10.1038/s41567-022-01699-5
20. Walsh, E. D.; Jung, W.; Lee, G.-H.; Efetov, D. K.; Wu, B.-I.; Huang, K.-F.; Ohki, T. A.; Taniguchi, T.; Watanabe, K.; Kim, P.; Englund, D.; Fong, K. C. *Science* **2021,** *372,* 409–412. doi:10.1126/science.abf5539
21. Paquet, E.; Viktor, H. L. *BioMed Res. Int.* **2015,** 183918. doi:10.1155/2015/183918
22. Tranchida, J.; Plimpton, S. J.; Thibaudeau, P.; Thompson, A. P. *J. Comput. Phys.* **2018,** *372,* 406–425. doi:10.1016/j.jcp.2018.06.042
23. Gilbert, T. L. *IEEE Trans. Magn.* **2004,** *40,* 3443–3449. doi:10.1109/tmag.2004.836740
24. Brown, W. F., Jr. *Phys. Rev.* **1963,** *130,* 1677–1686. doi:10.1103/physrev.130.1677
25. García-Palacios, J. L.; Lázaro, F. J. *Phys. Rev. B* **1998,** *58,* 14937–14958. doi:10.1103/physrevb.58.14937
26. Rugh, H. H. *Phys. Rev. Lett.* **1997,** *78,* 772–774. doi:10.1103/physrevlett.78.772
27. Nurdin, W. B.; Schotte, K.-D. *Phys. Rev. E* **2000,** *61,* 3579–3582. doi:10.1103/physreve.61.3579
28. Lee, B.-J.; Baskes, M. I.; Kim, H.; Koo Cho, Y. *Phys. Rev. B* **2001,** *64,* 184102. doi:10.1103/physrevb.64.184102
29. Baskes, M. I. *Phys. Rev. B* **1992,** *46,* 2727–2742. doi:10.1103/physrevb.46.2727
30. Plimpton, S. *J. Comput. Phys.* **1995,** *117,* 1–19. doi:10.1006/jcph.1995.1039
31. Beaujouan, D.; Thibaudeau, P.; Barreteau, C. *Phys. Rev. B* **2012,** *86,* 174409. doi:10.1103/physrevb.86.174409
32. Trunk, T.; Redjdal, M.; Kákay, A.; Ruane, M. F.; Humphrey, F. B. *J. Appl. Phys.* **2001,** *89,* 7606–7608. doi:10.1063/1.1355357
33. DeJong, M. D.; Livesey, K. L. *Phys. Rev. B* **2015,** *92,* 214420. doi:10.1103/physrevb.92.214420
34. Catalan, G.; Seidel, J.; Ramesh, R.; Scott, J. F. *Rev. Mod. Phys.* **2012,** *84,* 119–156. doi:10.1103/revmodphys.84.119

License and Terms

BEILSTEIN JOURNAL OF NANOTECHNOLOGY

Few-photon microwave fields for superconducting transmon-based qudit control

Irina A. Solovykh[1,2], Andrey V. Pashchenko[1,3,4], Natalya A. Maleeva[5],
Nikolay V. Klenov*[1,3], Olga V. Tikhonova[1,2,6] and Igor I. Soloviev[1,6]

Full Research Paper

Open Access

Address:
[1]Lomonosov Moscow State University, Faculty of Physics, Moscow, 119991, Russia, [2]Lomonosov Moscow State University, Skobeltsyn Institute of Nuclear Physics, Moscow, 119991, Russia, [3]All-Russian Research Institute of Automatics n.a. N.L. Dukhov (VNIIA), 127055, Moscow, Russia, [4]Moscow Technical University of Communications and Informatics (MTUCI), 111024, Moscow, Russia, [5]National University of Science and Technology "MISIS", 119049, Moscow, Russia and [6]Kotel'nikov Institute of Radio Engineering and Electronics of RAS, 125009 Moscow, Russia

Email:
Nikolay V. Klenov* - nvklenov@mail.ru

* Corresponding author

Keywords:
Josephson "atoms"; non-classical fields; quantum state control; superconducting qubits

Beilstein J. Nanotechnol. **2025,** *16,* 1580–1591.
https://doi.org/10.3762/bjnano.16.112

Received: 01 May 2025
Accepted: 19 August 2025
Published: 11 September 2025

This article is part of the thematic issue "Superconducting artificial neural networks and quantum circuits".

Guest Editor: A. S. Sidorenko

Abstract

Increasing the efficiency of quantum processors is possible by moving from two-level qubits to elements with a larger computational base. An example would be a transmon-based superconducting atom, but the new basic elements require new approaches to control. To solve the control problem, we propose the use of nonclassical fields in which the number of photons is comparable to the number of levels in the computational basis. Using theoretical analysis, we have shown that (i) our approach makes it possible to efficiently populate on demand even relatively high energy levels of the qudit starting from the ground state; (ii) by changing the difference between the characteristic frequencies of the superconducting atom and a single field mode, we can choose which level to populate; and (iii) even the highest levels can be effectively populated on a sub-nanosecond time scale. We also propose the quantum circuit design of a real superconducting system in which the predicted rapid control of the transmon-based qudit can be demonstrated.

Introduction

Currently, quantum computing is under active development, opening new horizons for solving a number of problems that are difficult for classical processors, including modeling the behavior of quantum systems, optimization problems, breaking cryptographic systems, solving large systems of linear equations, and analyzing heat conduction equations [1-6].

The basis for the physical implementation of these computations is a quantum processor consisting of computational cells called qudits, whose states can be represented with satisfactory accuracy in the form of a decomposition into n basis states. Today, the main focus is on processors based on qubits (a special case of qudits with $n = 2$) on a superconducting, ionic, or other platform. However, it is still not easy to create the necessary number of qubits and control channels to implement really useful quantum algorithms. A promising solution to this problem is to expand the computational basis of an element by switching to qutrits ($n = 3$), ququarts ($n = 4$), and so on [7-12].

We believe that an additional synergistic effect can be achieved by using quantum electromagnetic fields with a comparable (with n) number of photons to control such quantum multilevel systems. The coexistence of different photons in a single waveguide should make it possible to use the scarce control circuits on a quantum chip more efficiently. In the future, the analysis of the behavior of “qudits + multiphoton quantum field” systems will form the basis for the practical implementation of quantum internet and telecommunication systems [13-16].

Among the many possibilities, we will focus on a superconducting platform; it allows one to create sources and mixers for microwave photons, qubits, and qudits with corresponding characteristic frequencies of transitions between basis states, as well as radiation detectors with the claim of being quantum-sensitive [17-26].

So far, the most common artificial atom among the superconducting ones is considered to be a charge qubit with a large shunt capacity, namely a transmon [27-29]. The transmon is technically simple to fabricate, easy to operate, and resistant to decoherence from various sources. Transmon-based qudits are already being used to detect microwave fields [30]. The latter feature makes it possible to achieve a long lifetime of this artificial atom; in a recent work [29] “coherence” times of T_1 = 64–13 μs, Ramsey periods of T_{2R} = 85–16 μs, and Hahn echo times T_{2E} = 93–22 μs for levels of n = 2–10, respectively, have been achieved.

It should be noticed that the spectrum of eigenvalues of the Hamiltonian of a real transmon (a slightly nonlinear oscillator) is quite close to the equidistant one; however, a number of widely used theoretical models describing its evolution in an external electromagnetic field (the Jaynes–Cummings model) do not take into account the high-lying energy levels of the artificial atom, nor the nonlinearity existing in a real solid-state system [31-33]. In our fully quantum analysis of the “atom”–field interaction, the nonlinearity of transmon will be taken into account.

This article presents the results of a theoretical description of the interaction between a few-photon microwave non-classical field and a transmon-based qudit with several, even high-lying, levels being taken into account. We develop methods of rapid quantum control of the designed transmon-based qudit and its state population dynamics. The structure of the article is as follows: First, the model of the system under study is described in more detail, followed by a theoretical description of the Fock-based control of the qudit states and a discussion of possible practical implementations.

Results

Model description

The system under consideration consists of a high-quality superconducting resonator (the quality factor is about 10^5–10^6 and depends mainly on the external coupling $C_{\text{in/out}}$) connected to a transmon [34] by a capacitance C_g (see Figure 1). The resonator in this system is a quantum harmonic oscillator with a fully equidistant energy spectrum described by the bosonic ladder operators $\hat{a}$ and $\hat{a}^+$, and the photon number operator $\hat{n}_a = \hat{a}^+\hat{a}$. The transmon is considered as an anharmonic oscillator (with ladder operators $\hat{b}$ and $\hat{b}^+$) with the number of excitations in the solid-state system similarly introduced as $\hat{n}_b = \hat{b}^+\hat{b}$. In a transmon, the inductance is created using a nonlinear element, that is, a nanoscale Josephson junction (JJ), or a pair of JJs forming an interferometer-like circuit, so the spectrum is no longer equidistant. In the case where the JJ pair is used, the characteristic (plasma) frequency of the transmon can be quickly adjusted in 10–20 ns in the range of 1 GHz by an external magnetic field [35]. In practice, researchers try to reduce the transmon frequency dependence on the external magnetic field to get rid of parasitic flux fluctuations. A large shunt capacitance C_B is needed to increase resistance to parasitic charge fluctuations [36].

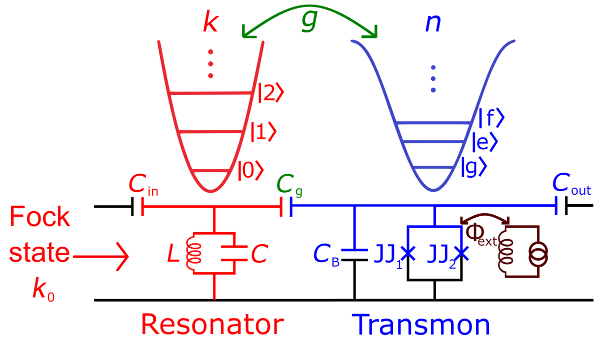

Figure 1: Schematic representation of the model under discussion: A few-photon microwave field from a high-quality resonator (red) affects an artificial transmon-based atom (blue). The potential energies and energy spectra for harmonic (resonator) and anharmonic (transmon) oscillators are shown above. Crosses mark the Josephson junctions in the transmon interferometer. The external magnetic flux Φ_ext is used to tune the spectrum of a transmon.

A few-photon non-classical microwave field (with a certain number of photons, k_0) enters the resonator [37-42] with variable frequency detuning $\Delta\omega$ between the resonator and the artificial atom. The time evolution of the quantum state of the transmon qudit, the populations of its eigenstates, and the number n of excitations induced in the superconducting system by the quantum field is studied. By taking into account the nonlinearities in the system, it will be shown that there is a certain value of the frequency detuning at which the dynamics of the energy transition from the field to the solid-state system and vice versa is most efficient.

Theoretical description of Fock-based qudit control

First, we need to quantize the field in the harmonic oscillator that corresponds to a high-quality resonator. The energy of the electric field stored in the capacitor and the energy of the magnetic field stored in the inductor can be written as follows:

$$H_{LC}=\frac{Q^2}{2C}+\frac{\Phi^2}{2L}\rightarrow\hat{H}_{LC}=\hbar\omega_0\left(\hat{a}^+\hat{a}+\frac{1}{2}\right),\tag{1}$$

with operators of quantum charge and flux introduced by:

$$\hat{Q}=iQ_{\text{zpf}}\left(\hat{a}^+-\hat{a}\right),\quad\hat{\Phi}=\Phi_{\text{zpf}}\left(\hat{a}^++\hat{a}\right),\tag{2}$$

where

$$Q_{\text{zpf}}=\sqrt{\frac{\hbar}{2Z_0}},\ \Phi_{\text{zpf}}=\sqrt{\frac{\hbar Z_0}{2}}$$

are the vacuum fluctuations of charge and flux, Z_0 is the characteristic impedance, and $\omega_0=1/\sqrt{LC}$ is the resonator angular frequency. The transmon is treated almost the same way, but, in this case, the number of Cooper pairs on the shunt capacitor C_B (island) and the phase on the JJ/(interferometer) are quantized as follows:

$$\hat{n}_{\text{CP}}=\frac{i}{2}\left(\frac{E_\text{J}}{2E_\text{C}}\right)^{\frac{1}{4}}\left(\hat{b}^+-\hat{b}\right),\hat{\varphi}=\left(\frac{2E_\text{C}}{E_\text{J}}\right)^{\frac{1}{4}}\left(\hat{b}^++\hat{b}\right),\tag{3}$$

where charge energy $E_\text{C}=\text{e}^2/2C_\text{B}$ and Josephson energy $E_\text{J}=(\Phi_0 I_\text{c})/2\pi$ are used (I_c is the critical current flowing through the Josephson junction). The Hamiltonian for the transmon part of our system can be written in the following form, taking into account the nonlinearity [6]:

$$\hat{H}_0=\hbar\omega_\text{p}\hat{b}^+\hat{b}-\frac{E_\text{C}}{12}\left(\hat{b}+\hat{b}^+\right)^4,\tag{4}$$

where $-E_\text{C}/12$ is the nonlinearity parameter and $\omega_\text{p}=\sqrt{8E_\text{J}E_\text{C}}/\hbar$ is the plasma frequency of the transmon.

The first term in the Hamiltonian describes a free linear evolution of the photon operators, characterized by their oscillations in time in the Heisenberg representation. The nonlinear term in the Hamiltonian can be averaged over high-frequency oscillations, leaving only smoothly varying terms. This procedure actually corresponds to the so-called rotating wave approximation, in which the following type of nonlinear term can be obtained:

$$\left(\hat{b}+\hat{b}^+\right)^4\approx 6\hat{n}_b^2+6\hat{n}_b+3.\tag{5}$$

The expression for the nonlinear term obtained in Equation 5 indicates that the nonlinearity of the transmon is similar to the type of Kerr phase modulation $\gamma\hat{n}_b(\hat{n}_b+1)$, with $\gamma=-E_\text{C}/2\hbar$. Thus, the Hamiltonian in Equation 4 can be rewritten as follows:

$$\hat{H}_0=\hbar\omega_\text{p}\hat{n}_b+\hbar\gamma\hat{n}_b\left(\hat{n}_b+1\right).\tag{6}$$

Note that, for such a system, the operator $\hat{n}_b$ is found to be independent on time (being an integral of motion). This means that this nonlinearity itself leads only to phase modulation without changing the excitation statistics.

In our case, the dynamics of the excitations of a Josephson nanosystem (transmon) under the action of a nonclassical electromagnetic field is studied. The interaction of the photonic and superconducting subsystems is investigated by direct solution of the nonstationary Schrödinger equation:

$$i\hbar\frac{\partial\Psi}{\partial t}=\hat{H}\Psi.\tag{7}$$

The Hamiltonian of such a system, taking into account both the nonlinearity of the transmon and the transmon–field coupling, can be written as follows:

$$\begin{aligned}\hat{H}=\hbar\omega_0\left(\hat{n}_a+\frac{1}{2}\right)+\hbar\left(\omega_0+\Delta\omega\right)\left(\hat{n}_b+\frac{1}{2}\right)\\+\hbar\gamma\hat{n}_b\left(\hat{n}_b+1\right)+\hbar\frac{g}{2}\left(\hat{b}^+\hat{a}+\hat{b}\hat{a}^+\right),\end{aligned}\tag{8}$$

where $\omega_0 + \Delta\omega = \omega_p$ is the transmon frequency. The interaction strength of the resonator mode with the Josephson subsystem is taken as $g = (d_0\varepsilon_0)/\hbar$, where $d_0 = 2el(E_J / 32E_C)^{1/4}$ is the dipole moment of the transmon,

$$\varepsilon_0 = \frac{\omega_0}{l}\frac{C_g}{C_B}\sqrt{\frac{\hbar Z_0}{2}}$$

is the vacuum electric field in the resonator that affects the transmon, and l is the distance that the Cooper pair travels when tunneling through JJ [43]. The conditions for the application of the rotating wave approximation, which makes it possible to use the relation in Equation 5, are $\Delta\omega \ll \omega_0$ and $g \ll \omega_0$ [44].

Here, the efficiency of the interaction between two subsystems is determined by the average photon density $\langle N \rangle / V_{res}$, which is large enough to allow field-induced transitions to occur significantly faster than any decoherence processes in the system [29]. This actually corresponds to the strong-field regime and makes it possible to correctly describe the dynamics of a quantum system in terms of the nonstationary Schrödinger equation without taking dissipations into account [45].

The developed theoretical approach appears to be very powerful and allows one to describe the mutual influence between the superconducting and field subsystems beyond the perturbation regime with efficient excitation of transmon being taken into account. For the case of few photons in the field mode, the analytical solution of the problem is found. In the general case, the nonstationary Schrödinger equation (Equation 7) was solved numerically using the expansion of the total non-stationary wave function in terms of the interaction-free eigenfunctions of the Josephson, ϕ_n, and field, $\tilde{\phi}_k$, subsystems:

$$\Psi = \Sigma C_{n,k}(t)\phi_n\tilde{\phi}_k e^{-\frac{iE_{nk}t}{\hbar}}, \tag{9}$$

where the designation of the total energy in the system is

$$E_{n,k} = \hbar(\omega_0 + \Delta\omega)\left(n + \frac{1}{2}\right) + \hbar\omega_0\left(k + \frac{1}{2}\right).$$

Substituting the solution in Equation 9 into Equation 7 leads to a system of differential equations for probability amplitudes $C_{n,k}(t)$ to find k photons in the field mode and n-fold excitation of the transmon:

$$\begin{aligned} i\dot{C}_{n,k} &= n\Delta\omega C_{n,k} + \gamma n(n+1)C_{n,k} \\ &+ \sqrt{\frac{n(k+1)}{4}}gC_{n-1,k+1} + \sqrt{\frac{k(n+1)}{4}}gC_{n+1,k-1}. \end{aligned} \tag{10}$$

Based on the obtained solution, the probability of detecting a transmon in the state with the number n is given by:

$$P_n(t) = \Sigma_k \left|C_{n,k}(t)\right|^2. \tag{11}$$

The probability of finding k photons in the field mode can be found similarly to Equation 11 as follows:

$$W_k(t) = \Sigma_n \left|C_{n,k}(t)\right|^2. \tag{12}$$

The initial state is considered to be the Fock state of the resonator with the number of photons k_0 denoted as $\tilde{\phi}_{in} = |k_0\rangle$.

Discussion

Different regimes of transmon population dynamics

The first feature demonstrated for the interacting superconducting subsystem and a single-mode quantum field is a significant influence of the Josephson nonlinearity (which is similar to the Kerr self-phase modulation) on the dynamics of the transmon excitation. Figure 2 shows 2D distributions characterizing the time dynamics of the population of different transmon states in the case of strong and weak nonlinearity in the system. Here we see Rabi-like oscillations [46-48] between different transmon states, and the amplitude of these oscillations is characterized by slow modulation resulting from the nonlinearity effect. It is shown that even a small nonlinearity leads to the appearance of amplitude modulation, and different numbers of states are characterized by different modulation and frequency. Moreover, it is found that significantly different regimes of dynamics take place in dependence on the value of the key parameter K, which combines the characteristics of both the nonlinearity and coupling with the quantum field:

$$K = \frac{\gamma k_0(k_0+1)}{g}. \tag{13}$$

Actually, this parameter represents the ratio between the efficient nonlinearity of the transmon and the strength of its coupling with the quantum field. It is very important that the efficient nonlinearity is calculated for maximal possible transmon excitation directly determined by the initial number of photons in the field k_0. For relatively small values of the nonlinearity parameter ($K \ll 1$), a strong coupling between the field and the Josephson subsystem gives rise to periodic transition of the transmon to high-energy states, as can be clearly seen in Figure 2a. Here, all the energy initially stored in the field can be

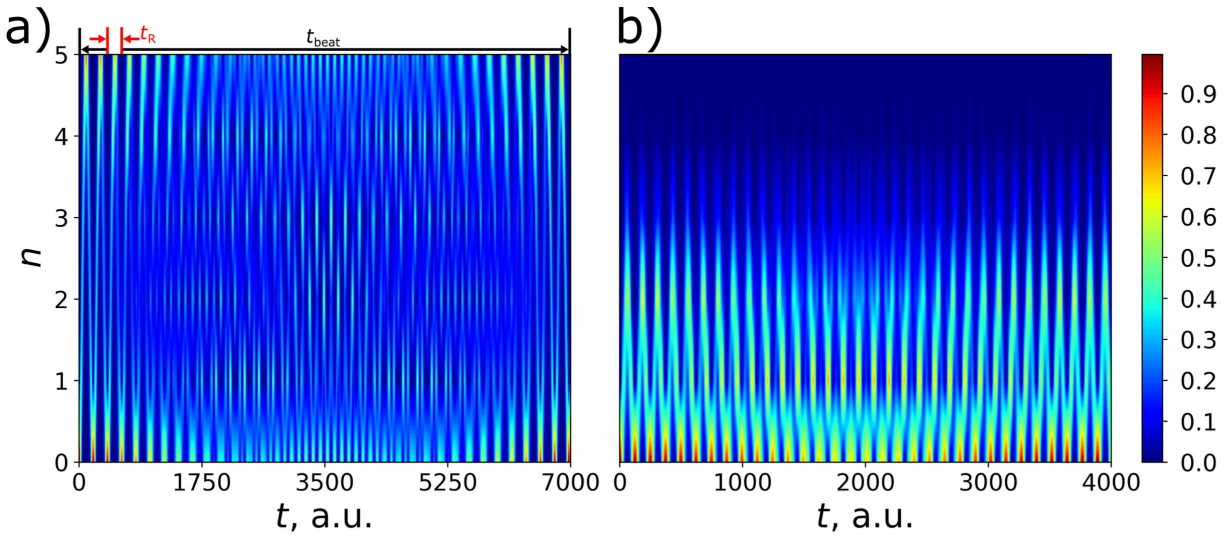

Figure 2: Distribution (colored) of the probability of transmon state excitation versus time with initial state $\psi_{in} = |0\rangle_b |5\rangle_a$ for nonlinearity parameters (a) $\gamma = -0.001\omega_0$ and (b) $\gamma = -0.01\omega_0$ for $g = 0.03\omega_0$, $\Delta\omega = 0$. The dimensionless time unit is t, which is converted to dimensional units via the formula $\tau = 2\pi t/\omega_0$.

transferred to the transmon with periodic maximal population of the highest possible excited transmon state with $n = k_0$.

An increase in the nonlinearity of the transmons leads to a significant reduction in the period of Rabi oscillations, t_R, and the beat frequency, t_{beat}, as shown in Figure 2a. When nonlinear interactions dominate, high-energy excitations are strongly suppressed. This fact is illustrated in Figure 2b.

Population control through frequency detuning

As it was shown in the previous section, the regime of strong nonlinearity, when the parameter $K > 1$, leads to suppression of excitation of high-energy transmon states. However, here we propose and discuss a method how to overcome this effect. We have found out that it is possible to controllably manage the excitations in the Kerr nonlinear transmon by varying the frequency detuning of $\Delta\omega$. Using the law of energy conservation in the case of the initial state $\psi_{in} = |0\rangle_b |k_0\rangle_a$, we have analytically found the formula to determine the optimal value of the frequency detuning that produces the maximum excitation of a certain transmon state "on demand":

$$\hbar\omega_0 k_0 + \langle W_{int}\rangle_{in} = \hbar(\omega_0 + \Delta\omega)n + \hbar\omega_0(k_0 - n) + \hbar\gamma n(n+1) + \langle W_{int}\rangle_{fin}, \tag{14}$$

where $\langle W_{int}\rangle_{in/fin}$ denotes the average value of the interaction energy in the initial and final states of the system, respectively. For an exact number of exitations in the system, the average interaction energy is zero, which means that for the case of the initial state of the transmon, $\langle W_{int}\rangle_{in} = 0$. In addition, under the condition of ensuring the maximum possible excitation, no energy should be involved in the interaction in the final state, so $\langle W_{int}\rangle_{fin} = 0$. Thus, Equation 14 implies an expression for the optimal frequency detuning at which the maximum excitation of the state with the highest number $n = k_0$ can be achieved:

$$\Delta\omega_{opt_n} = -\gamma(n+1). \tag{15}$$

It should also be emphasized that this analytical method, based on finding the integral of motion, makes it possible to predict the optimal frequency detuning without solving the system of Equation 10. Equation 15 is explicitly confirmed by the numerically calculated 2D probability distribution of the excitation of different transmon states shown in Figure 3 in dependence on frequency detuning and time.

A very well-pronounced maximum of the probability is found at optimal frequency detuning at each of the three presented distributions. It is important to note that Equation 15 is valid and can also be applied in the case of any intermediate transmon state, but in this case the characteristic peak width for the level population can be large enough to lead to some overlapping and interference patterns in the distribution (see Figure 3a,b). Physically, these lateral peaks occur in other settings when not only the desired state is involved in the excitation, but also some other neighbors. In this case, the average interaction energy in Equation 14 becomes non-zero, providing a different energy

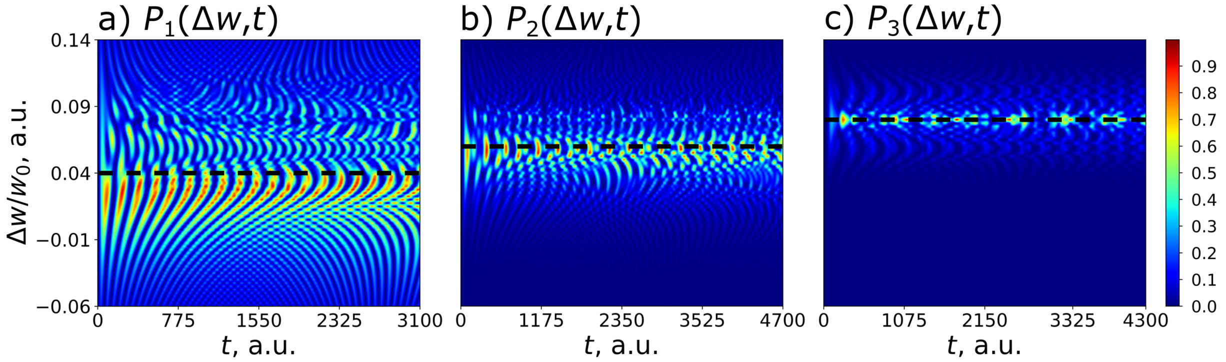

Figure 3: Distribution (colored) of the probability of transmon state excitation versus time of (a) the first, (b) the second, and (c) the third of the transmon states at $g = 0.025\omega_0$ and $\gamma = -0.02\omega_0$ as a function of the frequency detuning $\Delta\omega$ for the initial state $\psi_{\text{in}} = |0\rangle_b |3\rangle_a$. The horizontal black dashed lines correspond to the theoretical values of the detuning $\Delta\omega_{\text{opt}_n}$ obtained from Equation 15. As the transmon levels n increase, the theoretical detuning match the maximum detunings from numerical simulations $\Delta\omega_n$.

state that leads to additional preferred values of the frequency detuning.

To demonstrate more precisely the possibility of highly efficient excitation of any transmon state "on demand" by frequency detuning, we calculate the time-dependent populations of transmon levels at optimal points. The results are shown in Figure 4. In the resonance case (Figure 4a), the excitation of high-energy transmon states is strongly suppressed due to significant influence of the Kerr nonlinearity ($K = 9.6$). However, it is clearly seen that the frequency adjustments found by Equation 15 for the first (Figure 4b), second (Figure 4c), and third (Figure 4d) Fock states are indeed optimal values, providing increased excitation of the considered states. The effect of possible maximum excitation is especially pronounced for the highest transmon level when all the input energy of the quantum field is transferred to the superconducting subsystem. Thus, the optimal frequency detuning allows one to overcome the suppression of excitation induced by strong nonlinearity and to achieve a periodically maximum population of a certain transmon state "on demand".

Quantum circuit design

The optimal frequency detuning opens the possibility to achieve maximum excitation of a certain transmon state even under strong nonlinearity. In practice, however, the case where K is close to unity may be strongly demanded. This regime corresponds to a rather strong coupling between the transmon and the quantum field and can be attractive due to the possibility of much faster transmon dynamics. Moreover, as will be discussed below, the experimental control of the excitation is much easier in this case. This regime is difficult to achieve in traditional qubit-based experiments, where everyone deals with the weak coupling regime when $g/2\pi \approx 10$ MHz and $\gamma/2\pi \approx -100$ MHz. Devoret et al. [49] showed that the coupling of the JJ system with the resonator can be significantly enhanced by placing it in the gap of the central conductor of the coplanar waveguide. In this case, the JJ system will interact directly with the current (magnetic field) in the cavity, and the coupling strength will change from $g/\omega_0 \approx \sqrt{\alpha}$ to $g/\omega_0 \approx 1/\sqrt{\alpha}$, where α is a fine structure constant. This case corresponds to the so-called "ultrastrong coupling regime" [50,51], which is beyond the scope of this article.

Later, it was shown that this system is inconvenient for practical implementation because the low nonlinearity of $E_C/h \approx 5$ MHz and the huge intrinsic capacitance of JJ $C_J \approx 4$ pF are difficult to achieve. The reason was that the JJ system was located in the center of the resonator and inductive coupling prevailed. The problem can be solved by using the so-called "in-line transmon" design, that is, one should move the JJ system closer to the edge of the resonator in the area of the maximum voltage in the standing wave, where capacitive coupling will be implemented. At the same time, the value of the coupling strength will decrease, but will still remain quite large in comparison to the characteristic nonlinearity, that is, $E_C/h \approx 300$ MHz [52,53].

In this article, we turned this concept into a realistic design to demonstrate the experimental feasibility of the proposed qudit control with microwave photons. In our case, the characteristic magnitude of the nonlinearity $\gamma/2\pi = -E_C/2h = -100$ MHz is directly proportional to the charge energy E_C of the transmon, which is determined by the capacitance of the remaining part of the resonator $l_q = 549$ µm (Figure 5, the red part of the resonator). The coupling strength can be estimated as:

$$\frac{g}{2\pi} = \sqrt{\frac{2\pi Z_0 \alpha}{Z_{\text{vac}}}} \left(\frac{E_J}{2E_C}\right)^{\frac{1}{4}} \frac{\omega_p}{2\pi}, \qquad (16)$$

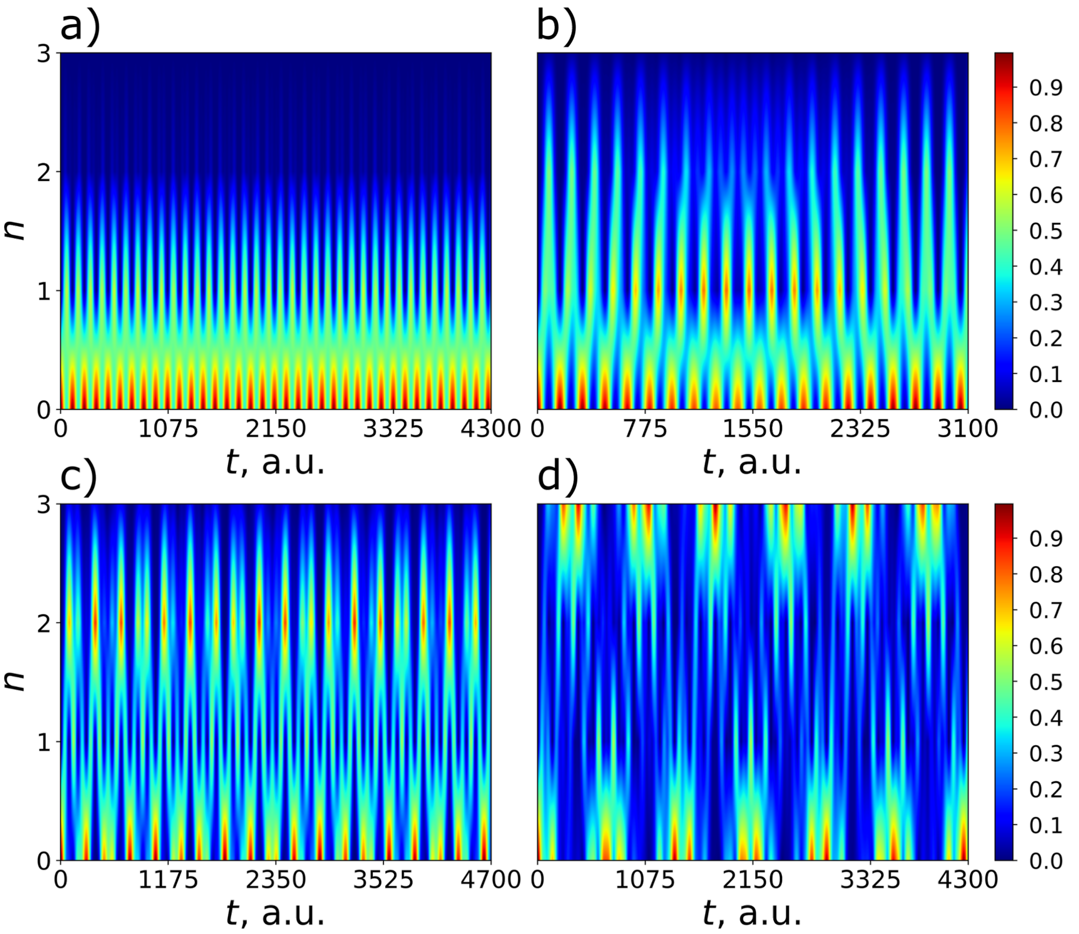

Figure 4: Distribution (colored) of the probability of transmon state excitation versus time, obtained in the case of the initial state $\psi_{\text{in}} = |0\rangle_b |3\rangle_a$ in the regime with predominant nonlinear interaction (K = 9.6) for $g = 0.025\omega_0$ and $\gamma = -0.02\omega_0$. Panel (a) corresponds to the resonant case at $\Delta\omega = 0$, panel (b) corresponds to the optimal frequency for efficient population of the first state $\Delta\omega = 0.04\omega_0$, panel (c) corresponds to the optimal frequency for efficient population of the second state $\Delta\omega = 0.06\omega_0$, and panel (d) corresponds to the optimal frequency for efficient population of the third state $\Delta\omega = 0.08\omega_0$.

and it will vary depending on the external magnetic flux ($E_J(\Phi_{\text{ext}})$ and $\omega_p/2\pi(\Phi_{\text{ext}})$). Here, $Z_{\text{vac}} \approx 377\ \Omega$ and $Z_0 = 50\ \Omega$. Taking this expression into account, at a typical plasma transmon frequency of $\omega_p/2\pi$ = 5–6 GHz, the coupling strength will be $g/2\pi \approx 1.2$ GHz, and efficient state control of the qudit will be possible for low-energy levels, n = 1–3.

Switching between effectively populated states is carried out when an external magnetic flux Φ_{ext} is applied to the interferometer, taking into account the condition $\Delta\omega_{\text{opt}_n} = -\gamma(n+1)$ (Figure 6). The tuning of the plasma frequency is regulated by the interferometric arm asymmetry, and the values of E_J determine the magnitude of the critical current and the area of each JJ: $I_{c1} \approx 39.44$ nA, $S_1 = 200 \times 197\ \text{nm}^2$, $I_{c2} \approx 22.21$ nA, and $S_2 = 149 \times 149\ \text{nm}^2$, with the usual critical current density of j = 1 μA·μm^{-2}. The frequency of the resonator was chosen to be $\omega_0/2\pi$ = 5.348 GHz to provide simultaneously strong coupling with the quantum field and optimal detuning from the resonance. In addition, this frequency determines the total length of the system, that is, $2l$ = 11.101 mm.

Let us discuss the limitations on the values of the physical parameters in this scheme. First of all, the following relation between Josephson and charge energies should be satisfied: $E_J \gg E_C$, provided in our design by the ratio $E_J/E_C \approx 100$, which correlates well with the chosen type of superconducting artificial atom. The second constraint $C_J \ll C_s = l_q C^0 \ll 2lC^0$ is also satisfied (the capacity of JJ can be estimated as $C_J = \varepsilon\varepsilon_0 S/d$, ε = 10, and d = 2 nm for an AlO$_x$ film).

This implementation has a number of significant drawbacks; the system takes up a lot of space on the chip, and the impedance matching for the JJ system and the resonator is a problem. Nevertheless, for this discussed in-line transmon design, all

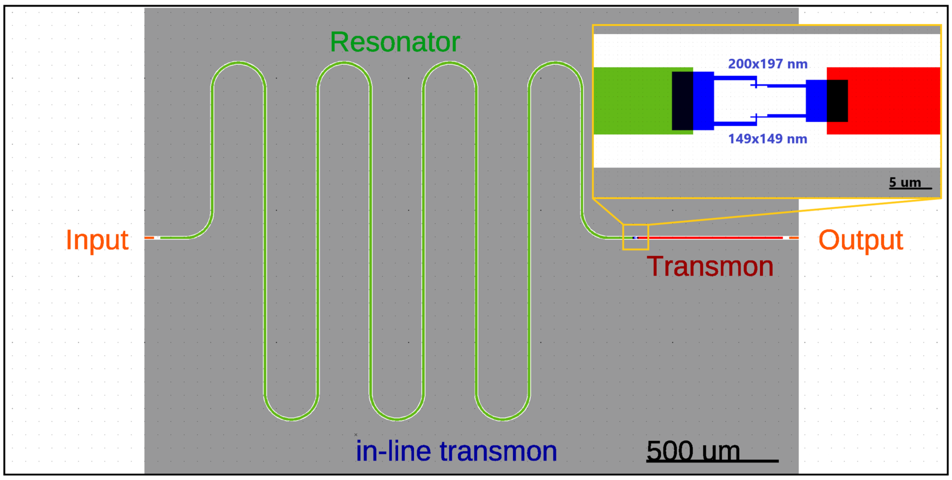

Figure 5: In-line transmon design for efficient transmission of the quantum state. The red part of the central conductor of the resonator and the blue SQUID form a transmon, the total length of the resonator (green and red parts) forms the main resonant mode ω_0.

necessary parameters are calculated and values of the coupling strength *g* corresponding to the optimal transmon frequencies predicted by Equation 15 and providing the most efficient excitation are found for the four lowest transmon states. For each considered transmon state, its population is numerically calculated as a function of frequency detuning and time at the found coupling strength to confirm the designed optimal frequency condition. The results are shown in Figure 7 and Table 1; they obviously prove that the optimal detuning providing maximum excitation of each state explicitly coincides with the value obtained in the designed scheme according to Equation 15 by varying the external magnetic flux and represented by four pink vertical lines in Figure 6 with corresponding numbers.

Moreover, it can be easily seen that the control of states is very rapid and can be performed on the sub-nanosecond time scale. Indeed, Figure 8 demonstrates the time-dependent probability of excitation of considered transmon states calculated for each

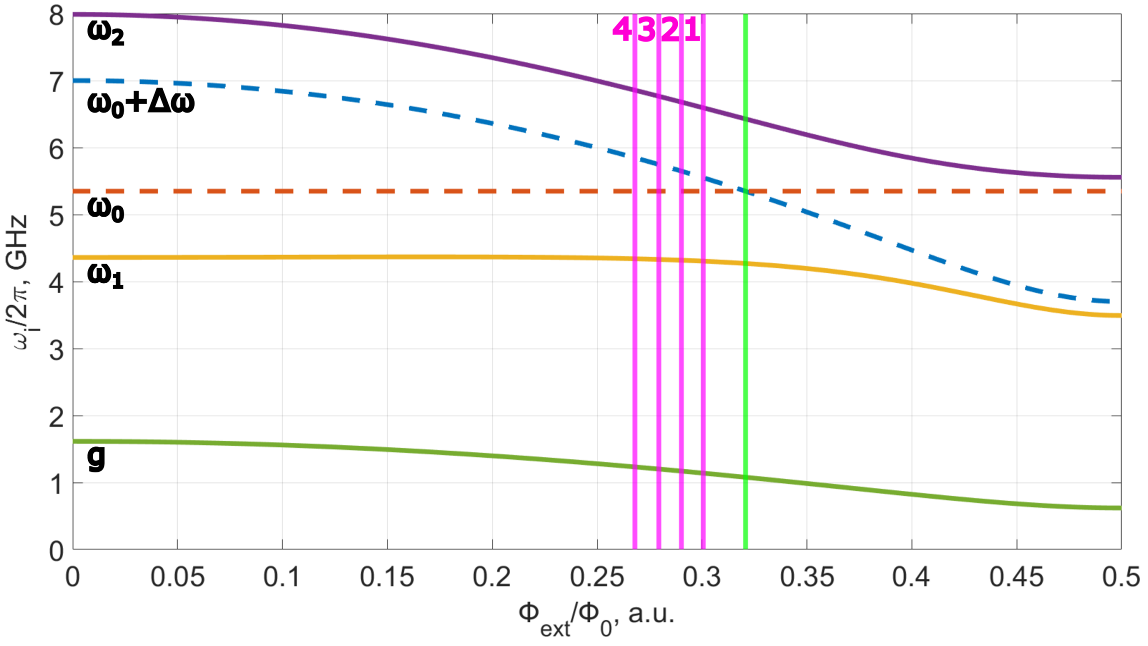

Figure 6: The dependence of the plasma frequency of the qudit $\omega_p = \omega_0 + \Delta\omega$ and coupling strength *g* between this two systems on the external magnetic flux Φ_{ext}. When these two systems are connected, the united system with two modes ω_1 and ω_2 appears. Anticrossing at the point when the frequencies of the two systems coincide corresponds to the green vertical line.

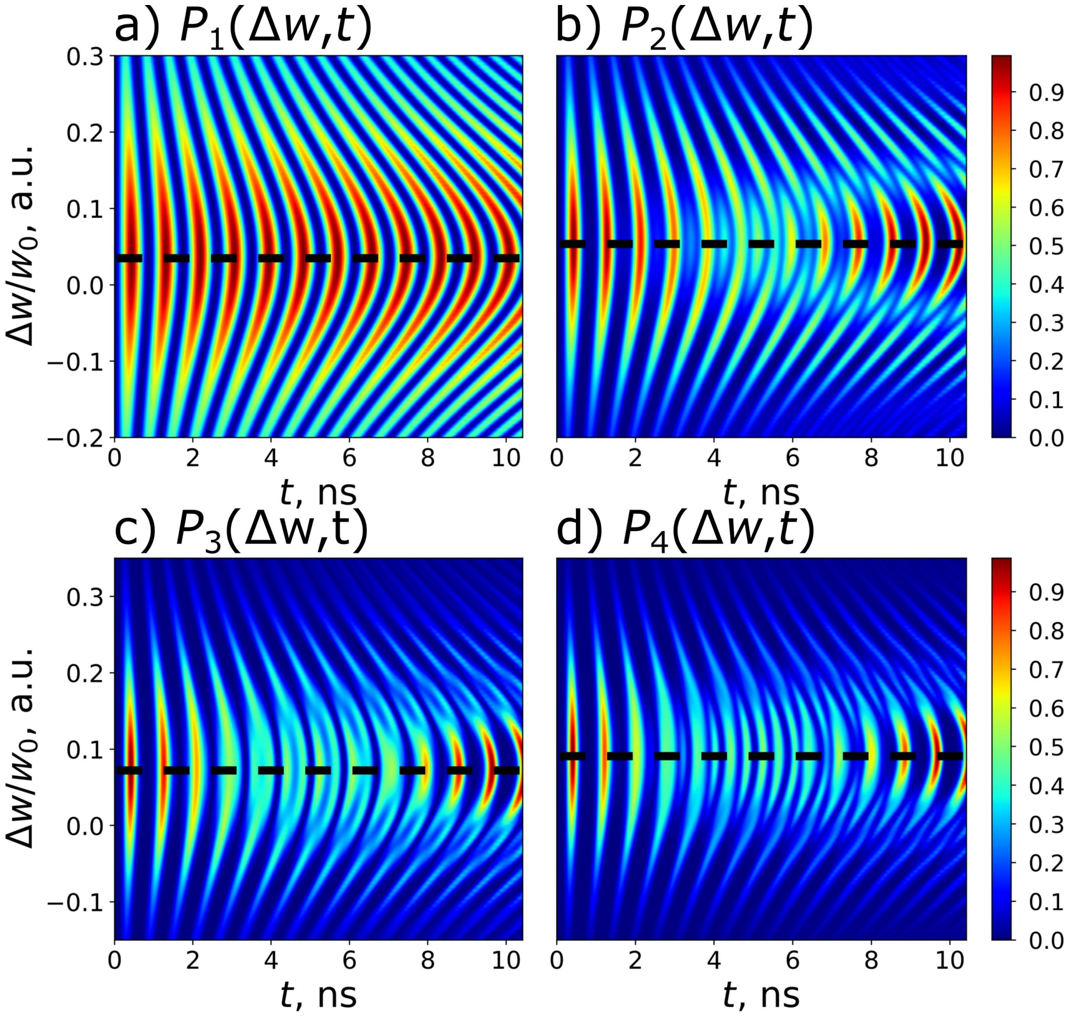

Figure 7: 2D distributions of the populations of states with n = 1–4 of the designed transmon with nonlinearity $\gamma = -0.0187\omega_0$ calculated in dependence on frequency detuning and time at certain values of the coupling strength specific for each considered state: (a) $g = 0.213\omega_0$, (b) $g = 0.219\omega_0$, (c) $g = 0.225\omega_0$, and (d) $g = 0.231\omega_0$. k_0 = 4 photons are chosen to be initially in the quantum field mode. The horizontal black dashed lines correspond to the theoretical values of the detuning (Equation 15), which is close enough to the numerical calculation results, see Table 1 for details.

Table 1: Comparison of theoretical detuning $\Delta\omega_{\mathrm{opt}_n} / \omega_0$ with detuning $\Delta\omega_n$ obtained from numerical simulations.

n	1	2	3	4
$\Delta\omega_n / \omega_0$, a.u.	0.0374	0.0561	0.0748	0.0935
$\Delta\omega_{\mathrm{opt}_n}$, a.u.	0.035	0.055	0.075	0.095

state at its own optimal detuning. The obtained results demonstrate a very fast excitation with probability equal to unity achieved for each state of the designed transmon-based qudit, even for the highest one (Table 2). Thus, the strong-coupling regime appears to be very advantageous for the rapid sub-nanosecond control of the designed transmon-based qudit. In this case a very fine tuning to the optimal frequency can be performed by varying the applied magnetic flux.

Conclusion

In this work, a fast, simple, and precise control of the population of an artificial atom is implemented theoretically using microwave photons (Fock states of the resonator). It is important to emphasize that, by adjusting the frequency of the nonlinear oscillator (qudit) from the linear resonator mode, we can choose which level of the solid-state subsystem is efficiently populated. Due to the nonlinearity, an efficient excitation of highly excited transmon states seems to be a challenging problem. It may be possible to excite this system “step by step” by choosing the appropriate frequency of the classical field for each stage, as was done in [54]. However, this procedure

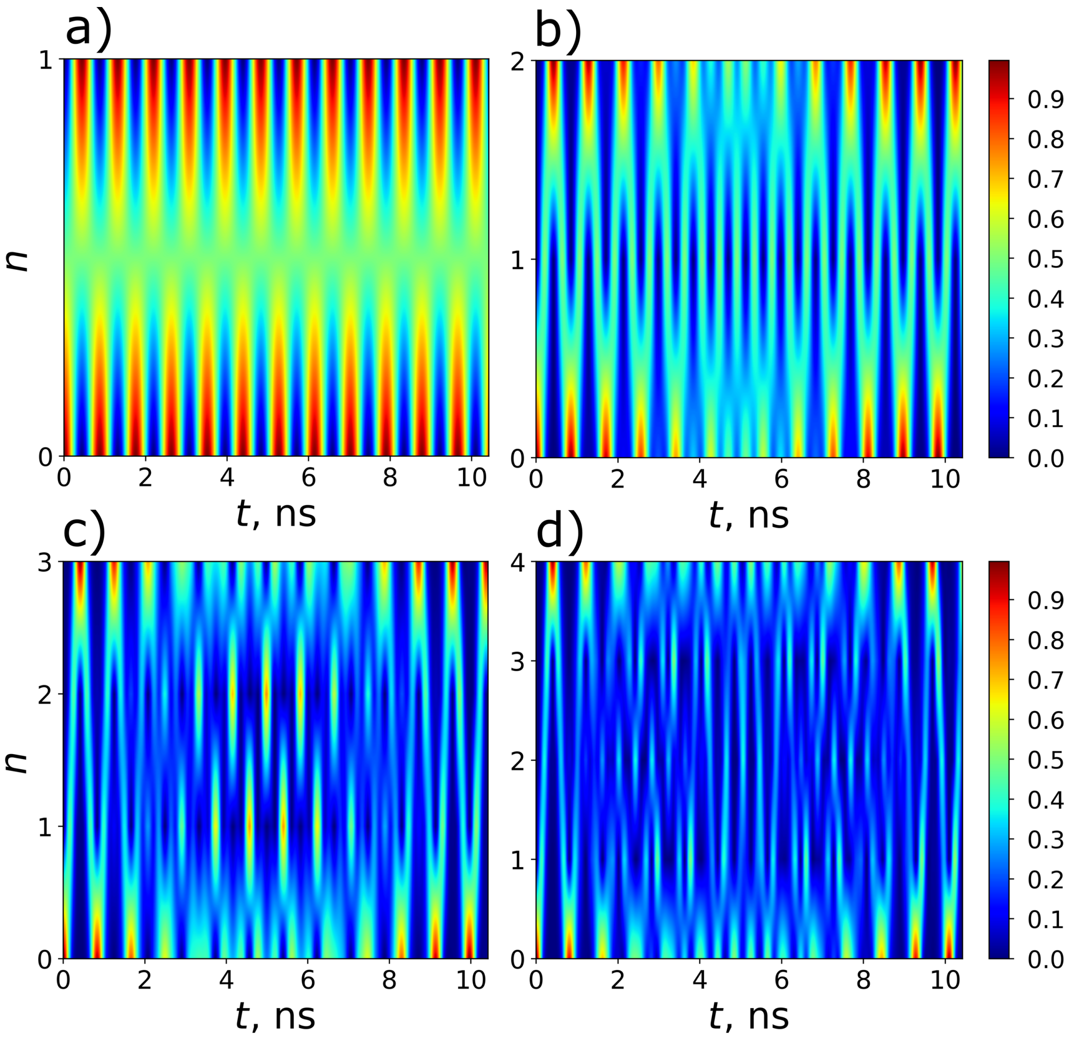

Figure 8: A demonstration of the rapid control of the states with n = 1–4 of the designed transmon (from (a) to (d), respectively). The panels show the time-dependent population of transmon states at the selected optimal frequency detuning. The parameters for each panel are the same as for the corresponding panels in Figure 7.

requires a rather complex experimental setup and takes a significant amount of time. For our particular system, we have identified and demonstrated the possibility of exciting a specific desired transmon state very quickly from the ground state (see Table 2 for details). We can significantly enhance the excitation of this specific transmon state by selecting an appropriate frequency detuning, whose value is determined analytically for each desired state. This phenomenon arises due to the interaction between nonlinearity and the coupling of quantum fields and cannot be observed when only classical fields are present.

Table 2: The maximum probability of excitation P_n of the states with n = 1–4 of the designed transmon during the time τ_n.

n	1	2	3	4
P_n, a.u.	0.999976	0.995518	0.987228	0.975867
τ_n, ns	0.438	0.427	0.417	0.405

In addition, we propose the quantum circuit design of a real superconducting scheme in which the predicted rapid control of transmon-based qudit can be demonstrated. It is important that, in a strong coupling regime, the efficient transitions in the transmon-based qudit occur on sub-nanosecond timescales [55,56]. Note that such times are not large in comparison to the decoherence process in the transmon-based qudit [29]. This circumstance makes it possible to design complex fully quantum hybrid “field + solid state” systems for quantum computing and developing a fully quantum interface between superconducting and photon platforms. Also, the developed transmon-based qudit can be used as an electromagnetic field detector, which allows one at least to determine the exact number of photons in the resonator.

Funding

The study of the basic element for quantum networking is supported by Ministry of Science and Higher Education of the Russian Federation (agreement No. 075-15-2024-538).

Author Contributions

Irina A. Solovykh: data curation; investigation; software; visualization; writing – review & editing. Andrey V. Pashchenko: formal analysis; investigation; software; visualization; writing – original draft. Natalya A. Maleeva: methodology; project administration; resources. Nikolay V. Klenov: conceptualization; methodology; validation; writing – original draft. Olga V. Tikhonova: conceptualization; data curation; investigation; methodology; writing – review & editing. Igor I. Soloviev: funding acquisition; project administration; supervision; validation.

ORCID® iDs

Irina A. Solovykh - https://orcid.org/0009-0006-2261-0055
Andrey V. Pashchenko - https://orcid.org/0000-0003-4859-6053
Nikolay V. Klenov - https://orcid.org/0000-0001-6265-3670
Olga V. Tikhonova - https://orcid.org/0000-0003-0229-5992
Igor I. Soloviev - https://orcid.org/0000-0001-9735-2720

Data Availability Statement

All data that supports the findings of this study is available in the published article and/or the supporting information of this article.

Preprint

A non-peer-reviewed version of this article has been previously published as a preprint: https://doi.org/10.3762/bxiv.2025.30.v1

References

1. Feynman, R. P. *Found. Phys.* **1986,** *16,* 507–531. doi:10.1007/bf01886518
2. Orús, R.; Mugel, S.; Lizaso, E. *Rev. Phys.* **2019,** *4,* 100028. doi:10.1016/j.revip.2019.100028
3. Kiktenko, E. O.; Pozhar, N. O.; Anufriev, M. N.; Trushechkin, A. S.; Yunusov, R. R.; Kurochkin, Y. V.; Lvovsky, A. I.; Fedorov, A. K. *Quantum Sci. Technol.* **2018,** *3,* 035004. doi:10.1088/2058-9565/aabc6b
4. Zhao, L.; Zhao, Z.; Rebentrost, P.; Fitzsimons, J. *Quantum Mach. Intell.* **2021,** *3,* 21. doi:10.1007/s42484-021-00048-8
5. Guseynov, N. M.; Zhukov, A. A.; Pogosov, W. V.; Lebedev, A. V. *Phys. Rev. A* **2023,** *107,* 052422. doi:10.1103/physreva.107.052422
6. Vozhakov, V. A.; Bastrakova, M. V.; Klenov, N. V.; Soloviev, I. I.; Pogosov, W. V.; Babukhin, D. V.; Zhukov, A. A.; Satanin, A. M. *Usp. Fiz. Nauk* **2022,** *192,* 457–476. doi:10.3367/ufnr.2021.02.038934
7. Shnyrkov, V. I.; Soroka, A. A.; Turutanov, O. G. *Phys. Rev. B* **2012,** *85,* 224512. doi:10.1103/physrevb.85.224512
8. Blok, M. S.; Ramasesh, V. V.; Schuster, T.; O'Brien, K.; Kreikebaum, J. M.; Dahlen, D.; Morvan, A.; Yoshida, B.; Yao, N. Y.; Siddiqi, I. *Phys. Rev. X* **2021,** *11,* 021010. doi:10.1103/physrevx.11.021010
9. Seifert, L. M.; Li, Z.; Roy, T.; Schuster, D. I.; Chong, F. T.; Baker, J. M. *Phys. Rev. A* **2023,** *108,* 062609. doi:10.1103/physreva.108.062609
10. Kiktenko, E. O.; Nikolaeva, A. S.; Xu, P.; Shlyapnikov, G. V.; Fedorov, A. K. *Phys. Rev. A* **2020,** *101,* 022304. doi:10.1103/physreva.101.022304
11. Liu, P.; Wang, R.; Zhang, J.-N.; Zhang, Y.; Cai, X.; Xu, H.; Li, Z.; Han, J.; Li, X.; Xue, G.; Liu, W.; You, L.; Jin, Y.; Yu, H. *Phys. Rev. X* **2023,** *13,* 021028. doi:10.1103/physrevx.13.021028
12. Nikolaeva, A. S.; Kiktenko, E. O.; Fedorov, A. K. *EPJ Quantum Technol.* **2024,** *11,* 43. doi:10.1140/epjqt/s40507-024-00250-0
13. Wehner, S.; Elkouss, D.; Hanson, R. *Science* **2018,** *362,* eaam9288. doi:10.1126/science.aam9288
14. Cacciapuoti, A. S.; Caleffi, M.; Tafuri, F.; Cataliotti, F. S.; Gherardini, S.; Bianchi, G. *IEEE Network* **2020,** *34,* 137–143. doi:10.1109/mnet.001.1900092
15. Kumar, S.; Lauk, N.; Simon, C. *Quantum Sci. Technol.* **2019,** *4,* 045003. doi:10.1088/2058-9565/ab2c87
16. Ang, J.; Carini, G.; Chen, Y.; Chuang, I.; Demarco, M.; Economou, S.; Eickbusch, A.; Faraon, A.; Fu, K.-M.; Girvin, S.; Hatridge, M.; Houck, A.; Hilaire, P.; Krsulich, K.; Li, A.; Liu, C.; Liu, Y.; Martonosi, M.; McKay, D.; Misewich, J.; Ritter, M.; Schoelkopf, R.; Stein, S.; Sussman, S.; Tang, H.; Tang, W.; Tomesh, T.; Tubman, N.; Wang, C.; Wiebe, N.; Yao, Y.; Yost, D.; Zhou, Y. *ACM Trans. Quantum Comput.* **2024,** *5,* 1–59. doi:10.1145/3674151
17. Zhou, Y.; Peng, Z.; Horiuchi, Y.; Astafiev, O. V.; Tsai, J. S. *Phys. Rev. Appl.* **2020,** *13,* 034007. doi:10.1103/physrevapplied.13.034007
18. Vozhakov, V.; Bastrakova, M.; Klenov, N.; Satanin, A.; Soloviev, I. *Quantum Sci. Technol.* **2023,** *8,* 035024. doi:10.1088/2058-9565/acd9e6
19. Pogosov, W. V.; Dmitriev, A. Y.; Astafiev, O. V. *Phys. Rev. A* **2021,** *104,* 023703. doi:10.1103/physreva.104.023703
20. Elistratov, A. A.; Remizov, S. V.; Pogosov, W. V.; Dmitriev, A. Yu.; Astafiev, O. V. *arXiv* **2023,** 2309.01444. doi:10.48550/arxiv.2309.01444
21. Zakharov, R. V.; Tikhonova, O. V.; Klenov, N. V.; Soloviev, I. I.; Antonov, V. N.; Yakovlev, D. S. *Adv. Quantum Technol.* **2024,** *7,* 2400141. doi:10.1002/qute.202400141
22. Pankratov, A. L.; Gordeeva, A. V.; Revin, L. S.; Ladeynov, D. A.; Yablokov, A. A.; Kuzmin, L. S. *Beilstein J. Nanotechnol.* **2022,** *13,* 582–589. doi:10.3762/bjnano.13.50
23. Chiarello, F.; Alesini, D.; Babusci, D.; Barone, C.; Beretta, M. M.; Buonomo, B.; D'Elia, A.; Gioacchino, D. D.; Felici, G.; Filatrella, G.; Foggetta, L. G.; Gallo, A.; Gatti, C.; Ligi, C.; Maccarrone, G.; Mattioli, F.; Pagano, S.; Piersanti, L.; Rettaroli, A.; Tocci, S.; Torrioli, G. *IEEE Trans. Appl. Supercond.* **2022,** *32,* 1–5. doi:10.1109/tasc.2022.3148693
24. Vasenko, A. S.; Hekking, F. W. J. *J. Low Temp. Phys.* **2009,** *154,* 221–232. doi:10.1007/s10909-009-9869-z
25. Ozaeta, A.; Vasenko, A. S.; Hekking, F. W. J.; Bergeret, F. S. *Phys. Rev. B* **2012,** *86,* 060509. doi:10.1103/physrevb.86.060509
26. Ozaeta, A.; Vasenko, A. S.; Hekking, F. W. J.; Bergeret, F. S. *Phys. Rev. B* **2012,** *85,* 174518. doi:10.1103/physrevb.85.174518

27. Koch, J.; Yu, T. M.; Gambetta, J.; Houck, A. A.; Schuster, D. I.; Majer, J.; Blais, A.; Devoret, M. H.; Girvin, S. M.; Schoelkopf, R. J. *Phys. Rev. A* **2007,** *76,* 042319. doi:10.1103/physreva.76.042319
28. Roth, T. E.; Ma, R.; Chew, W. C. *IEEE Antennas Propag. Mag.* **2023,** *65,* 8–20. doi:10.1109/map.2022.3176593
29. Wang, Z.; Parker, R. W.; Champion, E.; Blok, M. S. *Phys. Rev. Appl.* **2025,** *23,* 034046. doi:10.1103/physrevapplied.23.034046
30. Kristen, M.; Schneider, A.; Stehli, A.; Wolz, T.; Danilin, S.; Ku, H. S.; Long, J.; Wu, X.; Lake, R.; Pappas, D. P.; Ustinov, A. V.; Weides, M. *npj Quantum Inf.* **2020,** *6,* 57. doi:10.1038/s41534-020-00287-w
31. Houck, A. A.; Schreier, J. A.; Johnson, B. R.; Chow, J. M.; Koch, J.; Gambetta, J. M.; Schuster, D. I.; Frunzio, L.; Devoret, M. H.; Girvin, S. M.; Schoelkopf, R. J. *Phys. Rev. Lett.* **2008,** *101,* 080502. doi:10.1103/physrevlett.101.080502
32. Place, A. P. M.; Rodgers, L. V. H.; Mundada, P.; Smitham, B. M.; Fitzpatrick, M.; Leng, Z.; Premkumar, A.; Bryon, J.; Vrajitoarea, A.; Sussman, S.; Cheng, G.; Madhavan, T.; Babla, H. K.; Le, X. H.; Gang, Y.; Jäck, B.; Gyenis, A.; Yao, N.; Cava, R. J.; de Leon, N. P.; Houck, A. A. *Nat. Commun.* **2021,** *12,* 1779. doi:10.1038/s41467-021-22030-5
33. Wang, C.; Li, X.; Xu, H.; Li, Z.; Wang, J.; Yang, Z.; Mi, Z.; Liang, X.; Su, T.; Yang, C.; Wang, G.; Wang, W.; Li, Y.; Chen, M.; Li, C.; Linghu, K.; Han, J.; Zhang, Y.; Feng, Y.; Song, Y.; Ma, T.; Zhang, J.; Wang, R.; Zhao, P.; Liu, W.; Xue, G.; Jin, Y.; Yu, H. *npj Quantum Inf.* **2022,** *8,* 3. doi:10.1038/s41534-021-00510-2
34. Lvov, D. S.; Lemziakov, S. A.; Ankerhold, E.; Peltonen, J. T.; Pekola, J. P. *Phys. Rev. Appl.* **2025,** *23,* 054079. doi:10.1103/physrevapplied.23.054079
35. Rol, M. A.; Ciorciaro, L.; Malinowski, F. K.; Tarasinski, B. M.; Sagastizabal, R. E.; Bultink, C. C.; Salathe, Y.; Haandbaek, N.; Sedivy, J.; DiCarlo, L. *Appl. Phys. Lett.* **2020,** *116,* 054001. doi:10.1063/1.5133894
36. Houck, A. A.; Koch, J.; Devoret, M. H.; Girvin, S. M.; Schoelkopf, R. J. *Quantum Inf. Process.* **2009,** *8,* 105–115. doi:10.1007/s11128-009-0100-6
37. Hofheinz, M.; Weig, E. M.; Ansmann, M.; Bialczak, R. C.; Lucero, E.; Neeley, M.; O'Connell, A. D.; Wang, H.; Martinis, J. M.; Cleland, A. N. *Nature* **2008,** *454,* 310–314. doi:10.1038/nature07136
38. Hofheinz, M.; Wang, H.; Ansmann, M.; Bialczak, R. C.; Lucero, E.; Neeley, M.; O'Connell, A. D.; Sank, D.; Wenner, J.; Martinis, J. M.; Cleland, A. N. *Nature* **2009,** *459,* 546–549. doi:10.1038/nature08005
39. Peng, Z. H.; de Graaf, S. E.; Tsai, J. S.; Astafiev, O. V. *Nat. Commun.* **2016,** *7,* 12588. doi:10.1038/ncomms12588
40. Zhao, Y.-J.; Wang, C.; Zhu, X.; Liu, Y.-x. *Sci. Rep.* **2016,** *6,* 23646. doi:10.1038/srep23646
41. Dmitriev, A. Y.; Shaikhaidarov, R.; Antonov, V. N.; Hönigl-Decrinis, T.; Astafiev, O. V. *Nat. Commun.* **2017,** *8,* 1352. doi:10.1038/s41467-017-01471-x
42. Dmitriev, A. Y.; Shaikhaidarov, R.; Hönigl-Decrinis, T.; de Graaf, S. E.; Antonov, V. N.; Astafiev, O. V. *Phys. Rev. A* **2019,** *100,* 013808. doi:10.1103/physreva.100.013808
43. Blais, A.; Grimsmo, A. L.; Girvin, S. M.; Wallraff, A. *Rev. Mod. Phys.* **2021,** *93,* 025005. doi:10.1103/revmodphys.93.025005
44. Popolitova, D. V.; Tikhonova, O. V. *Laser Phys. Lett.* **2019,** *16,* 125301. doi:10.1088/1612-202x/ab570b
45. Tikhonova, O. V.; Vasil'ev, A. N. *J. Phys.: Condens. Matter* **2023,** *35,* 115301. doi:10.1088/1361-648x/acaf1f
46. Johansson, J.; Saito, S.; Meno, T.; Nakano, H.; Ueda, M.; Semba, K.; Takayanagi, H. *Phys. Rev. Lett.* **2006,** *96,* 127006. doi:10.1103/physrevlett.96.127006
47. Claudon, J.; Zazunov, A.; Hekking, F. W. J.; Buisson, O. *Phys. Rev. B* **2008,** *78,* 184503. doi:10.1103/physrevb.78.184503
48. Shevchenko, S. N.; Omelyanchouk, A. N.; Zagoskin, A. M.; Savel'ev, S.; Nori, F. *New J. Phys.* **2008,** *10,* 073026. doi:10.1088/1367-2630/10/7/073026
49. Devoret, M. H.; Girvin, S.; Schoelkopf, R. *Ann. Phys. (Berlin, Ger.)* **2007,** *519,* 767–779. doi:10.1002/andp.200751910-1109
50. Andersen, C. K.; Blais, A. *New J. Phys.* **2017,** *19,* 023022. doi:10.1088/1367-2630/aa5941
51. Frisk Kockum, A.; Miranowicz, A.; De Liberato, S.; Savasta, S.; Nori, F. *Nat. Rev. Phys.* **2019,** *1,* 19–40. doi:10.1038/s42254-018-0006-2
52. Bourassa, J.; Beaudoin, F.; Gambetta, J. M.; Blais, A. *Phys. Rev. A* **2012,** *86,* 013814. doi:10.1103/physreva.86.013814
53. Hyyppä, E.; Kundu, S.; Chan, C. F.; Gunyhó, A.; Hotari, J.; Janzso, D.; Juliusson, K.; Kiuru, O.; Kotilahti, J.; Landra, A.; Liu, W.; Marxer, F.; Mäkinen, A.; Orgiazzi, J.-L.; Palma, M.; Savytskyi, M.; Tosto, F.; Tuorila, J.; Vadimov, V.; Li, T.; Ockeloen-Korppi, C.; Heinsoo, J.; Tan, K. Y.; Hassel, J.; Möttönen, M. *Nat. Commun.* **2022,** *13,* 6895. doi:10.1038/s41467-022-34614-w
54. Peterer, M. J.; Bader, S. J.; Jin, X.; Yan, F.; Kamal, A.; Gudmundsen, T. J.; Leek, P. J.; Orlando, T. P.; Oliver, W. D.; Gustavsson, S. *Phys. Rev. Lett.* **2015,** *114,* 010501. doi:10.1103/physrevlett.114.010501
55. Klenov, N. V.; Kuznetsov, A. V.; Soloviev, I. I.; Bakurskiy, S. V.; Tikhonova, O. V. *Beilstein J. Nanotechnol.* **2015,** *6,* 1946–1956. doi:10.3762/bjnano.6.199
56. Bastrakova, M.; Klenov, N.; Ruzhickiy, V.; Soloviev, I.; Satanin, A. *Supercond. Sci. Technol.* **2022,** *35,* 055003. doi:10.1088/1361-6668/ac5505

License and Terms

BEILSTEIN JOURNAL OF NANOTECHNOLOGY

Energy spectrum and quantum phase transition of the coupled single spin and an infinitely coordinated Ising chain

Seidali Seidov*[1,2], Natalia Pugach[1] and Anatolie Sidorenko[3,4]

Full Research Paper

Open Access

Address:
[1]HSE University, Moscow, Russia, [2]NUST MISIS, Moscow, Russia, [3]Technical University of Moldova, Institute of Electronic Engineering and Nanotechnologies, Republic of Moldova and [4]Moscow Institute of Physics and Technology, Dolgoprudny, Russia

Email:
Seidali Seidov* - alikseidov@yandex.ru

* Corresponding author

Keywords:
Ising chain; Lipkin–Meshkov–Glick model; quantum phase transitions

Beilstein J. Nanotechnol. **2025,** *16,* 1668–1676.
https://doi.org/10.3762/bjnano.16.117

Received: 29 April 2025
Accepted: 22 August 2025
Published: 24 September 2025

This article is part of the thematic issue "Superconducting artificial neural networks and quantum circuits".

Associate Editor: J. M. van Ruitenbeek

Abstract

In this work we consider a spin model composed of a single spin and connected to an infinitely coordinated Ising chain. Theoretical models of this type arise from various fields of theoretical physics, such as theory of open systems, quantum control, and quantum computations. In the thermodynamic limit of an infinite chain, we map the chain Hamiltonian to the Hamiltonian of the Lipkin–Meshkov–Glik model, and the system as a whole is described by a generalized Rabi Hamiltonian. Next, the effective Hamiltonian is obtained using the Foulton–Gouterman transformation. In the thermodynamic limit we obtain the spectrum of the whole system and study the properties of the ground-state quantum phase transition.

Introduction

In the present manuscript, we consider a single spin connected to an infinitely coordinated Ising chain. From a purely theoretical point of view, this model arises when studying the physics of open systems [1,2]. In this case, the chain is modelling the external environment to which the single spin is connected. In such models, it is convenient to study not only Markovian dynamics of the single spin, but also non-Markovian dynamics going beyond the limitations of the Lindblad master equation [3-6]. The approach is to find the dynamics of the whole system (i.e., the chain and the single spin) and then trace out the chain degrees of freedom, ending up with the master equation for the single-spin density matrix. One might choose to make or not to make the Markov approximation, obtaining different types of master equations. Given that the exact solution is known, different master equation solutions can be compared against it. This allows to study the limits of applicability of the Markovian approximation, and also the correct way of introducing the Lindblad dissipation operators. These problems remain important in the general field of open quantum systems, extending beyond spin models [7-9].

One of the practical applications is modelling of certain quantum computing layouts, if one considers spins as qubits. In particular, we have previously proposed a method for implementing a CCZ (control–control–Z) quantum gate on a system composed of three logical qubits, which are connected to another coupler qubit [10]. This approach allows to increase the fidelity of the operation, and it has technical benefits such as simplicity of calibration and suppression of the unwanted longitudinal ZZ interaction. One of the important quantities is the shift of the coupler qubits energy levels depending on the state of the logical qubits. In the present manuscript, we find the energy levels of such system in the limit of infinitely many logical qubits, and find the energy spectrum of the coupler qubit depending on the state of the logical qubits ensemble.

We start our theoretical analysis by mapping the Ising chain Hamiltonian to a Lipkin– Meshkov–Glik (LMG) Hamiltonian [11-13]. The Hamiltonian of the whole system then becomes akin to the Hamiltonian of the generalized Rabi model, but with the bosonic field replaced by the collective spin of the LMG model. Next, it is diagonalized in the spin space using the Fulton–Gouterman transformation and we obtain an effective Hamiltonian. In the limit of infinite Ising chain, or equivalently of the infinite total spin, the LMG Hamiltonian can be solved exactly. We exploit this fact and analytically obtain the energy spectrum of the whole system. Based on this result, we study the structure of the extrema of the ground state energy and the consequent properties of different phases of the system.

Model

We consider a single spin coupled to a fully connected Ising chain with the Hamiltonian

$$\begin{aligned} H &= \frac{\omega}{2}\tau_z + \frac{\Delta}{2}\tau_x + H_{\text{chain}} + H_{\text{int}} \\ H_{\text{chain}} &= \frac{1}{2}\sum_{i=1}^{N}\left(\tilde{\omega}\sigma_z^i + \tilde{\Delta}\sigma_x^i\right) + \frac{J}{4N}\sum_{i\neq j}^{N}\sigma_z^i\sigma_z^j \\ H_{\text{int}} &= \frac{\tilde{J}}{2}\tau_z\sum_{i=1}^{N}\sigma_z^i. \end{aligned} \tag{1}$$

Here, $\tau_{x,z}$ are the Pauli matrices describing the single spin, and $\sigma_{x,z}^i$ are the Pauli matrices describing spins in the Ising chain. This model arises when one studies spin-bath theoretical models in studies of quantum control and design of qubit layouts in quantum computation. The coupling between the spins in the chain is rescaled by $1/N$ factor in order to obtain a finite energy per spin $\langle H\rangle/N$ in the thermodynamic limit.

Let us first consider the Hamiltonian $H_{\text{chain}} + H_{\text{int}}$. By introducing collective spin operators

$$S_{x,z} = \frac{1}{2}\sum_{i=1}^{N}\sigma_{x,z}^i \tag{2}$$

the Hamiltonian is brought in the following form [14,15]:

$$H_{\text{chain}} + H_{\text{int}} = \left(\tilde{\omega} + \frac{\tilde{J}}{2}\tau_z\right)S_z + \tilde{\Delta}S_x + \frac{J}{2S}S_z^2. \tag{3}$$

Here, $S = N/2$ is the total spin of the chain. This is a well-known Lipkin–Meshkov–Glick (LMG) Hamiltonian which we will further denote as $H_{\text{LMG}} = H_{\text{chain}} + H_{\text{int}}$. The total Hamiltonian now can be written as a 2 × 2 block matrix in the single-spin Hilbert space:

$$H = \frac{1}{2}\begin{pmatrix}\omega & \Delta \\ \Delta & -\omega\end{pmatrix} + \begin{pmatrix} H_{\text{LMG}}^{+} & 0 \\ 0 & H_{\text{LMG}}^{-}\end{pmatrix}. \tag{4}$$

Here $H_{\text{LMG}}^{\pm}$ are the Hamiltonians H_{LMG} corresponding to eigenvalues ±1 of τ_z. These types of Hamiltonians are the Hamiltonians of the generalized Rabi models. These describe a two-level system connected not to a single bosonic mode, but to a more complicated environment [16-18].

Diagonalization in the Spin Space

The Hamiltonian in the spin space can be diagonalized using the formula for the determinant of a 2 × 2 block matrix. This is also known as the Fulton–Gouterman transformation [19]. This leads to two effective Hamiltonians in the chain Hilbert space, corresponding to the state of the single spin. These are:

$$\begin{aligned} H_{\text{eff}}^{\pm} &= \pm\frac{\omega}{2} + H_{\text{LMG}}^{\pm} - \frac{\Delta^2}{4}G_{\mp} \\ G_{\pm} &= \left(\pm\frac{\omega}{2} + H_{\text{LMG}}^{\pm} - E\right)^{-1}. \end{aligned} \tag{5}$$

Operators $G_{\pm}$ are the Green functions of the Hamiltonians $\pm\omega/2 + H_{\text{LMG}}^{\pm}$. Both of these Hamiltonians contain full information about the system, so it is sufficient to consider only one of them. We will choose the Hamiltonian $H_{\text{eff}} = H_{\text{eff}}^{+}$ as the effective Hamiltonian. Given the eigenenergies $\varepsilon_n^{\pm}$ and eigenstates $|n^{\pm}\rangle$ of the Hamiltonian $\pm\omega/2 + H_{\text{LMG}}^{\pm}$, the effective Hamiltonian can be written as:

$$H_{\text{eff}} = \sum_{n=1}^{N} \varepsilon_n^{+} \left|n^{+}\right\rangle\left\langle n^{+}\right| - \frac{\Delta^2}{4} \sum_{n=1}^{N} \frac{\left|n^{-}\right\rangle\left\langle n^{-}\right|}{\varepsilon_n^{-} - E}. \tag{6}$$

The eigenenergies of the whole system are solutions of the equation $\lambda(E) = E$, where $\lambda(E)$ are the eigenvalues of H_{eff}. In principle, solutions of this equation are exactly the energy levels of the corresponding physical system. However, given that in practice an analytical solution is impossible in most cases, a usual approach is to substitute some values of energy E_0 on the left hand side and look for corrections. Our approach will be to find some kind of relation between the Hamiltonians H^{+}_{LMG} and H^{-}_{LMG}, which will allow us to express the eigenstates of one Hamiltonian via the eigenstates of the other. Then, the equation $\lambda(E) = E$ will be quadratic with two solutions, corresponding to two states of the single spin.

Limit of Strong Single-Spin–Chain Coupling

We focus on the limit of large coupling between the single spin and the chain (i.e., large $\tilde{J}$). In practice, this can be realized by coupling a single spin to an ensemble of noninteracting spins, such that the ensemble interacts only indirectly through the external spin. In this case, spins in the chain are mostly aligned along the z-axis due to the large $\tilde{J}\tau_z S_z$ term. Effectively, an interaction with the single spin creates a strong magnetic field parallel to the single spin direction. Thus, the perpendicular component of the "magnetic field" $\tilde{\Delta} S_x$ can be considered as a small perturbation. Formally, this means that we can divide the LMG Hamiltonian into the main part

$$H^{0}_{\text{LMG}} = \left(\tilde{\omega} + \frac{\tilde{J}}{2}\tau_z\right) S_z + \frac{J}{2S} S_z^2 \tag{7}$$

and the perturbation $V = \tilde{\Delta} S_x$. With the standard perturbation theory approach, we find the energy levels of H_{LMG} up to second order in $\tilde{\Delta}$:

$$\begin{aligned}
\varepsilon_\sigma^{\pm} &= \varepsilon^{(0)}_{\pm,\sigma} + \sum_{\sigma' \neq \sigma} c_{\sigma\sigma'} \\
\varepsilon^{(0)}_{\pm,\sigma} &= \left(\tilde{\omega} \pm \frac{\tilde{J}}{2}\right)\sigma + \frac{J}{2S}\sigma^2 \\
c^{\pm}_{\sigma\sigma'} &= \tilde{\Delta}^2 \frac{\left|\left\langle \sigma' \right| S_x \left| \sigma \right\rangle\right|^2}{E^{(0)}_{\pm,\sigma} - E^{(0)}_{\pm,\sigma'}}.
\end{aligned} \tag{8}$$

Here, $S_z|\sigma\rangle = \sigma|\sigma\rangle$. Accordingly, the eigenstates are

$$\left|\psi_\sigma^{\pm}\right\rangle \approx \left|\sigma\right\rangle + \sum_{\sigma' \neq \sigma} c^{\pm}_{\sigma\sigma'} \left|\sigma'\right\rangle. \tag{9}$$

As discussed earlier, we aim to relate H^{+}_{LMG} and H^{-}_{LMG}. Let us express the projectors on states $\left|\psi_\sigma^{+}\right\rangle$ via projectors on $\left|\psi_\sigma^{-}\right\rangle$. Up to the second order in $\tilde{\Delta}$:

$$\begin{aligned}
\left|\psi_\sigma^{+}\right\rangle\left\langle\psi_\sigma^{+}\right| &= \left|\psi_\sigma^{-}\right\rangle\left\langle\psi_\sigma^{-}\right| \\
&\quad + \sum_{\sigma'} \left(c^{+}_{\sigma\sigma'} - c^{-}_{\sigma\sigma'}\right)\left(\left|\psi_\sigma^{-}\right\rangle\left\langle\sigma\right| + \left|\sigma\right\rangle\left\langle\psi_\sigma^{-}\right|\right).
\end{aligned} \tag{10}$$

The Hamiltonians $H^{\pm}_{\text{LMG}}$ now can be written as:

$$\begin{aligned}
H^{+}_{\text{LMG}} &= \sum_{\sigma} E_\sigma^{+} \left|\psi_\sigma^{-}\right\rangle\left\langle\psi_\sigma^{-}\right| \\
&\quad + \sum_{\sigma\sigma'} \varepsilon_\sigma^{+} \left(c^{+}_{\sigma\sigma'} - c^{-}_{\sigma\sigma'}\right)\left(\left|\psi_\sigma^{-}\right\rangle\left\langle\sigma\right| + \left|\sigma\right\rangle\left\langle\psi_\sigma^{-}\right|\right) \\
H^{-}_{\text{LMG}} &= \sum_{\sigma} \varepsilon_\sigma^{-} \left|\psi_\sigma^{-}\right\rangle\left\langle\psi_\sigma^{-}\right|.
\end{aligned} \tag{11}$$

One can see that the leading order H^{+}_{LMG} is expressed via projectors on the eigenstates of H^{-}_{LMG}. The extra terms, when substituted in the effective Hamiltonian, will lead to higher order corrections and will be insignificant. Indeed, substituting in (Equation 6) we find:

$$\begin{aligned}
H_{\text{eff}} &= \sum_{\sigma} \left(\frac{\omega}{2} + \varepsilon_\sigma^{+} - \frac{\Delta^2}{4\left(E_\sigma^{-} - \omega/2 - E\right)}\right)\left|\psi_\sigma^{-}\right\rangle\left\langle\psi_\sigma^{-}\right| \\
&\quad + \sum_{\sigma\sigma'} \varepsilon_\sigma^{+} \left(c^{+}_{\sigma\sigma'} - c^{-}_{\sigma\sigma'}\right)\left(\left|\psi_\sigma^{-}\right\rangle\left\langle\sigma\right| + \left|\sigma\right\rangle\left\langle\psi_\sigma^{-}\right|\right).
\end{aligned} \tag{12}$$

The first term is diagonal in the basis $\left|\psi_\sigma^{-}\right\rangle$, so its contribution to the eigenvalues of the effective Hamiltonian eigenvalues will be of second order in $\tilde{\Delta}$ (as it is the order to which we have expanded $\varepsilon_\sigma^{\pm}$). The second term is of second order in $\tilde{\Delta}$ and off-diagonal, so its contribution will be of fourth order in $\tilde{\Delta}$. Thus, up to the second order in $\tilde{\Delta}$, the energy E of the whole system is defined by the following equation:

$$\frac{\omega}{2} + \varepsilon_\sigma^{+} - \frac{\Delta^2}{4\left(\varepsilon_\sigma^{-} - \omega/2 - E\right)} = E, \tag{13}$$

from which follows

$$E_\sigma^\pm = \frac{1}{2}\left(\varepsilon_\sigma^+ + \varepsilon_\sigma^- \pm \sqrt{\left(\omega + \varepsilon_\sigma^+ - \varepsilon_\sigma^-\right)^2 + \Delta^2}\right). \tag{14}$$

Also, from these calculations follows that the eigenstates are $\left|\psi_\sigma^-\right\rangle$. One might wonder why there is no contribution from $\left|\psi_\sigma^+\right\rangle$, given that our choice between expanding the Hamiltonian (Equation 13) in $\left|\psi_\sigma^-\right\rangle\left\langle\psi_\sigma^-\right|$ or $\left|\psi_\sigma^+\right\rangle\left\langle\psi_\sigma^+\right|$ was arbitrary. In fact, there is indeed no difference between choosing one over the other, because $\left\langle\psi_\sigma^-\middle|\psi_\sigma^+\right\rangle = \delta_{\sigma\sigma'} + \mathcal{O}\left(\tilde{\Delta}^4\right)$.

We also note that the same spectrum corresponds to the single-spin Hamiltonian

$$H = \frac{1}{2}\begin{pmatrix}\omega & \Delta \\ \Delta & -\omega\end{pmatrix} + \begin{pmatrix}\varepsilon_{\mathrm{LMG}}^+ & 0 \\ 0 & \varepsilon_{\mathrm{LMG}}^-\end{pmatrix}. \tag{15}$$

This Hamiltonian can be obtained if one replaces $H_{\mathrm{LMG}}^\pm$ by their eigenvalues $\varepsilon_{\mathrm{LMG}}^\pm$ in Equation 4. This is a Born–Oppenheimer approximation in which the chain is considered to be a fast subsystem relative to the single spin. In particular, the energy of the spin chain is a contribution to the potential energy of the single spin.

Phase Transition in the Thermodynamic Limit

Phase transition of the bare LMG model

In the thermodynamic classical limit, the spin operators in the LMG model can be replaced by classical expectation values (i.e., $S_z = S\cos\theta$, $S_x = S\sin\theta\cos\varphi$, $S_y = S\sin\theta\sin\varphi$). The Hamiltonian is then replaced by its classical energy profile, which is defined according to [12] as:

$$\begin{aligned}\varepsilon^\pm(\theta,\varphi) &= \lim_{S\to\infty}\frac{\left\langle H_{\mathrm{LMG}}^\pm\right\rangle}{S} \\ &= \left(\tilde{\omega} \pm \frac{\tilde{J}}{2}\right)\cos\theta + \frac{J}{2}\cos^2\theta + \tilde{\Delta}\sin\theta\cos\varphi.\end{aligned} \tag{16}$$

The average is taken over a spin coherent state $|\theta,\varphi\rangle$. It is known that the LMG Hamiltonian has two distinct phases in the thermodynamic limit [12,20-22]. The symmetric phase, in which $|\langle S_z\rangle| = S$, is realized when the linear part in S_z term in the Hamiltonian dominates over the quadratic one. In our particular case, this means competition between the values of coefficients $\tilde{\omega} + \tilde{J}\tau_z/2$ and J in the Hamiltonian (Equation 3). The second broken symmetry phase, in which the energy profile has two minima at $\left\langle S_z\right\rangle = \pm S_z^0$, is realized in the opposite case, when the S_z^2 term dominates over the ~S_z term. These minima are degenerate if $\tilde{\Delta} = 0$, otherwise one is lower than the other. The plot of the LMG model energy as a function of the angle θ is presented in Figure 1.

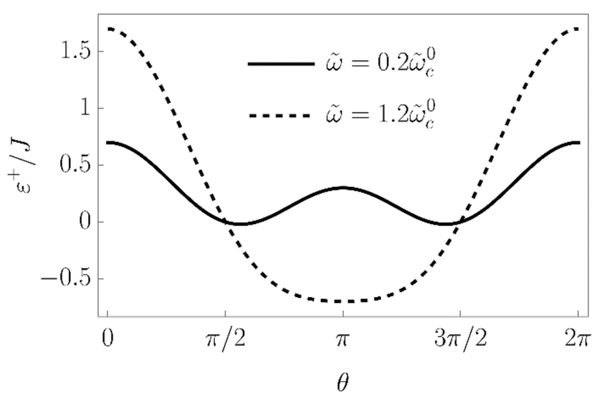

Figure 1: Energy profile (Equation 16) of the LMG model in the thermodynamic limit as a function of θ at φ = 0 and $\tilde{\Delta}$ = 0. The solid line corresponds to the broken symmetry phase with two stable minima, and the dashed line to the symmetric phase with a single minimum at θ = π.

We wished to study the phase transition of the bare LMG model (i.e., decoupled from the external spin) and in the next section we will compare the results with the ones for the LMG model coupled to the external spin. First, we have to find the extrema of the LMG model energy $\varepsilon = \varepsilon^+\left(\tilde{J} = 0\right)$. They are defined by the following equations:

$$\begin{aligned}&\frac{\partial\varepsilon}{\partial\theta} = 0 \Rightarrow \sin\theta\left(J\cos\theta + \tilde{\omega}\right) - \tilde{\Delta}\cos\theta\cos\varphi = 0 \\ &\frac{\partial\varepsilon}{\partial\varphi} = 0 \Rightarrow \tilde{\Delta}\sin\theta\sin\varphi = 0.\end{aligned} \tag{17}$$

One of the solutions is sinθ = 0 and cosφ = 0; it corresponds to the symmetric phase in which $|\langle S_z\rangle| = |S\cos\theta| = S$. The second solution corresponds to sinφ = 0 and

$$\cos\theta + \frac{\tilde{\omega}\sin\theta}{J\sin\theta - \tilde{\Delta}} = 0. \tag{18}$$

It describes the broken symmetry phase in which $|\langle S_z\rangle| \neq S$.

We found the critical values of the parameters, at which the phase transition occurs, by checking the stability of the symmetric phase. Namely, if it is stable, the sinθ = 0 and cosφ = 0 extremum is a minimum in the θ direction, and the second derivative of $\varepsilon^+(\theta,\varphi)$ with respect to θ is positive. Otherwise, the said extremum is a maximum and the stable phase is the broken symmetry one. When carrying out the calculations, we should choose the $\theta = \pi$ solution of the equation $\sin\theta = 0$, since the $\sim S_z$ contribution to the energy is positive and the ground state corresponds to $S_z = \cos\pi = -S$. The $\theta = 0$ solution corresponds to the maximum of the energy profile. Thus, we find:

$$\frac{\partial^2}{\partial\theta^2}\varepsilon^+\bigg|_{\theta=\pi,\varphi=0} = \tilde{\omega} - J. \tag{19}$$

Therefore, the broken symmetry phase exists (i.e., the expression above is negative) for $\tilde{\omega} < \tilde{\omega}_c^0 = J$. The projection of the spin on the z-axis in the broken symmetry phase is $S_z^0 = S\cos\theta_0$, where θ_0 is the solution of Equation 18. If $\tilde{\Delta} = 0$, the solutions are $\cos\theta_0 = \tilde{\omega}/J = \tilde{\omega}/\tilde{\omega}_c^0$. The plots of the energy profile $\varepsilon^+(\theta,\varphi)$ in symmetric and broken symmetry phases are presented in Figure 1.

Phase transition of the LMG model coupled to a single spin

Next, we study the properties of the phase transition if the chain is coupled to the external single spin. In this case, we have to minimize the ground state energy of the whole system. From Equation 14 we find the spectrum:

$$E^{\pm}(\theta,\varphi) = \frac{1}{2}\left(\begin{array}{c}\varepsilon^+(\theta,\varphi) + \varepsilon^-(\theta,\varphi) \\ \pm\sqrt{\left[\omega + \varepsilon^+(\theta,\varphi) - \varepsilon^-(\theta,\varphi)\right]^2 + \Delta^2}\end{array}\right). \tag{20}$$

These functions also have nontrivial minima structure depending on the values of the parameters, see Figure 2. Again, from equations $\partial_\theta E^- = 0$ and $\partial_\varphi E^- = 0$ we find that the extrema of the ground state energy are defined by equations

$$\begin{gathered}\sin\varphi\sin\theta = 0 \\ \left(\tilde{\Delta}\cos\varphi - J\sin\theta\right)\cos\theta - \tilde{\omega}\sin\theta = \frac{\tilde{J}\left(\omega + \tilde{J}\cos\theta\right)\sin\theta}{2\sqrt{\left(\omega + \tilde{J}\cos\theta\right)^2 + \Delta^2}}.\end{gathered} \tag{21}$$

The second equation defines $\langle S_z\rangle$ in the broken symmetry phase, analogously to Equation 18. In general, it has up to nine real solutions on the interval $\theta \in [0,2\pi]$ depending on the values of the parameters. For $\tilde{\Delta} = 0$, three of them are $\theta = 0, \pi, 2\pi$ as it follows from the condition $\sin\theta = 0$. Nonzero $\tilde{\Delta}$ will shift these solutions and corrections due to small $\tilde{\Delta}$which can be found by expanding the equation at said points. Six other solutions cannot be analytically found; however, we can study the properties of the energy profile exploiting the following facts: 1) due to the 2π-periodicity of $E^{\pm}(\theta,\varphi)$, the extrema at $\theta = 0, 2\pi$ are of the same type. 2) Three of unknown extrema are on the interval $\theta \in (0,\pi)$ and the other three are on the interval $\theta \in (\pi,2\pi)$. 3) A maximum should be followed by a minimum and vice versa.

Additional extrema arise due to hybridization between the energy levels $\varepsilon^{\pm}(\theta,\varphi)$ of the bare LMG model with the single spin directed up or down, leading to the appearance of avoided crossings and richer extremum structure of the ground state energy. The extrema at $\theta = 0, \pi, 2\pi$ always exist and could be either minima or maxima and the six other ones might be minima, maxima, or not exist. This allows us to list all possible extrema configurations of the energy profile. We group them into two types: either minima at $\theta = 0, 2\pi$ and $\theta = \pi$ are of different types or the same, see Figure 2a and Figure 2b, respectively.

Let us first start with "different type" configurations in Figure 2a. Configurations 1 and 2 have no additional extrema and in both of them the symmetric phase is stable. The difference is that in configuration 1 the total spin of the chain is aligned along the positive direction of the z-axis, and in configuration 2 – along the negative direction. Remarkably, configuration 1 is unstable for the bare LMG model. Configuration 3 is not realized and in configuration 4 both symmetric and broken symmetry extrema are minima, meaning that one of the phases is stable and the other is metastable. This means that coupling to the external spin can change the type of the phase transition between two phases from the second to the first one. The corresponding plots of the energy levels are presented in Figure 3.

Now we consider the "same type" configurations in Figure 2b. In configuration 1, two minima correspond to symmetric phases with the total spin aligned along the positive and negative directions of the z-axis. One of the phases is stable and the other is metastable, so a first order phase transition between them is possible. In configuration 2, the broken symmetry phase is stable, resembling the case of the bare LMG model. The configuration 3 is again not realized. The most interesting one is the configuration 4 in which the minima, corresponding to the stable broken symmetry phase, split into two. The plots of the energy levels, corresponding to described extrema configurations, can be found in Figure 4.

We also derive the conditions for stability of the points $\theta = 0, \pi, 2\pi$. Calculating the second derivatives we find:

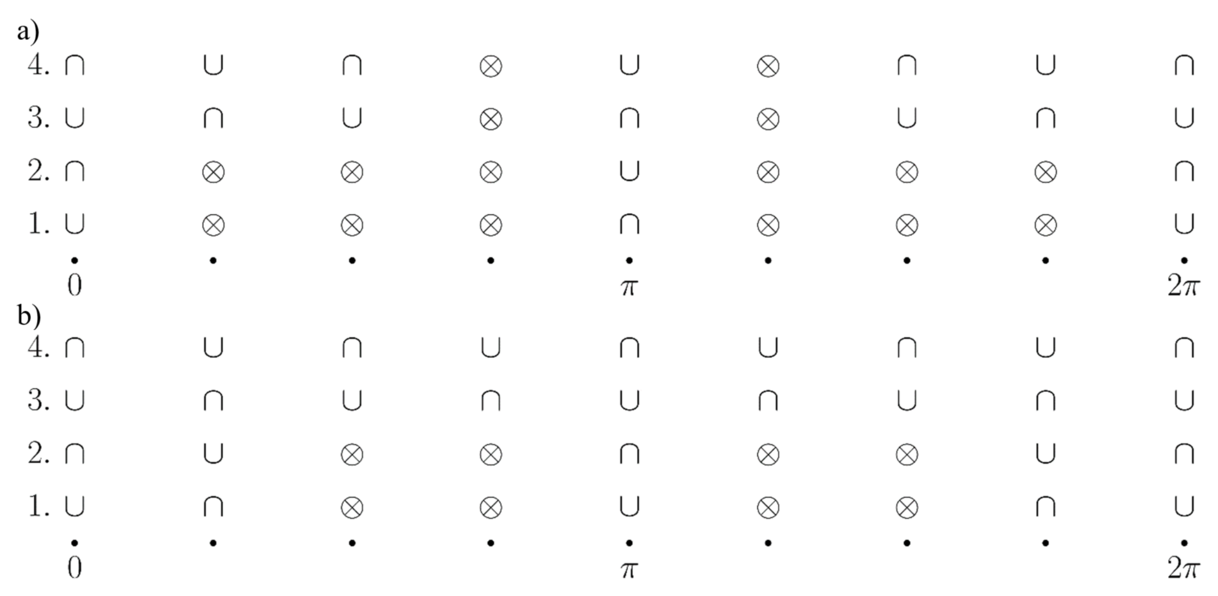

a)

4.	∩	∪	∩	⊗	∪	⊗	∩	∪	∩
3.	∪	∩	∪	⊗	∩	⊗	∪	∩	∪
2.	∩	⊗	⊗	⊗	∪	⊗	⊗	⊗	∩
1.	∪	⊗	⊗	⊗	∩	⊗	⊗	⊗	∪
	0				π				2π

b)

4.	∩	∪	∩	∪	∩	∪	∩	∪	∩
3.	∪	∩	∪	∩	∪	∩	∪	∩	∪
2.	∩	∪	⊗	⊗	∩	⊗	⊗	∪	∩
1.	∪	∩	⊗	⊗	∪	⊗	⊗	∩	∪
	0				π				2π

Figure 2: Possible configurations of the extrema of the ground state energy $E^{-}(\theta,\varphi)$. The symbol ∪ denotes a minimum, ∩ – a maximum, and ⊗ – absence of the extremum. In (a) "different type" configurations are presented and in (b) "same type" configurations are presented.

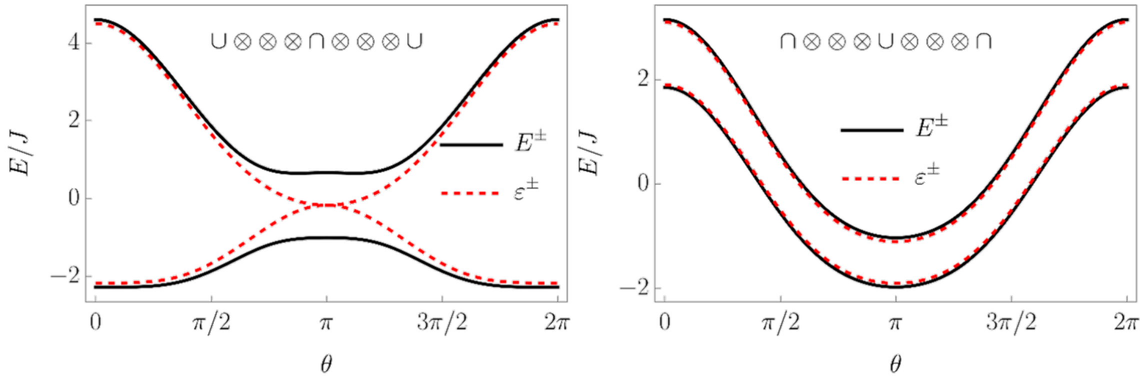

a) Configuration 1 from Figure 2a. b) Configuration 2 from Figure 2a.

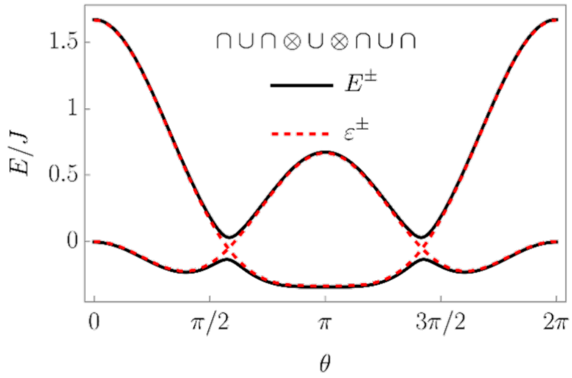

c) Configuration 4 from Figure 2a.

Figure 3: The energy levels of the system corresponding to configurations 1, 2, and 4 from Figure 2a. In plots a) and b) the symmetric phases with spin aligned along positive and negative directions of the *z*-axis, respectively, are stable. In plot c) one can observe a stable symmetric phase and a metastable broken symmetry phase.

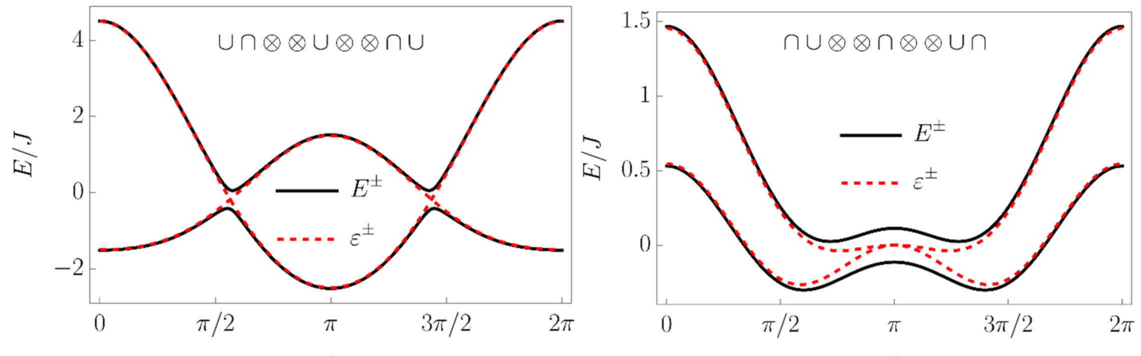

a) Configuration 1 from Figure 2b.

b) Configuration 2 from Figure 2b.

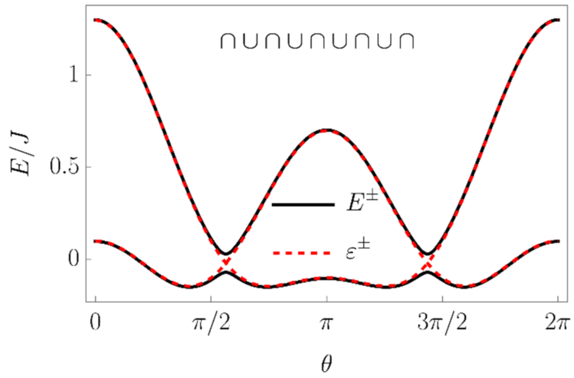

c) Configuration 4 from Figure 2b.

Figure 4: The energy levels of the system corresponding to configurations 1, 2, and 4 from Figure 2b. In plot a) the symmetric phases with spin aligned along negative direction of the *z*-axis is stable and the one with spin aligned along the positive direction is metastable. In plot c) the minima corresponding to the stable broken symmetry phase are split into two.

$$\frac{\partial^2}{\partial\theta^2}E^-\Big|_{\theta=\pi} = \tilde{\omega} - J + \frac{\tilde{J}\left(\tilde{J}-\omega\right)}{2\sqrt{\left(\tilde{J}-\omega\right)^2+\Delta^2}}$$
$$\frac{\partial^2}{\partial\theta^2}E^-\Big|_{\theta=0,2\pi} = -\tilde{\omega} - J + \frac{\tilde{J}\left(\tilde{J}+\omega\right)}{2\sqrt{\left(\tilde{J}+\omega\right)^2+\Delta^2}}. \tag{22}$$

Accordingly, the point $\theta = \pi$ is a minimum if

$$\tilde{\omega} > J - \frac{\tilde{J}\left(\tilde{J}-\omega\right)}{2\sqrt{\left(\tilde{J}-\omega\right)^2+\Delta^2}} \tag{23}$$

and points $\theta = 0, 2\pi$ are stable if

$$\tilde{\omega} < -J + \frac{\tilde{J}\left(\tilde{J}+\omega\right)}{2\sqrt{\left(\tilde{J}+\omega\right)^2+\Delta^2}}. \tag{24}$$

Two important observations can be made here. First, the right-hand side of Equation 23 can be negative for large enough values of $\tilde{J}$ (i.e., single spin–chain coupling) making the symmetric state always stable. Second, at certain range of parameters, both conditions (Equation 23) and Equation 24 might be true or not true simultaneously, which leads to the appearance of the “same type” configurations. More detailed analysis of transitions between different phases requires knowing the conditions of existence of intermediate extrema at $\theta = 0, \pi, 2\pi$. This boils down to finding all solutions of Equation 21 and one has to resort to numerical calculations. In Figure 5, the phase diagram, obtained numerically, is presented on the J–$\tilde{J}$ plane for fixed values of the rest of the parameters.

Results and Discussion

We have theoretically studied the infinitely coordinated Ising chain, coupled to a single external spin. We have written down the effective Hamiltonian in the Ising chain space by diagonalizing the Hamiltonian of the whole system in the space of the external spin. In the thermodynamic limit, when the chain Hamiltonian is exactly solvable, the energy spectrum of the

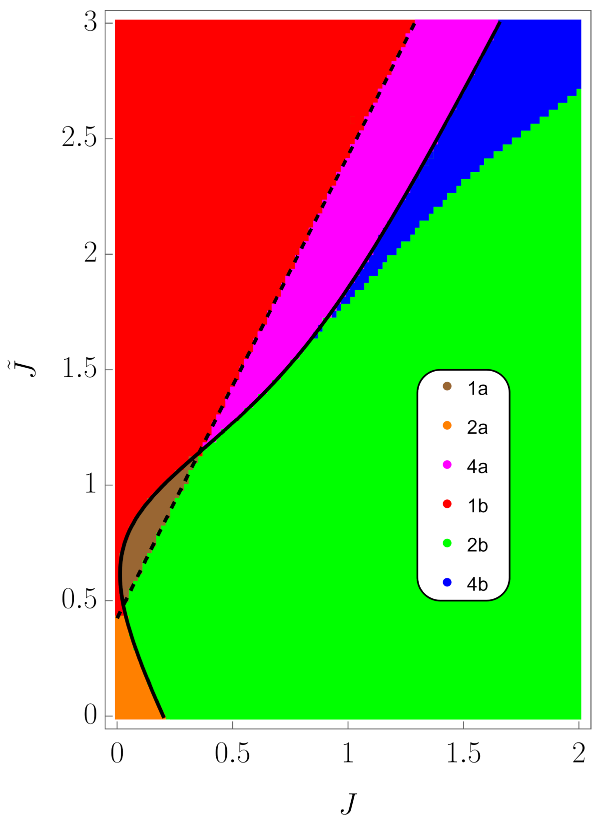

Figure 5: The phase diagram of the considered model on the J–$\tilde{J}$ plane. The legend notation coincides with the configurations in Figure 2 (e.g., 1a is the configuration 1 in Figure 2a). The black solid line is the contour given by Equation 23, and the dashed black line is given by Equation 24. The rest of the parameters are chosen as $\omega = 1$, $\tilde{\omega} = 0.2$, $\Delta = 0.5$, and $\tilde{\Delta} = 0$.

system was found. It is demonstrated that coupling to an external spin drastically changes the properties of the phases relative to the bare LMG model. In particular, it leads to the appearance of a new stable phase-symmetric one, but with the total spin of the chain oriented in the reverse direction compared to the symmetric state of the bare LMG model. This phase might be stable as well as metastable, and the first order phase transition between two stable phases is possible. The broken symmetry phase might also become metastable at certain values of the parameters, which means that the corresponding phase transition becomes of first order as opposed to the second order in the case of the bare LMG model. Finally, coupling to the external spin might change the properties of the broken symmetry phase by splitting the corresponding minima of energy into two.

In case of an experimental attempt, it is possible to check the spin configuration of the coordinated Ising chain by using a well-developed and very sensitive method of polarized neutron reflectometry (PNR) [23-26] to improve the qubit quality, which is an important task [27,28].

The considered model is relevant in the field of quantum computation, as the layout is used for a certain realization of the CCZ gate [10]. Although, admittedly, the thermodynamic limit approximation made during the analysis is far from a feasible experimental setup involving only several qubits.

Funding

The publication was prepared with the support of the Russian Science Foundation (Grant No. 23–72–01067).

Author Contributions

Seidali Seidov: data curation; investigation; software. Natalia Pugach: conceptualization; formal analysis; funding acquisition; validation; writing – original draft. Anatolie Sidorenko: data curation; investigation; supervision; validation.

ORCID® iDs

Seidali Seidov - https://orcid.org/0000-0003-1946-6014
Natalia Pugach - https://orcid.org/0000-0003-4017-1667
Anatolie Sidorenko - https://orcid.org/0000-0001-7433-4140

Data Availability Statement

All data that supports the findings of this study is available in the published article and/or the supporting information of this article.

Preprint

A non-peer-reviewed version of this article has been previously published as a preprint: https://arxiv.org/abs/2504.02164

References

1. Prokof'ev, N. V.; Stamp, P. C. E. *Rep. Prog. Phys.* **2000,** *63,* 669–726. doi:10.1088/0034-4885/63/4/204
2. Arenz, C.; Gualdi, G.; Burgarth, D. *New J. Phys.* **2014,** *16,* 065023. doi:10.1088/1367-2630/16/6/065023
3. Krovi, H.; Oreshkov, O.; Ryazanov, M.; Lidar, D. A. *Phys. Rev. A* **2007,** *76,* 052117. doi:10.1103/physreva.76.052117
4. Budini, A. A. *Phys. Rev. A* **2019,** *99,* 052125. doi:10.1103/physreva.99.052125
5. Han, L.; Zou, J.; Li, H.; Shao, B. *Entropy* **2020,** *22,* 895. doi:10.3390/e22080895
6. Brenes, M.; Min, B.; Anto-Sztrikacs, N.; Bar-Gill, N.; Segal, D. *J. Chem. Phys.* **2024,** *160,* 244106. doi:10.1063/5.0207028
7. Cattaneo, M.; Giorgi, G. L.; Maniscalco, S.; Zambrini, R. *New J. Phys.* **2019,** *21,* 113045. doi:10.1088/1367-2630/ab54ac
8. Mitchison, M. T.; Plenio, M. B. *New J. Phys.* **2018,** *20,* 033005. doi:10.1088/1367-2630/aa9f70
9. Czerwinski, A. *Symmetry* **2022,** *14,* 1752. doi:10.3390/sym14081752
10. Simakov, I. A.; Mazhorin, G. S.; Moskalenko, I. N.; Seidov, S. S.; Besedin, I. S. *Phys. Rev. Appl.* **2024,** *21,* 044035. doi:10.1103/physrevapplied.21.044035

11. Lipkin, H. J.; Meshkov, N.; Glick, A. J. *Nucl. Phys.* **1965,** *62,* 188–198. doi:10.1016/0029-5582(65)90862-x
12. Ribeiro, P.; Vidal, J.; Mosseri, R. *Phys. Rev. E* **2008,** *78,* 021106. doi:10.1103/physreve.78.021106
13. Chinni, K.; Poggi, P. M.; Deutsch, I. H. *Phys. Rev. Res.* **2021,** *3,* 033145. doi:10.1103/physrevresearch.3.033145
14. Santos, L. F.; Távora, M.; Pérez-Bernal, F. *Phys. Rev. A* **2016,** *94,* 012113. doi:10.1103/physreva.94.012113
15. Vidal, J. *Phys. Rev. A* **2006,** *73,* 062318. doi:10.1103/physreva.73.062318
16. Moroz, A. *EPL* **2016,** *113,* 50004. doi:10.1209/0295-5075/113/50004
17. Eckle, H.-P.; Johannesson, H. *J. Phys. A: Math. Theor.* **2017,** *50,* 294004. doi:10.1088/1751-8121/aa785a
18. Li, Z.-M.; Batchelor, M. T. *Phys. Rev. A* **2021,** *104,* 033712. doi:10.1103/physreva.104.033712
19. Naseri, A.; Hu, Y.; Luo, W. *arXiv* **2020,** 2012.00197. doi:10.48550/arxiv.2012.00197
20. Botet, R.; Jullien, R.; Pfeuty, P. *Phys. Rev. Lett.* **1982,** *49,* 478–481. doi:10.1103/physrevlett.49.478
21. Botet, R.; Jullien, R. *Phys. Rev. B* **1983,** *28,* 3955–3967. doi:10.1103/physrevb.28.3955
22. Castaños, O.; López-Peña, R.; Hirsch, J. G.; López-Moreno, E. *Phys. Rev. B* **2006,** *74,* 104118. doi:10.1103/physrevb.74.104118
23. Khaydukov, Y. N.; Lenk, D.; Zdravkov, V.; Morari, R.; Keller, T.; Sidorenko, A. S.; Tagirov, L. R.; Tidecks, R.; Horn, S.; Keimer, B. *Phys. Rev. B* **2021,** *104,* 174445. doi:10.1103/physrevb.104.174445
24. Khaydukov, Y.; Pütter, S.; Guasco, L.; Morari, R.; Kim, G.; Keller, T.; Sidorenko, A.; Keimer, B. *Beilstein J. Nanotechnol.* **2020,** *11,* 1254–1263. doi:10.3762/bjnano.11.109
25. Khaydukov, Y.; Kravtsov, E.; Morari, R.; Lenk, D.; Mustafa, L.; Kim, G.; Trapp, M.; Zhaketov, V.; Proglyado, V.; Zrdavkov, V.; Nikitenko, Y.; Krug von Nidda, H.-A.; Keller, T.; Steitz, R.; Tideks, R.; Sidorenko, A.; Ustinov, V.; Aksenov, V.; Keimer, B. *J. Phys.: Conf. Ser.* **2019,** *1389,* 012060. doi:10.1088/1742-6596/1389/1/012060
26. Zhaketov, V. D.; Devyaterikov, D. I.; Avdeev, M. M.; Norov, D. A.; Kolupaev, E. D.; Kuzmenko, M. O.; Pugach, N. G.; Khaydukov, Yu. N.; Kravtsov, E. A.; Nikitenko, Yu. V.; Aksenov, V. L. *Phys. Solid State* **2023,** *65,* 1076. doi:10.61011/pss.2023.07.56393.35h
27. Klenov, N.; Kornev, V.; Vedyayev, A.; Ryzhanova, N.; Pugach, N.; Rumyantseva, T. *J. Phys.: Conf. Ser.* **2008,** *97,* 012037. doi:10.1088/1742-6596/97/1/012037
28. Klenov, N. V.; Kornev, V. K.; Sharafiev, A. V.; Bakurskiy, S. V.; Pugach, N. G. *J. Phys.: Conf. Ser.* **2010,** *234,* 042017. doi:10.1088/1742-6596/234/4/042017

License and Terms

The definitive version of this article is the electronic one which can be found at:
https://doi.org/10.3762/bjnano.16.117

BEILSTEIN JOURNAL OF NANOTECHNOLOGY

Programmable soliton dynamics in all-Josephson-junction logic cells and networks

Vsevolod I. Ruzhickiy[1,2], Anastasia A. Maksimovskaya*[1,2,3], Sergey V. Bakurskiy[1,4], Andrey E. Schegolev[1,5], Maxim V. Tereshonok[5], Mikhail Yu. Kupriyanov[1,4], Nikolay V. Klenov[3] and Igor I. Soloviev[1,2,4]

Full Research Paper

Open Access

Address:
[1]Lomonosov Moscow State University, Skobeltsyn Institute of Nuclear Physics, Moscow, 119991, Russia, [2]All-Russian Research Institute of Automatics n.a. N.L. Dukhov (VNIIA), 127030, Moscow, Russia, [3]Lomonosov Moscow State University, Faculty of Physics, Moscow, 119991, Russia, [4]Moscow Institute of Physics and Technology, 141700 Dolgoprudny, Russia and [5]Moscow Technical University of Communications and Informatics (MTUCI), 111024, Moscow, Russia

Email:
Anastasia A. Maksimovskaya* - stasyahime@gmail.com

* Corresponding author

Keywords:
Josephson-based diode; kinetic inductance; soliton dynamics; superconducting electronics; superconducting neural networks

Beilstein J. Nanotechnol. **2025,** *16,* 1883–1893.
https://doi.org/10.3762/bjnano.16.131

Received: 31 July 2025
Accepted: 30 September 2025
Published: 28 October 2025

This article is part of the thematic issue "Superconducting artificial neural networks and quantum circuits".

Guest Editor: A. S. Sidorenko

Abstract

We demonstrate the programmable control of kinetic soliton dynamics in all-Josephson-junction (all-JJ) networks through a novel tunable cell design. This cell enables on-demand switching of transmission lines and operates across defined parameter regimes supporting diverse dynamical modes. By introducing a structural asymmetry into a transmission line, we implement a Josephson diode that enforces unidirectional soliton propagation. The programmability of the kinetic inductance then provides a crucial mechanism to selectively enable or disable this diode functionality. By engineering artificial inhomogeneity into the circuit architecture, we enhance robustness in all-JJ logic circuits, 2D transmission line all-JJ lattices, and neuromorphic computing systems.

Introduction

The rapid advancement of Josephson junction (JJ) logic circuits [1-5] and neuromorphic networks [6-9] holds transformative potential for ultra-low-power computing. However, achieving scalable integration remains a critical bottleneck, as conventional JJ-based architectures face fundamental density constraints imposed by magnetic flux manipulation requirements and complex mutual inductive crosstalks.

Circuits composed entirely of Josephson junctions (all-JJ circuits) [10-16] represent a promising platform for energy-efficient, high-speed, and scalable computing. In these systems, the propagation of information is associated with the movement of a current wave/topological soliton, which is clearly visible in the model by a 2π jump of the so-called Josephson phase, φ. In contrast to conventional rapid single flux quantum (RSFQ) logic, the phase drop for the considered single kinetic soliton (SKS) occurs not on the relatively large connecting geometric inductors, but on the Josephson junctions. SKS is a propagating wave of phase change with kinetic energy limited from below; the corresponding current pulse “dissipates” if its motion is interrupted, for example, by a structural inhomogeneity in a transmission line. Traditionally, this sensitivity to structural inhomogeneities has been viewed as a challenge for robust circuit design.

In this work, we propose to exploit the sensitivity mentioned above. We base our proposal on the concept of applying a small number of key cells, which should create precisely engineered tunable inhomogeneities. Such inhomogeneity may be designed as an element of tunable kinetic inductance [17]. This element has high inductance at small scales and can be controlled using currents [18,19], voltage [20], or magnetic fields [21,22]. At the same time, the use of hybrid superconductor–normal metal structures makes it possible to increase the effect of frequency tuning [23,24], while the addition of ferromagnetic layers permits the non-volatile control [25,26]. Another feature of tunable kinetic inductance element is the linear behavior for weak signals, which excludes formation of parasitic processes in the transmission line. This permits to apply tunable kinetic inductance in the resonators with shifting resonance frequency [19,21,22], as well as in sensitive all-JJ digital circuits.

This idea enables us to use the “flaws” of the structure as its important features, opening up a pathway to creating programmable and reconfigurable large circuits. An obvious and widely required application of this technology is in the development of superconductive programmable gate arrays (SPGAs) [27-30], an active area of current research. Another important application of this idea lies in the promising neuromorphic direction [31-33]. Earlier in [34], we have already proposed using kinetic inductances to control neuron dynamics in networks based on radial basis functions (RBF-networks). Moreover, this approach can be extended to hardware realizations of bio-inspired spiking neural networks [35-42] by solving the challenges of creating controllable synapses to realize the effect of spike-timing-dependent plasticity and unidirectional feedbacks for self-regulation. Furthermore, the physical resemblance between solitons and the action potentials (spikes of voltage) generated in biological nervous systems makes all-JJ structures tempting candidates for constructing neuromorphic hardware [43].

In this paper, we investigate the use of controlled kinetic inductance to create an engineered inhomogeneous medium for kinetic solitons. We demonstrate that by tuning this inhomogeneity, distinct dynamical modes can be induced, fundamentally altering the soliton’s behavior. Furthermore, we explore how structural asymmetry within this medium can be exploited to achieve a diode effect, enabling non-reciprocal soliton propagation. Building upon these foundational concepts, we then propose two specific architectural solutions: a programmable switch and a versatile routing matrix, which we term the “WayMatrix”. We suggest that these architectures provide a framework for the flexible configuration of advanced logic and neuromorphic circuits.

Results

Model description

To model the dynamics of kinetic solitons [43], we employ the resistively and capacitively shunted junction (RCSJ) model [1], where the total current I across a Josephson junction is the sum of the supercurrent, the quasi-particle current, and the displacement current:

$$I = I_c \sin(\varphi) + \frac{V}{R_N} + C\frac{dV}{dt}. \qquad (1)$$

Here, φ is the phase difference for the complex superconducting order parameter across the junction, V is the voltage, I_c is the critical current, R_N is the resistance in the normal state and C is the capacitance. For analysis, it is convenient to express this equation in a dimensionless form. We normalize the time to the inverse of a reference plasma frequency, $\tau = \tilde{\omega}_p t$, where $\tilde{\omega}_p = \sqrt{2\pi \tilde{I}_c / (\Phi_0 C)}$, and normalize the current to a reference critical current $\tilde{I}_c$. This yields:

$$i = A \cdot \sin(\varphi) + \alpha\dot{\varphi} + \ddot{\varphi}. \qquad (2)$$

In this normalized equation, the dots above the phases indicate differentiation over time with respect to τ. The dimensionless damping coefficient is $\alpha = \Phi_0 \tilde{\omega}_p / (2\pi \tilde{I}_c R_N)$. The term $\dot{\varphi}$ represents the voltage normalized by the characteristic voltage $V_0 = \Phi_0 \tilde{\omega} / (2\pi)$. The parameter $A = I_c / \tilde{I}_c$ is the normalized amplitude of the critical current for junctions with the critical current I_c that differs from the reference normalization value $\tilde{I}_c$.

To analyze the circuit dynamics, we adopt a nodal analysis approach. In this approach, the gauge-invariant phase difference across any element is expressed in terms of the nodal phases at its terminals, $\varphi = \varphi_k - \varphi_j$. The phase of the ground node is set to zero by convention. This formulation inherently satisfies Kirchhoff’s current law (KCL) at each node. For any node k connected to H elements, KCL dictates that the algebraic sum of currents is zero:

$$\sum_{h=1}^{H} I_{k,j(h)} = 0, \tag{3}$$

where the index h runs over all elements connected to node k, $j(h)$ is the index of the node at the other end of element h, and $I_{k,j(h)}$ is the normalized current flowing from the node k to the node $j(h)$. Each current is described by the RCSJ model (Equation 2):

$$\frac{I_{k,j(h)}}{\tilde{I}_\mathrm{c}} = A_h \sin\left(\varphi_k - \varphi_{j(h)}\right) + \alpha_h\left(\dot{\varphi}_k - \dot{\varphi}_{j(h)}\right) + \left(\ddot{\varphi}_k - \ddot{\varphi}_{j(h)}\right). \tag{4}$$

With this approach, the current across the inductance is defined by the expression

$$\frac{I^{L}_{k,j(h)}}{\tilde{I}_\mathrm{c}} = \frac{\Phi_0}{2\pi L \tilde{I}_\mathrm{c}}\left(\varphi_k - \varphi_{j(h)}\right) = \frac{\left(\varphi_k - \varphi_{j(h)}\right)}{l}, \tag{5}$$

where $l = L/L_\mathrm{J}$ is inductance normalized to the Josephson inductance $L_\mathrm{J} = \Phi_0 / \left(2\pi \tilde{I}_\mathrm{c}\right)$.

After substituting the expressions for the current into the formula for the current balance at the node, we get:

$$M_{k,k}\ddot{\varphi}_k - \sum_{h=1}^{H} M_{k,j(h)}\ddot{\varphi}_{k,j(h)} = F_k\left(\varphi_k, \varphi_{k,j(h)}, \dot{\varphi}_k, \dot{\varphi}_{k,j(h)}\right), \tag{6}$$

where $M_{k,k}$ is the sum of the coefficients before $\ddot{\varphi}_k$, $M_{k,j(h)}$ are the coefficients before $\ddot{\varphi}_{k,j(h)}$, F_k contains the sum of all summands except those that do not contain the second derivative. In F_k, all summands with φ_k are written with a minus sign, and all summands with $\varphi_{k,j(h)}$ are written with a plus sign. Additional currents (e.g., the bias current or the time-dependent current from the generator) are also included as components. After writing down Equation 6 for each node, a system of second-order diffeomorphic equations are obtained, which can be represented in matrix form:

$$\hat{M}\ddot{\varphi} = \begin{pmatrix} M_{11} & M_{12} & \cdots & M_{1N} \\ M_{21} & M_{22} & \cdots & M_{2N} \\ \vdots & \vdots & \ddots & \vdots \\ M_{N1} & M_{N2} & \cdots & M_{NN} \end{pmatrix} \begin{pmatrix} \ddot{\varphi}_1 \\ \ddot{\varphi}_2 \\ \vdots \\ \ddot{\varphi}_N \end{pmatrix} = \mathbf{F}(\varphi, \dot{\varphi}). \tag{7}$$

The resulting system of N ordinary differential equations is expressed in the matrix form shown in Equation 7. In this equation, $\vec{\varphi}$ is the vector of nodal phases, N is the total number of non-ground nodes, and $\hat{M}$ is the $N \times N$ mass matrix (also known as the capacitance matrix), which is defined by the capacitive coupling coefficients from Equation 6. A key property of $\hat{M}$ is its sparsity, which arises directly from the local connectivity of the circuit topology; each node is connected to a small subset of other nodes. To increase computational efficiency, we exploit this sparsity when solving the system. The equations are integrated numerically using an adaptive-step-size solver based on the explicit Runge–Kutta (4th and 5th order) formula, commonly known as the Dormand–Prince pair [44,45], which is well suited for this class of non-stiff problems.

The fundamental building block of our design is the "kinetic inductance controllable key" (KICK), which is constructed from the two modified unit cells of an all-Josephson Junction Transmission Line (all-JJTL). As depicted in Figure 1a, each cell is modified by incorporating a controlled kinetic inductance in series with one of its Josephson junctions connected to the ground plane. There are some operational regimes inherent to such a KICK governed by the value of this inductance and by the damping parameter of junctions within the transmission line. The damping parameter is a critical factor as it dictates the kinetic soliton's propagation rate.

As a preliminary step, we characterized the dependence of the kinetic soliton propagation velocity on the damping parameter of the connecting junctions, α (see Figure 1b). We define the velocity as the number of grounded junctions traversed per unit of normalized time, τ. Our simulations revealed a critical damping threshold at $\alpha_\mathrm{crit} \approx 0.8$; below this value, stable soliton propagation is not supported. Also, under this condition, the energy dissipation rate is too high relative to the energy transfer between adjacent junctions, causing the soliton to decay. When $\alpha > \alpha_\mathrm{crit}$, the soliton velocity is a monotonically increasing function of the damping. This dependence falls into an approximately linear regime for $\alpha > 3$. The physical mechanism for this velocity increase can be understood from the RCSJ model; a higher value of α enhances the resistive quasiparticle current ($\alpha\dot{\varphi}$) that flows as a junction switches. This larger current provides a stronger driving force to the next junction in the line, causing it to reach its critical threshold and switch more rapidly, thus increasing the overall propagation velocity of the soliton.

The functionality of the KICK is determined by the interplay between the damping α and the normalized kinetic inductance L/L_J. Figure 1c summarizes the behavior of the device in a parameter map, which reveals four distinct operational regimes: (1) Open mode: The KICK is effectively transparent, allowing an incident kinetic soliton to propagate through it with minimal perturbation. (2) Close mode: The KICK acts as a terminator, blocking and destroying the incoming soliton. (3) T-mode: The

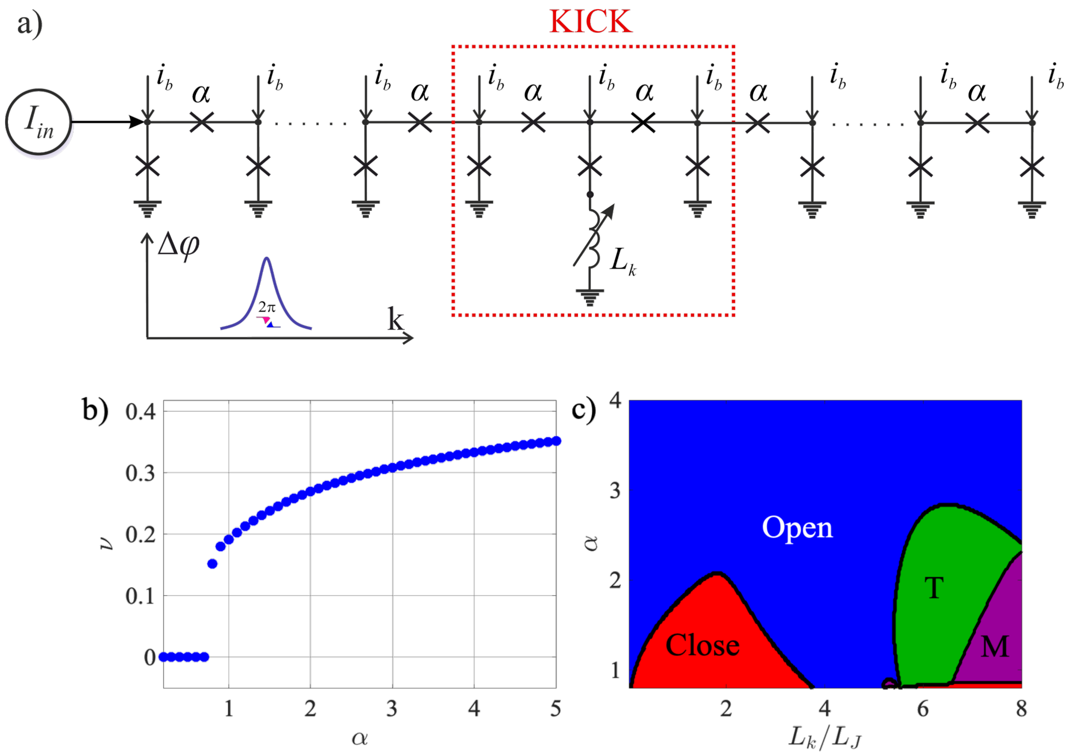

Figure 1: (a) An equivalent scheme for the “kinetic inductance controllable key” (KICK) as a part of an all-Josephson transmission line. A soliton whose dynamics is controlled by the developed key is represented schematically. (b) Dependence of the single kinetic soliton (SKS) propagation velocity, measured in Josephson junctions per normalized time unit, on the damping parameter α. (c) Map of different modes depending on the damping parameter and kinetic inductance measurement. Close mode (red zone): The KICK does not allow the SKS to pass through. Open mode (blue zone): The SKS passes through the KICK. T-mode (green zone): The KICK has two stable states, and every second SKS passes through it. M-mode (purple zone): The KICK has many stable states.

KICK functions as a T-flip-flop. It possesses two stable states, and each arriving soliton toggles the cell from its current state to the other. Every second soliton passes to the exit. (4) M-mode (Multistate mode): This regime is characterized by the formation of more than two stable states and other complex dynamics, which fall outside the scope of this study.

An essential feature of the KICK is the ability to switch between different modes at a fixed value of α; thus, by fixing α (e.g., $\alpha = 2$) and varying the kinetic inductance, we can switch between all modes (Open mode → Close mode → Open mode → T-mode → M-mode) represented on the parameter map (see Figure 1).

To illustrate the operational modes of the KICK, we simulated the propagation of a kinetic soliton through the all-JJTL. The simulated line comprises 31 grounded junctions with a uniform damping parameter of connecting junctions $\alpha = 1$. The KICK is implemented by inserting a controlled kinetic inductance in series with the ground junction at the line’s center (node $k = 16$). Figure 2 presents the results for different values of this inductance, corresponding to distinct operational modes. Each panel displays two key physical quantities on dual y-axes: (1) the spatial profile of the nodal Josephson phases (φ_k) as a function of the node index k and (2) the normalized currents flowing through the series junctions connecting the nodes. The current between nodes k and $k + 1$ ($I_c/\tilde{I}_c \sin(\varphi_{k+1} - \varphi_k)$) is plotted at the midpoint index $k + 0.5$ for visual clarity.This visualization allows for a direct comparison of the system’s state before and after soliton interaction. The solid lines depict the initial state (before the soliton reaches the KICK), and the dashed lines show the final state (after the soliton has passed and the system has settled).

For a low inductance of $L/L_J = 0.1$ (see Figure 2a), corresponding to the Open mode, the KICK causes only slight disturbance in the transmission line.The incident soliton propagates through it unimpeded, and the entire line returns to its initial physical state. However, increasing the inductance to $L/L_J = 2$ (see Figure 2b) switches the system to the Close mode. In this mode, the KICK serve as a significant barrier; when the soliton arrives, the large inductance impedes the necessary current dynamics, halting the propagation and causing the soliton to be annihilated. Consequently, the 2π phase slip, which signifies the

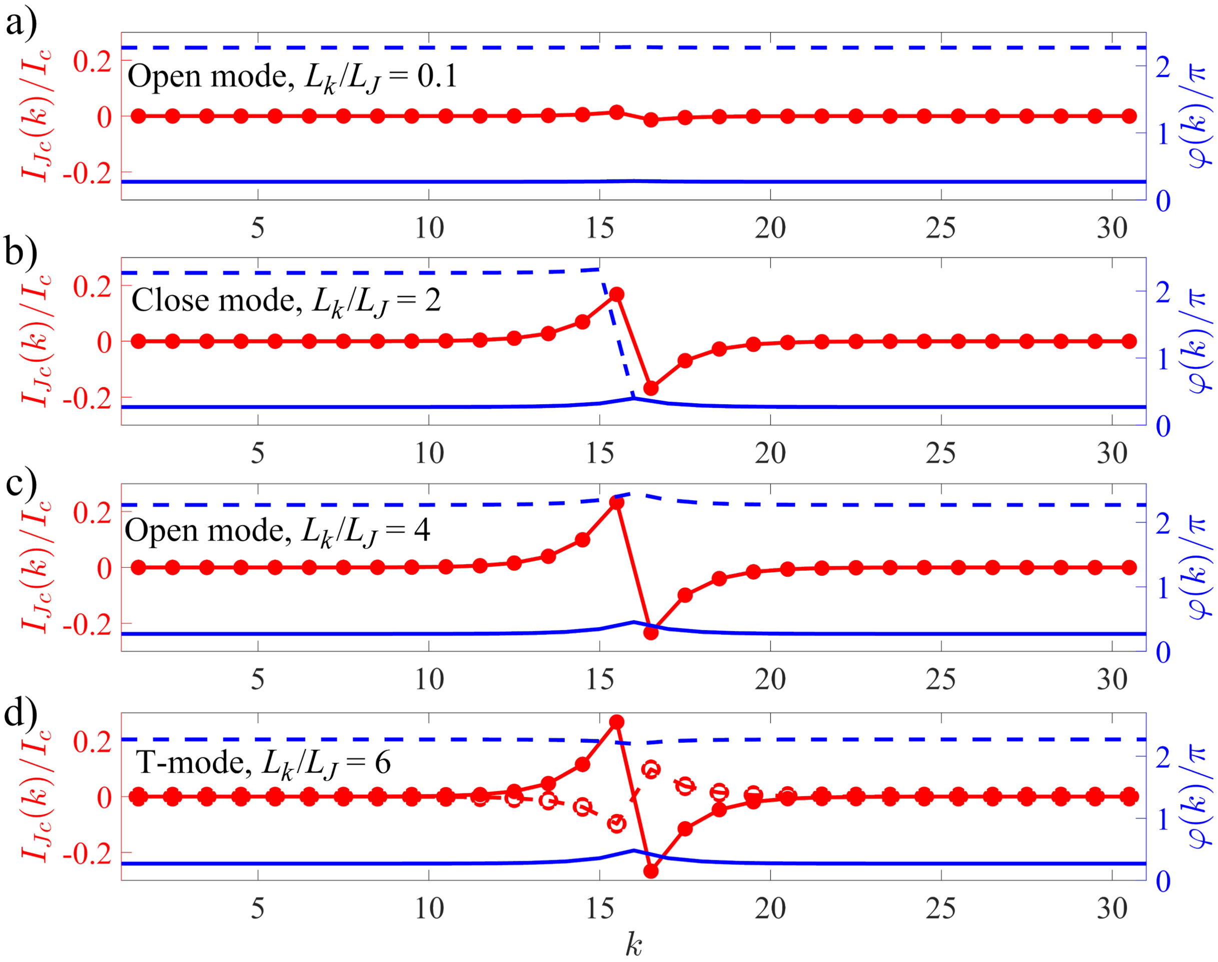

Figure 2: Spatial distributions of the Josephson phase (blue curves) and current (red curves) in (a, c) Open mode, $L_k/L_J = 0.1$ (a) and $L_k/L_J = 4$ (c); (b) Close mode, $L_k/L_J = 2$; and (d) T-mode, $L_k/L_J = 6$. Solid lines show initial profiles, and dashed lines represent distributions after soliton passage. The Josephson phase is plotted against the integer node index k, whereas the current is plotted at the midpoint index $k + 0.5$ to represent the junction between nodes k and $k + 1$, see Figure 1a.

soliton’s passage, only traverses the first half of the line (nodes 1 to 15), while the segment beyond the KICK remains entirely unperturbed. Remarkably, a further increase of inductance to $L/L_J = 4$ (see Figure 2c) leads to the re-emergence of the Open mode. This non-trivial effect is governed by transient energy storage in the inductor L. Although the soliton is momentarily halted at the KICK, the subsequent release of stored magnetic energy provides the necessary “kick” to complete the phase slip at node 16. This re-initiates the propagation, allowing the soliton to effectively re-form and travel down the rest of the line. Similarly to the low-inductance case, the soliton successfully traverses the entire line, and the system returns to its initial physical state.

The behavior of the KICK in the T-Mode, which enables its use as a T-flip-flop, is detailed in Figure 2d. This mode is defined by the existence of two distinct stable states, physically corresponding to a bistable potential landscape created by the KICK architecture. These two states are distinguished by the presence of persistent, static currents of opposite polarity flowing from the central node ($k = 16$). This physical difference leads to an fundamentally state-dependent and asymmetric toggling action. When the KICK is in the first stable state, an incoming soliton successfully flips it to the second state and is transmitted, continuing its propagation down the line. Conversely, when starting from the second state, an arriving soliton again flips the KICK back to the first state, but it is annihilated in the process and does not propagate further. This state-dependent transmission and annihilation is the core mechanism that allows the KICK to function as a memory element or a dynamic routing switch.

Beyond primary operational modes, the system exhibits other notable behavior types in specific regions of its parameter space. The M-Mode, for instance, is characterized by complex responses, depend on previous events. This can include such behavior when an initial soliton is annihilated, effectively "priming" the cell to transmit all subsequent solitons, a feature potentially useful for tasks like sequential filtering. Furthermore, in the transition regions between the primary modes, we observe phenomena such as soliton reflection back towards the source.

Finally, the asymptotic behavior in the high-damping (α) limit is particularly significant. As α increases, so does the soliton's velocity and kinetic energy. Consequently, for sufficiently high α, the soliton's energy is large enough to overcome any potential barrier presented by the KICK, ensuring transmission regardless of the inductance value. This results in a universal Open mode at high rates. Crucially, this high-energy passage is not inert; if the KICK is in a bistable regime (such as the T-Mode), the "passing" soliton can still deliver enough of an impulse to toggle the cell's state.

The soliton diode

What is even more interesting is that the KICK architecture can be engineered to function as a soliton diode, a device the function of which is similar to that of a semiconductor diode, allowing the soliton to pass in only one direction. This is achieved by introducing a structural asymmetry into the cell's design. It is important to note that such non-reciprocal behavior can be achieved even without the kinetic inductance (L = 0). However, the inclusion of one (i.e., a tunable inductance) is a key innovation, as it allows to dynamically switch this directional property on and off.

We demonstrate this principle through simulation of a KICK with $L/L_J = 2$. In our model, the transmission line's series junctions have a nominal critical current of $I_c = 0.7\tilde{I}_c$. The asymmetry is created by increasing the critical current of the specific junction connecting nodes 15 and 16 to $I_c = \tilde{I}_c$ (i.e., to 1 in normalized units). The effect of this asymmetric potential barrier is that a soliton initiated in the forward direction (from node 1) successfully overcomes it and is transmitted along the entire line. In contrast, a soliton propagating in the reverse direction (from node 31) is unable to pass the barrier and is annihilated at node 17.

Figure 3 demonstrates the non-reciprocal behavior of the soliton diode by showing a sequence of five snapshots of the nodal Josephson phase distribution at successive moments in time, arranged from top to bottom. The process begins with the line in its initial state (top panel), after which a soliton is initiated from the left side (node 1). As shown in the second panel, this forward-propagating soliton successfully passes through the diode, resulting in a 2π phase advance across all nodes. Immediately after, a new soliton is initiated from the right side (node 31) to test the reverse direction. The third panel reveals that this soliton is blocked; its propagation is halted at the diode, and the corresponding 2π phase slip is confined to nodes 17 through 31. The fourth panel confirms the robustness of this blocking action, as a second, subsequent reverse-propagating soliton is also annihilated in the same manner. To complete the demonstration, another forward-propagating soliton is sent from the left. The fifth panel confirms that the diode once again allows it to pass, resulting in another full 2π phase advance across the entire line. It is crucial to note that although the absolute phase values accumulate in multiples of 2π throughout this sequence, the physical state of the structure remains unchanged after each full transmission, a direct consequence of the 2π periodicity of the Josephson energy.

A significant feature of this structure is the ability to disable the diode effect. By increasing the inductance to L/L_J = 3, the device becomes bi-directionally transparent, effectively turning the diode function "off". This demonstrates how the introduced structural asymmetry alters the operational landscape of the device: An inductance value that would normally correspond to the Close mode in a symmetric KICK now matches to a bi-directional Open mode for the asymmetric diode structure. Furthermore, it is worth noting that the asymmetry required for diode-like behavior can be achieved through alternative means, such as by creating a local mismatch in the damping parameter, for instance, by increasing α from 1 to 3 for one of the series junctions instead of the critical current.

The ability to enforce a specific direction of soliton flow makes the soliton diode an essential component for complex circuit design. This is particularly critical in architectures involving feedback loops, where it is necessary to unambiguously define the direction of signal propagation. This concept can be extended by cascading two such tunable diodes with opposing forward directions. This configuration creates a programmable transmission line where the permitted direction of soliton travel can be pre-configured by setting the inductance values of each diode.

Discussion

Implementation of reconfigurable networks

On the basis of the operational principles of the kinetic inductance controllable key and the soliton diode, we now demonstrate how these fundamental building blocks can be integrated to create reconfigurable soliton-based logic circuits. We begin by proposing a specific proof-of-concept design for a signal routing network and then introduce a generalized, scalable architecture suitable for complex computational tasks.

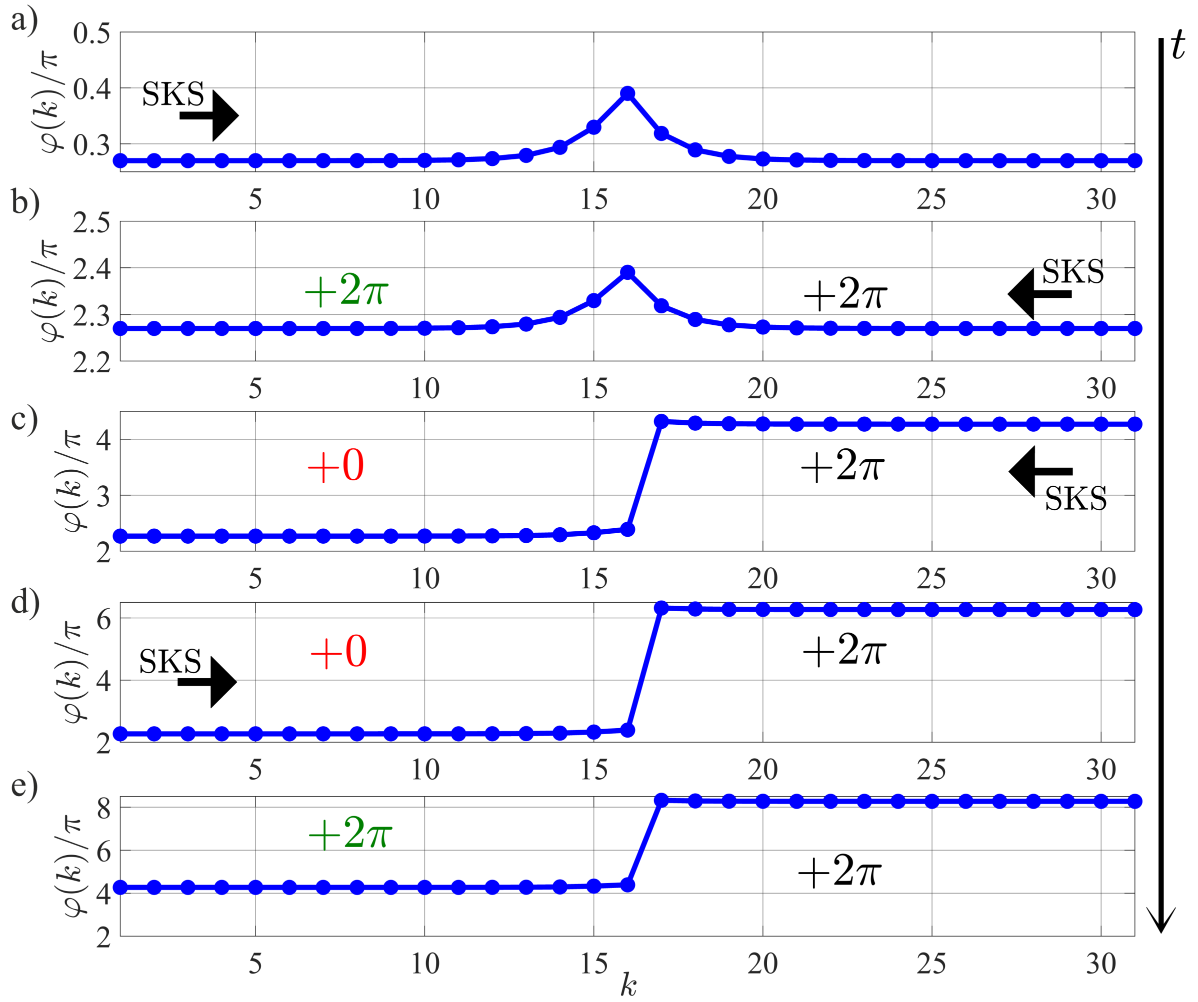

Figure 3: Temporal evolution of Josephson phase asymmetry in a soliton diode: (a) initial state; (b) after left-propagating soliton passage; (c, d) sequential right-propagating soliton interactions; (e) final left-propagating soliton recurrence.

As a direct application of the KICK's switching capabilities, we first propose the three-input, three-output routing network illustrated in Figure 4a. The proposed architecture is based on a grid where each path depicted is itself a complete all-JJTL. The routing mechanism would depend on the incorporation of KICKs into specific segments of these all-JJTLs. By programming each KICK to be in either its Open mode (transmitting) or Close mode (blocking), one could control the flow of solitons through the network and define a unique path from any input to any output. To prevent collisions between solitons traveling along different routes, the design incorporates auxiliary buffer lines. These lines make it possible to define a set of non-intersecting paths for all required connections, thus ensuring collision-free operation. This design serves to validate the fundamental principle of using KICKs as programmable switches.

With this idea, we propose a more general and powerful architecture, which we term the "WayMatrix", shown schematically in Figure 4b. This versatile $N \times M$ routing matrix is conceived as a core component of larger soliton-based processors. Its enhanced functionality would be predicated on the synergistic action of its core components. First, KICKs integrated into the line segments would act as programmable switches controlling the signal flow. Second, the directionality of soliton propagation would be rigorously enforced by integrated soliton diodes. Thus, the diodes and switches placed in the all-JJTL lines determine the direction of soliton propagation in the line. Finally, to solve the problem of collisions in a dense matrix, we propose dedicated vertical lines that enable row-skipping connections. For the same purposes, horizontal lines can also be used for column-skipping connections.

At first glance, it may seem that the proposed architecture is a complicated version of a memristive crossbar, but this is not the case. The main distinction is in the organization of interconnections between lines: In a memristive crossbar, as the name sug-

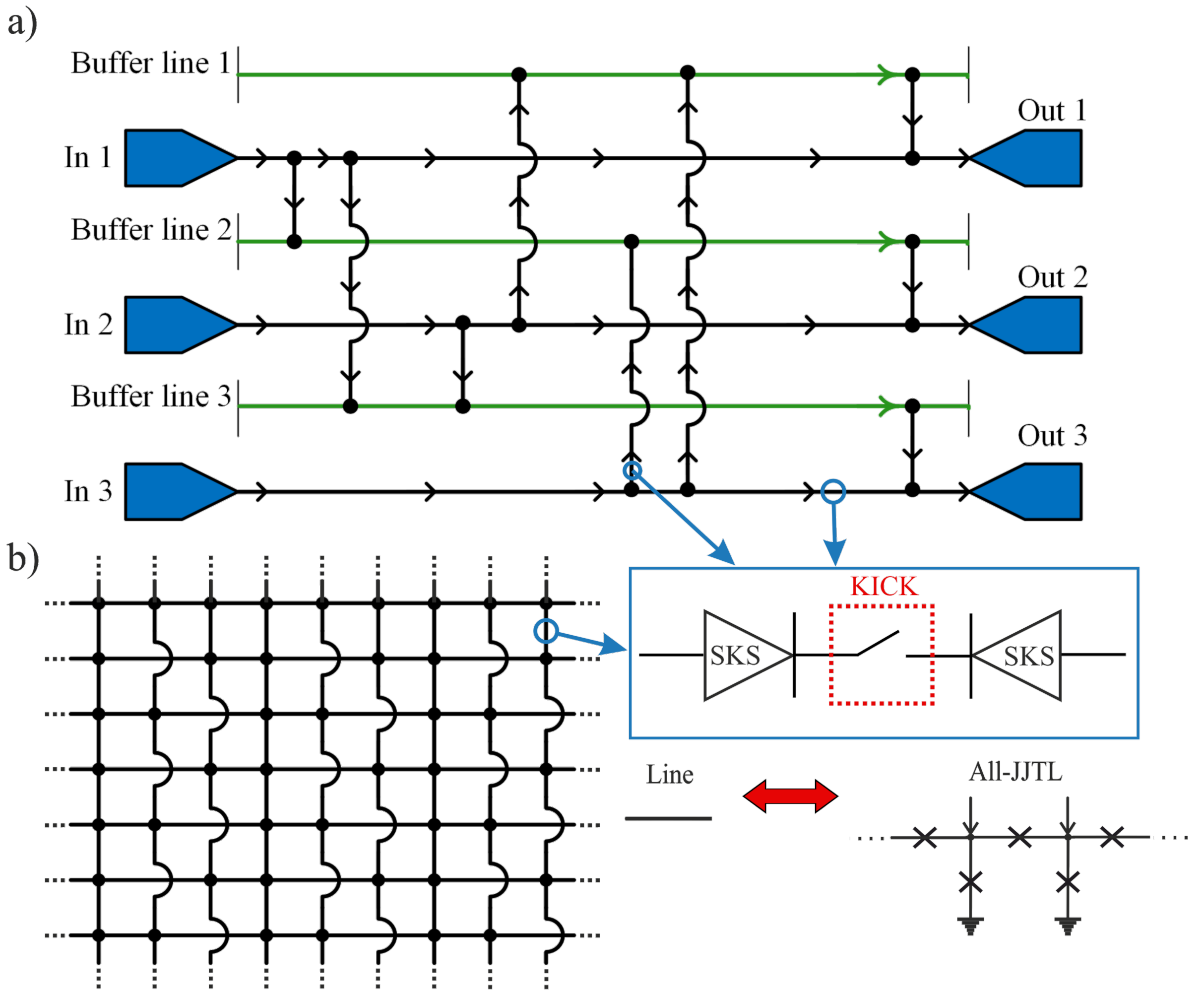

Figure 4: (a) Schematic of an all-Josephson-junction transmission line (all-JJTL) network with three inputs (In 1, In 2, In 3), three outputs (Out 1, Out 2, Out 3), and three auxiliary buffer lines. Black arrows on the lines indicate soliton propagation paths. Input–output connections are configured by setting operation modes of kinetic inductance controllable keys (KICKs), where each cell either transmits or blocks solitons based on its programmed state. (b) The schematic shows a transmission line matrix where path selection is governed by KICKs and signal directionality is ensured by soliton diodes. Specific vertical lines enable row-skipping connections to prevent soliton collisions during signal propagation.

gests, these connections are formed by the intersection of signal lines and the corresponding memristive layer. In the proposed WayMatrix, however, the lines are combined into a single node at the intersection point, the current direction of which can be controlled by switches and diodes. The power of the WayMatrix architecture lies in its potential use as a universal framework for creating programmable and reconfigurable connections between different circuit blocks. WayMatrix makes it easy to set up feedback loops between these blocks, change their connection order, and perform logical operations. We envision it serving as a reconfigurable "backbone" to link various specialized functional units within a larger integrated circuit. For example, the WayMatrix could be configured to connect arrays of memory cells to arithmetic logic units or to route data between different processing cores. Another key application is the creation of programmable clock distribution networks. In such a role, the WayMatrix could manage signal timing across a chip by introducing precise, configurable delays into the clock paths, which is crucial for asynchronous circuit design. This would allow a single hardware platform to be flexibly repurposed for different algorithms by simply re-programming the routing paths, a paradigm central to the development of SPGAs.

The true potential of this architecture, however, is most evident in its application as an axon-synaptic connection matrix for neuromorphic computing. The ability to program connections, enforce directionality, and reconfigure paths makes the WayMatrix an ideal candidate for emulating the complex and plastic connectivity of a biological neural network. In such a system, each soliton acts as a "spike", and the WayMatrix serves as the synaptic network that routes these spikes between artificial neurons. This lays the groundwork for building powerful, event-driven, and energy-efficient spiking neural networks based on the principles we have outlined. In addition to using the WayMatrix, we can reconfigure the neural network itself, program connections between different neurons, implement synaptic pruning, and even "kill" parts of the artificial brain.

Human or animal brains contain a huge number of synapses, many times greater than the number of neurons (e.g., the Norwegian rat brain contains about 200 million neurons, each of which roughly has an average of about 1000 synapses [46]). The ability of a living being to solve certain tasks depends precisely on the number of interneuronal connections. In their attempts to implement such complex systems in hardware, engineers and scientists inevitably face the problem of interconnects and the implementation of a huge number of synaptic connections. The superconducting axon-synaptic matrix based on the WayMatrix concept seems to be a promising solution to the problem [47-50].

As mentioned above repeatedly, the field applications of kinetic inductance and, in particular, KICK, also extend to bio-inspired neuromorphic spiking networks. One important feature of living nervous tissues is the ability to modulate the synaptic delay of signal propagation from one neuron to another. This feature is equally important to implement in hardware artificial realizations of neuromorphic networks. The signal propagation delay is also affected by a length and a conductivity of an axon, which is quite simply imitated by means of a standard Josephson transmission line, as well as by means of all-JJTLs, discussed at the beginning of this article. A simple solution to modulate the propagation delay is to change the length (number of JTL cells) of such an artificial axon, but there is another way. The inductance connected in parallel with the Josephson junctions determines the amount of magnetic energy stored within each JTL cell. Consequently, a larger inductance value results in a longer propagation delay.

Conclusion

This study demonstrates the programmable control of kinetic soliton dynamics in all-Josephson-junction networks through a novel tunable element, the "kinetic inductance controllable key" (KICK). By engineering inhomogeneity via controlled kinetic inductance, we induce distinct dynamical modes (Open mode, Close mode, and T-mode) that fundamentally alter soliton propagation. Furthermore, the features of the proposed cell enable a soliton diode effect, achieving non-reciprocal signal transmission. Building on these principles, we propose two scalable architectures, namely, a programmable switch for reconfigurable routing and the WayMatrix, a versatile $N \times M$ routing matrix. These solutions establish a framework for robust, high-speed superconducting logic that addresses critical bottlenecks in this type of computing.

We realize that the time required to "reprogram" kinetic inductance significantly exceeds the picosecond timescales of Josephson junction dynamics. However, this re-configuration time should be considered in the context of hardware development cycles. From this point of view, the re-configuration time is orders of magnitude lower than the time required to design, fabricate, and test a new application-specific integrated circuit (ASIC), offering a compelling advantage in flexibility and prototyping rate.

The superconducting diodes proposed in this work can be used as a part of synaptic connections in neuromorphic networks to prevent the backward influence of a postsynaptic neuron on a presynaptic neuron through the same connection link. It should also be noted that the signal propagation time between neurons can be controlled by modulating the bias currents, the value of which directly affects the potential barrier in Josephson line (standard JTL or All-JJTL). Thus, the choice of a particular method of signal propagation delay influence depends on the realization of interneuron interactions and the need to adjust a particular interneuron connection. Moreover, these approaches can be combined into one by using a chain of superconductor diodes. Using cells with kinetic inductances, we can change the local propagation speed of spikes in interneuronal signal transmission circuits by smoothly adjusting the delay time. The integration of the WayMatrix will make it possible to change the length of the axonal line as a whole, and thus introduce a delay. Besides, it is really interesting to examine how the dynamics of voltage spike formation in a bio-inspired neuron, proposed in [42], will change if we substitute geometric inductances for kinetic ones. Further development of the idea presented in this article will also address this aspect.

The proposed technique allows for a more compact design and new (diode) functionality of various superconducting computing modules and makes possible further increase of integration density compared to well-known RSFQ technology.

Funding

N.K. and M.K. are grateful to Russian Science Foundation for the support of theoretical study of controlled kinetic inductance as a programmable element for superconducting logic (Project no. 25-19-00057). S.B. and I.S. are grateful the Ministry of Science and Higher Education of the Russian Federation for the support of the study of reconfigurable networks. (Agreement no. 075-15-2025-010). A.M. is grateful to the Foundation for the Advancement of Theoretical Physics and Mathematics "BASIS" (A.M. grant 24-2-10-6-1).

ORCID® iDs

Vsevolod I. Ruzhickiy - https://orcid.org/0000-0002-3411-7050
Anastasia A. Maksimovskaya - https://orcid.org/0009-0002-4197-2263
Sergey V. Bakurskiy - https://orcid.org/0000-0002-6010-6697
Andrey E. Schegolev - https://orcid.org/0000-0002-5381-3297
Maxim V. Tereshonok - https://orcid.org/0000-0003-1330-281X
Mikhail Yu. Kupriyanov - https://orcid.org/0000-0003-1204-9664
Nikolay V. Klenov - https://orcid.org/0000-0001-6265-3670
Igor I. Soloviev - https://orcid.org/0000-0001-9735-2720

Data Availability Statement

Data generated and analyzed during this study is available from the corresponding author upon reasonable request.

Preprint

A non-peer-reviewed version of this article has been previously published as a preprint: https://doi.org/10.3762/bxiv.2025.49.v1

References

1. Likharev, K. K. *Dynamics of Josephson junctions and circuits;* CRC Press: Boca Raton, FL, USA, 1986.
2. Likharev, K. K. *Phys. C (Amsterdam, Neth.)* **2012,** *482,* 6–18. doi:10.1016/j.physc.2012.05.016
3. Holmes, D. S.; Ripple, A. L.; Manheimer, M. A. *IEEE Trans. Appl. Supercond.* **2013,** *23,* 1701610. doi:10.1109/tasc.2013.2244634
4. Tolpygo, S. K. *Low Temp. Phys.* **2016,** *42,* 361–379. doi:10.1063/1.4948618
5. Ahmad, M.; Giagkoulovits, C.; Danilin, S.; Weides, M.; Heidari, H. *Adv. Intell. Syst.* **2022,** *4,* 2200079. doi:10.1002/aisy.202200079
6. Marković, D.; Mizrahi, A.; Querlioz, D.; Grollier, J. *Nat. Rev. Phys.* **2020,** *2,* 499–510. doi:10.1038/s42254-020-0208-2
7. Schneider, M.; Toomey, E.; Rowlands, G.; Shainline, J.; Tschirhart, P.; Segall, K. *Supercond. Sci. Technol.* **2022,** *35,* 053001. doi:10.1088/1361-6668/ac4cd2
8. Jardine, M. A.; Fourie, C. J. *IEEE Trans. Appl. Supercond.* **2023,** *33,* 1302409. doi:10.1109/tasc.2023.3248140
9. Karamuftuoglu, M. A.; Bozbey, A.; Razmkhah, S. *IEEE Trans. Appl. Supercond.* **2023,** *33,* 1400607. doi:10.1109/tasc.2023.3270766
10. Yamanashi, Y.; Nakaishi, S.; Sugiyama, A.; Takeuchi, N.; Yoshikawa, N. *Supercond. Sci. Technol.* **2018,** *31,* 105003. doi:10.1088/1361-6668/aad78d
11. Soloviev, I. I.; Ruzhickiy, V. I.; Bakurskiy, S. V.; Klenov, N. V.; Kupriyanov, M. Yu.; Golubov, A. A.; Skryabina, O. V.; Stolyarov, V. S. *Phys. Rev. Appl.* **2021,** *16,* 014052. doi:10.1103/physrevapplied.16.014052
12. Maksimovskaya, A. A.; Ruzhickiy, V. I.; Klenov, N. V.; Bakurskiy, S. V.; Kupriyanov, M. Y.; Soloviev, I. I. *J. Exp. Theor. Phys. Lett.* **2022,** *115,* 735–741. doi:10.1134/s0021364022600884
13. Salameh, I.; Friedman, E. G.; Kvatinsky, S. *IEEE Trans. Circuits Syst. II: Express Briefs* **2022,** *69,* 2533–2537. doi:10.1109/tcsii.2022.3162723
14. Tanemura, S.; Takeshita, Y.; Li, F.; Nakayama, T.; Tanaka, M.; Fujimaki, A. *IEEE Trans. Appl. Supercond.* **2023,** *33,* 1701305. doi:10.1109/tasc.2023.3258374
15. Jabbari, T.; Bocko, M.; Friedman, E. G. *IEEE Trans. Appl. Supercond.* **2023,** *33,* 1303807. doi:10.1109/tasc.2023.3260774
16. Razmkhah, S.; Pedram, M. *Eng. Res. Express* **2024,** *6,* 015307. doi:10.1088/2631-8695/ad27f5
17. Annunziata, A. J.; Santavicca, D. F.; Frunzio, L.; Catelani, G.; Rooks, M. J.; Frydman, A.; Prober, D. E. *Nanotechnology* **2010,** *21,* 445202. doi:10.1088/0957-4484/21/44/445202
18. Adamyan, A. A.; Kubatkin, S. E.; Danilov, A. V. *Appl. Phys. Lett.* **2016,** *108,* 172601. doi:10.1063/1.4947579
19. Mahashabde, S.; Otto, E.; Montemurro, D.; de Graaf, S.; Kubatkin, S.; Danilov, A. *Phys. Rev. Appl.* **2020,** *14,* 044040. doi:10.1103/physrevapplied.14.044040
20. Splitthoff, L. J.; Bargerbos, A.; Grünhaupt, L.; Pita-Vidal, M.; Wesdorp, J. J.; Liu, Y.; Kou, A.; Andersen, C. K.; van Heck, B. *Phys. Rev. Appl.* **2022,** *18,* 024074. doi:10.1103/physrevapplied.18.024074
21. Wang, C.-G.; Yue, W.-C.; Tu, X.; Chi, T.; Guo, T.; Lyu, Y.-Y.; Dong, S.; Cao, C.; Zhang, L.; Jia, X.; Sun, G.; Kang, L.; Chen, J.; Chen, J.; Wang, Y.-L.; Wang, H.; Wu, P. *Chin. Phys. B* **2024,** *33,* 058402. doi:10.1088/1674-1056/ad2f21
22. Li, J.; Barry, P.; Cecil, T.; Lisovenko, M.; Yefremenko, V.; Wang, G.; Kruhlov, S.; Karapetrov, G.; Chang, C. *Phys. Rev. Appl.* **2024,** *22,* 014080. doi:10.1103/physrevapplied.22.014080
23. Ustavschikov, S. S.; Levichev, M. Y.; Pashenkin, I. Y.; Klushin, A. M.; Vodolazov, D. Y. *Supercond. Sci. Technol.* **2021,** *34,* 015004. doi:10.1088/1361-6668/abc2ad
24. Levichev, M. Y.; Pashenkin, I. Y.; Gusev, N. S.; Vodolazov, D. Y. *Phys. Rev. B* **2023,** *108,* 094517. doi:10.1103/physrevb.108.094517
25. Neilo, A.; Bakurskiy, S.; Klenov, N.; Soloviev, I.; Kupriyanov, M. *Nanomaterials* **2024,** *14,* 245. doi:10.3390/nano14030245
26. Neilo, A. A.; Bakurskiy, S. V.; Klenov, N. V.; Soloviev, I. I.; Kupriyanov, M. Y. *J. Exp. Theor. Phys. Lett.* **2025,** *121,* 58–66. doi:10.1134/s0021364024604391
27. Fourie, C. J.; van Heerden, H. *IEEE Trans. Appl. Supercond.* **2007,** *17,* 538–541. doi:10.1109/tasc.2007.897387
28. Hironaka, Y.; Hosoya, T.; Yamanashi, Y.; Yoshikawa, N. *IEEE Trans. Appl. Supercond.* **2022,** *32,* 1301305. doi:10.1109/tasc.2022.3191984
29. Hosoya, T.; Yamanashi, Y.; Yoshikawa, N. *IEEE Trans. Appl. Supercond.* **2021,** *31,* 1300406. doi:10.1109/tasc.2021.3049771
30. Katam, N. K.; Mukhanov, O. A.; Pedram, M. *IEEE Trans. Appl. Supercond.* **2018,** *28,* 1300212. doi:10.1109/tasc.2018.2797262
31. Schuman, C. D.; Kulkarni, S. R.; Parsa, M.; Mitchell, J. P.; Date, P.; Kay, B. *Nat. Comput. Sci.* **2022,** *2,* 10–19. doi:10.1038/s43588-021-00184-y
32. Kudithipudi, D.; Schuman, C.; Vineyard, C. M.; Pandit, T.; Merkel, C.; Kubendran, R.; Aimone, J. B.; Orchard, G.; Mayr, C.; Benosman, R.; Hays, J.; Young, C.; Bartolozzi, C.; Majumdar, A.; Cardwell, S. G.; Payvand, M.; Buckley, S.; Kulkarni, S.; Gonzalez, H. A.; Cauwenberghs, G.; Thakur, C. S.; Subramoney, A.; Furber, S. *Nature* **2025,** *637,* 801–812. doi:10.1038/s41586-024-08253-8
33. Schegolev, A. E.; Bastrakova, M. V.; Sergeev, M. A.; Maksimovskaya, A. A.; Klenov, N. V.; Soloviev, I. *Mesosci. Nanotechnol.* **2024,** *1,* 01-01005. doi:10.64214/jmsn.01.01005
34. Schegolev, A. E.; Klenov, N. V.; Bakurskiy, S. V.; Soloviev, I. I.; Kupriyanov, M. Y.; Tereshonok, M. V.; Sidorenko, A. S. *Beilstein J. Nanotechnol.* **2022,** *13,* 444–454. doi:10.3762/bjnano.13.37

35. Merolla, P. A.; Arthur, J. V.; Alvarez-Icaza, R.; Cassidy, A. S.; Sawada, J.; Akopyan, F.; Jackson, B. L.; Imam, N.; Guo, C.; Nakamura, Y.; Brezzo, B.; Vo, I.; Esser, S. K.; Appuswamy, R.; Taba, B.; Amir, A.; Flickner, M. D.; Risk, W. P.; Manohar, R.; Modha, D. S. *Science* **2014,** *345,* 668–673. doi:10.1126/science.1254642
36. Indiveri, G.; Liu, S.-C. *Proc. IEEE* **2015,** *103,* 1379–1397. doi:10.1109/jproc.2015.2444094
37. Crotty, P.; Schult, D.; Segall, K. *Phys. Rev. E* **2010,** *82,* 011914. doi:10.1103/physreve.82.011914
38. Goteti, U. S.; Dynes, R. C. *J. Appl. Phys.* **2021,** *129,* 073901. doi:10.1063/5.0027997
39. Semenov, V. K.; Golden, E. B.; Tolpygo, S. K. *IEEE Trans. Appl. Supercond.* **2023,** *33,* 1400308. doi:10.1109/tasc.2023.3252495
40. Feldhoff, F.; Toepfer, H. *IEEE Trans. Appl. Supercond.* **2024,** *34,* 1300105. doi:10.1109/tasc.2024.3355876
41. Skryabina, O. V.; Schegolev, A. E.; Klenov, N. V.; Bakurskiy, S. V.; Shishkin, A. G.; Sotnichuk, S. V.; Napolskii, K. S.; Nazhestkin, I. A.; Soloviev, I. I.; Kupriyanov, M. Y.; Stolyarov, V. S. *Nanomaterials* **2022,** *12,* 1671. doi:10.3390/nano12101671
42. Schegolev, A. E.; Klenov, N. V.; Gubochkin, G. I.; Kupriyanov, M. Y.; Soloviev, I. I. *Nanomaterials* **2023,** *13,* 2101. doi:10.3390/nano13142101
43. Maksimovskaya, A. A.; Ruzhickiy, V. I.; Klenov, N. V.; Schegolev, A. E.; Bakurskiy, S. V.; Soloviev, I. I.; Yakovlev, D. S. *Chaos, Solitons Fractals* **2025,** *193,* 116074. doi:10.1016/j.chaos.2025.116074
44. Dormand, J. R.; Prince, P. J. *J. Comput. Appl. Math.* **1980,** *6,* 19–26. doi:10.1016/0771-050x(80)90013-3
45. Shampine, L. F.; Reichelt, M. W. *SIAM J. Sci. Comput.* **1997,** *18,* 1–22. doi:10.1137/s1064827594276424
46. Swanson, L. W. *J. Comp. Neurol.* **2018,** *526,* 935–943. doi:10.1002/cne.24381
47. Xia, Q.; Yang, J. J. *Nat. Mater.* **2019,** *18,* 309–323. doi:10.1038/s41563-019-0291-x
48. El Mesoudy, A.; Lamri, G.; Dawant, R.; Arias-Zapata, J.; Gliech, P.; Beilliard, Y.; Ecoffey, S.; Ruediger, A.; Alibart, F.; Drouin, D. *Microelectron. Eng.* **2022,** *255,* 111706. doi:10.1016/j.mee.2021.111706
49. Chakraborty, I.; Ali, M.; Ankit, A.; Jain, S.; Roy, S.; Sridharan, S.; Agrawal, A.; Raghunathan, A.; Roy, K. *Proc. IEEE* **2020,** *108,* 2276–2310. doi:10.1109/jproc.2020.3003007
50. Xu, Q.; Wang, J.; Yuan, B.; Sun, Q.; Chen, S.; Yu, B.; Kang, Y.; Wu, F. *IEEE Trans. Autom. Sci. Eng.* **2023,** *20,* 74–87. doi:10.1109/tase.2021.3125065

License and Terms

BEILSTEIN JOURNAL OF NANOTECHNOLOGY

Quantum circuits with SINIS structures

Mikhail Tarasov*[1], Mikhail Fominskii[1], Aleksandra Gunbina[1], Artem Krasilnikov[2,3], Maria Mansfeld[2,3], Dmitrii Kukushkin[3,4], Andrei Maruhno[3], Valeria Ievleva[5], Mikhail Strelkov[1], Daniil Zhogov[1], Konstantin Arutyunov[6,7], Vyacheslav Vdovin[2,3], Vladislav Stolyarov[3] and Valerian Edelman[7]

Full Research Paper

Address:
[1]V. Kotelnikov Institute of Radio Engineering and Electronics RAS, Moscow, Russia, [2]Institute of Applied Physics RAS, Nizhny Novgorod, Russia, [3]Special Astrophysical Observatory RAS, Nizhnii Arkhyz, Russia, [4]ITMO University, Saint Petersburg, Russia, [5]P.N. Lebedev Physical Institute of the Russian Academy of Sciences, 119991 Moscow, [6]National Research University "Higher School of Economics," Moscow, 101000 Russia and [7]P. Kapitza Institute for Physical Problems RAS, Moscow, Russia

Email:
Mikhail Tarasov* - tarasov@hitech.cplire.ru

* Corresponding author

Keywords:
Big Telescope Alt-azimuthal; electron coolers; microwave detectors; micro- and nanotechnology; NIS tunnel junction; superconducting tunnel junctions

Beilstein J. Nanotechnol. **2025,** *16,* 1931–1941.
https://doi.org/10.3762/bjnano.16.134

Received: 12 August 2025
Accepted: 08 October 2025
Published: 04 November 2025

This article is part of the thematic issue "Superconducting artificial neural networks and quantum circuits".

Guest Editor: A. S. Sidorenko

Abstract

The superconductor–insulator–normal metal–insulator–superconductor (SINIS) tunnel junction structure is the basic building block for various cryogenic devices. Microwave detectors, electron coolers, primary thermometers, and Aharonov–Bohm interferometers have been fabricated by various methods and measured at temperatures down to 100 mK. The manufacturing methods included Dolan-type shadow evaporation, Manhattan-type shadow evaporation, and magnetron sputtering with selective etching of superconducting and normal metal electrodes. Improvement in ultimate sensitivity is achieved by suspending the absorber above the substrate. Best responsivity of up to 30 electrons per photon at a frequency of 350 GHz, or 72000 A/W, and voltage responsivity up to 3.9×10^9 V/W were obtained with a black body radiation source and series of band-pass filters. The specially designed SINIS arrays are intended to detect 90 GHz radiation at the “Big Telescope Alt-azimuthal” (romanized Russian: “Bolshoi Teleskop Alt-azimutalnyi”, BTA) with noise equivalent power of less than 10^{-16} $\mathrm{W{\cdot}Hz^{-1/2}}$. The receiver in a ^{3}He cryostat with an optical window was mounted at the Nasmyth focus of the BTA and tested at a temperature of 260 mK with a IMPATT diode radiation source.

Introduction

Modern superconducting electronics is moving towards lower temperatures, lower noise levels, and higher sensitivity, which can be achieved at sub-Kelvin temperatures using aluminum-based tunnel junctions. One group of devices, such as superconducting quantum interference devices (SQUIDs) and rapid single flux quantum circuits, are based on superconductor–insulator–superconductor (SIS) junctions, another uses superconductor–insulator–normal metal (SIN) junctions. Tunnel junctions based on the SIN structure are widely used, and many different devices are manufactured on their basis [1-3]. These extend from cryogenic thermometers [4-6] and electron coolers [7-10] to various detectors such as Andreev bolometers [11-13], cold electron bolometers [14,15], superconductor–insulator–normal metal–insulator–superconductor (SINIS) bolometers [16,17], and SINIS detectors [18-20]. Here, we present an overview and comparison of our SINIS devices manufactured using different methods. The advantage of Al-based technology is the presence of the intrinsic oxide on its surface, which prevents short circuits with subsequent conductive layers and ensures ease of manufacturing a tunnel barrier, in contrast to Nb-based technology, which requires the formation of an artificial anodic oxide or an additional insulating layer to prevent short circuits, as well as an additional Al layer to form an AlO_x or AlN tunnel barrier.

Results

NIS tunnel junction

In tunnel structures, the barrier is a dielectric layer between two metal films (often the oxide layer on the surface of the first metal layer is used as a dielectric). The first experimental study of a tunnel junction was carried out in 1960 [21] for an aluminum–aluminum oxide–lead contact. When tunneling from a normal metal into a superconductor, due to the presence of an energy gap (Δ), only electrons whose energy exceeds Δ can tunnel into the superconductor. Without applying an external voltage or in the case when $eV < \Delta$ ($T = 0$), tunneling does not occur. Accordingly, a tunnel current occurs when $eV > \Delta$. In the case when $T \neq 0$ the I–V curve will be smeared [22].

The current–voltage characteristic of a tunnel NIS junction is determined by the following formula [23]:

$$I = \frac{1}{eR_\text{n}} \int_{-\infty}^{+\infty} N_\text{S}(E)\left[n_\text{N}(E - eV) - n_\text{S}(E)\right] \text{d}E, \qquad (1)$$

where R_n is the asymptotic resistance of the tunnel junction, $N_\text{S}(E)$ is the density of states in the superconductor, n_S is the distribution function in the superconductor, and n_N is the distribution function in the normal metal. At temperatures $T \ll T_\text{c}$ (T_c is the critical temperature of the superconductor), the relationship between the tunnel current and voltage can be written using a simplified formula:

$$I = \frac{2\Delta}{eR_\text{n}} \sqrt{2\pi k_\text{B} T \Delta} \cdot \exp\left(-\frac{\Delta}{k_\text{B}T}\right) \sinh\left(\frac{eV}{k_\text{B}T}\right), \qquad (2)$$

where Δ is the energy gap of the superconductor and k_B is the Boltzmann constant. The differential resistance is expressed by the following formula:

$$R_d = R_\text{n} \sqrt{\frac{k_\text{B}T}{2\pi\Delta}} \cdot \exp\left(\frac{\Delta}{k_\text{B}T}\right) \left(\cosh\left(\frac{eV}{k_\text{B}T}\right)\right)^{-1}. \qquad (3)$$

It should also be noted that, in addition to the tunnel current in NIS structures, the presence of a subgap (Andreev) current caused by the Andreev reflection effect is possible [24]. In general terms, the Andreev reflection process is as follows: An electron from a normal metal hitting the SN boundary, passes into the superconductor in the form of a Cooper pair, and a hole is reflected from the SN boundary back into the normal metal. In the simplest case, the Andreev current can be written as the sum of contributions associated with the transfer of electrons in the normal metal (I_N) and the superconductor (I_S), [25]:

$$I_\text{N} = \frac{\hbar}{e^3 R_\text{n}^2 S \nu_\text{N} d_\text{N}} \tanh \frac{eV}{k_\text{B}T}, \qquad (4)$$

$$I_\text{S} = \frac{\hbar}{e^3 R_\text{n}^2 S \nu_\text{S} d_\text{S}} \frac{eV/\Delta}{2\pi\sqrt{1 - eV/\Delta}}, \qquad (5)$$

where ν_N and ν_S are the densities of electron states in a normal metal and a superconductor, S is the area of the tunnel NIS junction, d_N and d_S are the thicknesses of the normal metal and superconductor films, respectively.

Another feature of the tunnel–NIS junction is the phenomenon of electron cooling. This process is a transfer of heat from a normal metal to a superconductor and is caused by the fact that charge carriers with higher energy (exceeding the value of $\Delta - eV$) move from the metal to the superconductor, and those with lower energy remain in the normal metal. As a result, a heat flow arises from the normal metal (P is the power of electron cooling) [26]:

$$P = Q - IV = \frac{1}{e^2 R_\text{n}} \int_{-\infty}^{+\infty} E N_\text{S}(E)\left[n_\text{N}(E - eV) - n_\text{S}(E)\right] \text{d}E, \qquad (6)$$

where Q is the total power released in the superconductor, IV is the Joule heat, n_N and n_S are the distribution functions of electrons and holes in normal metal and superconductor, respectively. As can be seen from the formula, the electron cooling power depends on both the temperature of the normal metal and the temperature of the superconductor.

Fabrication techniques

Historically, aluminum tunnel junctions were fabricated by shadow evaporation at different angles by the so-called Dolan technology [27]. It requires the formation of a two-layer resist with suspended bridge of the top resist layer (Figure 1a). The advantage of the technique is its simplicity, drawbacks are not very high reproducibility and stability. Another fabrication method is the Manhattan technology [28] with deep orthogonal groves in the resist, see Figure 1b,c. Both methods are based on thermal evaporation at different angles and rotation of substrate, requiring rather sophisticated and expensive deposition plants with thermal or e-beam evaporation. A much more available and simple deposition equipment is magnetron sputtering, but it provides only isotropic deposition, which is incompatible with anisotropic shadow evaporation. The practical solution for a magnetron sputtering is selective etching of different layers of superconducting aluminum and normal metal (e.g., copper). In case of chemical wet etching, this is achieved through an alkali and acid pair, for dry etching, chlorine and fluorine plasmas are used. Alternatively, in the case of magnetron sputtering and separate lithography, ion etching is used before making of the insulator and sputtering of the normal metal (for details see [29]). An example of such a method is presented in Figure 1d,e. Besides SINIS structures with N-absorber on the substrate, we also developed devices with the absorber suspended above the substrate (Figure 1f, technology with wet etching) that are promising for detectors and electron coolers. More details on various technologies and specific features of the fabrication of tunnel structures are provided in a review publication [29].

Aharonov–Bohm interferometer

The Aharonov–Bohm interferometer is a hybrid nanostructure consisting of a T-shaped normal metal electrode (copper), an insulating tunnel layer (aluminum oxide), and a superconducting fork (aluminum), Figure 2a. Tunnel junction size is 0.2×0.2 µm, loop area 2, 4, 8, or 10 μm^2. The transport characteristics of the fabricated interferometers were studied in sorption ^{3}He cryostat at 0.33 K, Figure 2b. The relatively low value of the resistance ratio (R_d/R_n – dynamic resistance/normal resistance) is associated with the high sensitivity of the interferometer to external noise.

NIS thermometers

The I–V characteristic and dynamic resistance of the NIS junction are described by simple relations (Equation 2 and Equation 3), which do not contain fit parameters. In the case of negligibly small Andreev currents suppressed by the ferromagnetic sublayer, such characteristics can be used as primary thermometers [30]. A simple figure of merit for NIS thermometers is the ratio of the resistance at zero bias to the asymptotic one (Equation 7):

$$RR = \left(0.09 T_e / T_c\right) \times \exp\left(1.76 T_e / T_c\right), \tag{7}$$

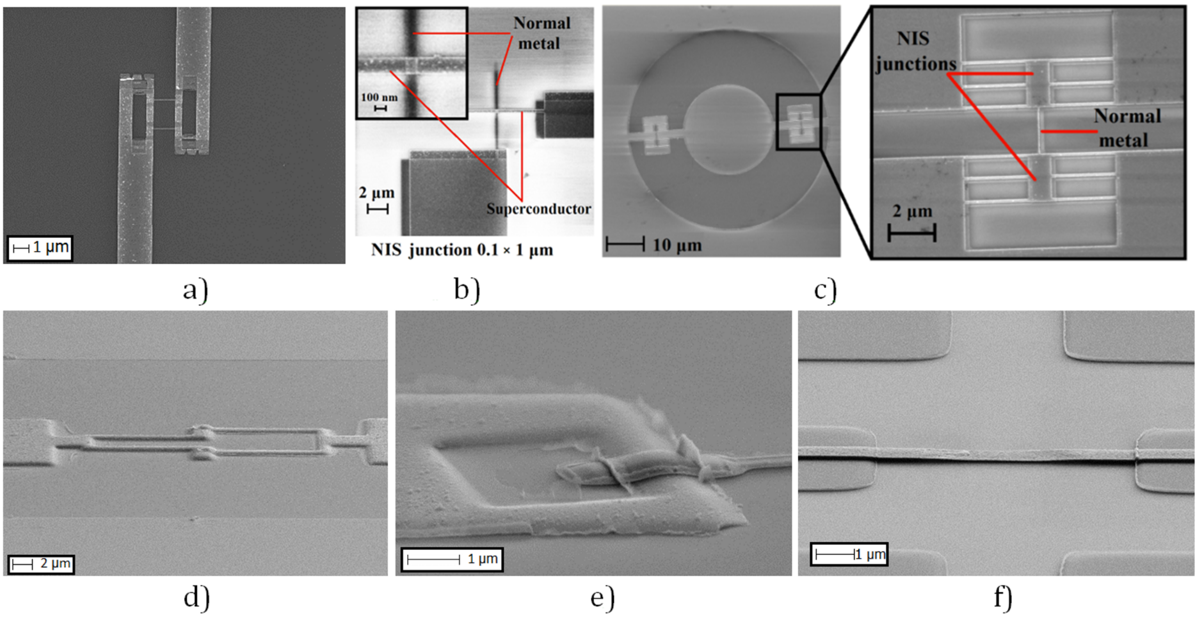

Figure 1: Photos of various tunnel structures fabricated using different technologies. (a) SINIS detector made by using Dolan technology, (b) single tunnel NIS junction and (c) circular antenna with SINIS detector made by Manhattan technology, (d) single SQUID and (e) single NIS junction made by magnetron sputtering with separate lithography, and (f) single SINIS detector with suspended Hf absorber.

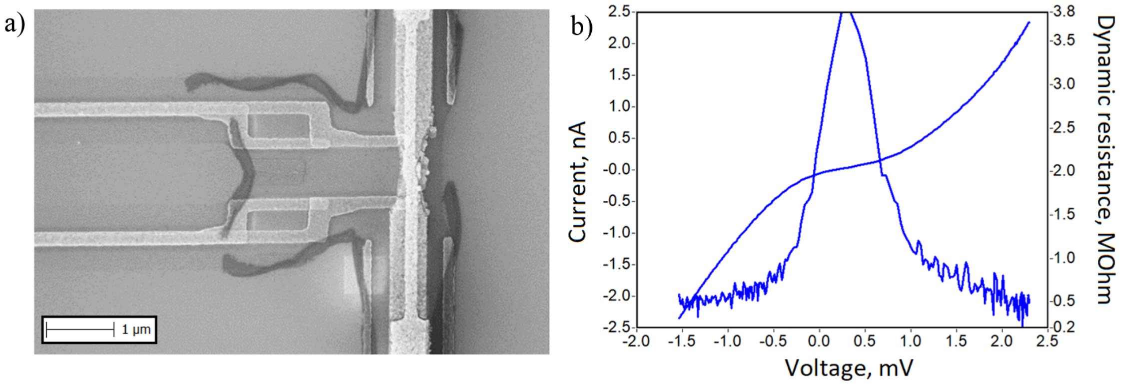

Figure 2: Aharonov–Bohm structure. (a) SEM image of the sample made by Manhattan-type SINIS fabrication and (b) *I–V* curve and dynamic resistance of the Aharonov–Bohm interferometer at 330 mK.

obtained from the general relation in Equation 3. For $I(V) = I_0\exp[(eV - \Delta)/kT_e]$ the temperature sensitivity at low bias current can be approximated as $dV/dT_e = (k/e)\ln(I/I_0) \approx -V_\Delta/T_e$. To reduce the influence of external noise and increase the signal-to-noise ratio, the NIS junctions are connected in series arrays (Figure 3). The temperature dependency of the resistance ratio for aluminum SIN junctions is shown in Figure 4.

Electron coolers

The tunneling current, when biased near the energy gap, carries hot quasiparticles out of the normal electrode, which leads to electron cooling, as in a Peltier element. In a single SINIS structure, it is possible to reduce the electron temperature from 260 to 90 mK [31]. Cascaded NIS coolers can be efficient refrigerators for cooling from 1 K to below 100 mK [32]. One of the

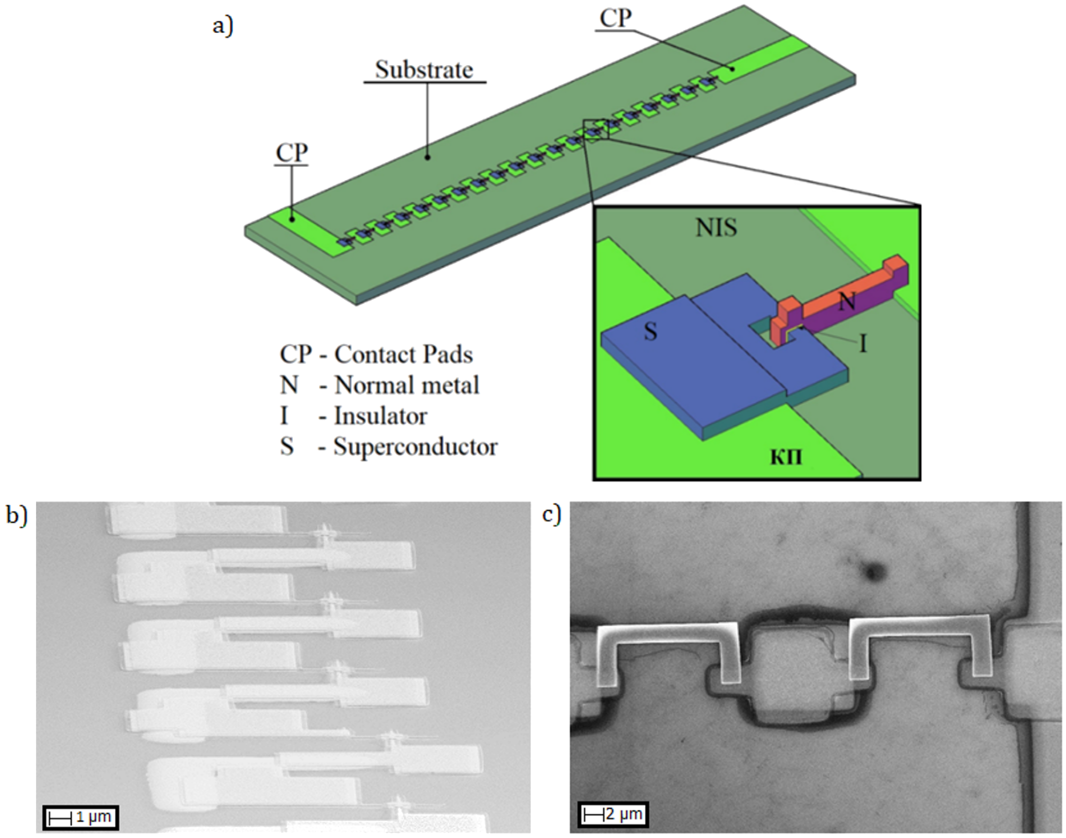

Figure 3: NIS thermometer series array. (a) Schematic view of a thermometer with a chain of 20 NIS junctions and SEM images of thermometers made by (b) Manhattan technology and (c) magnetron sputtering with separate lithography technology.

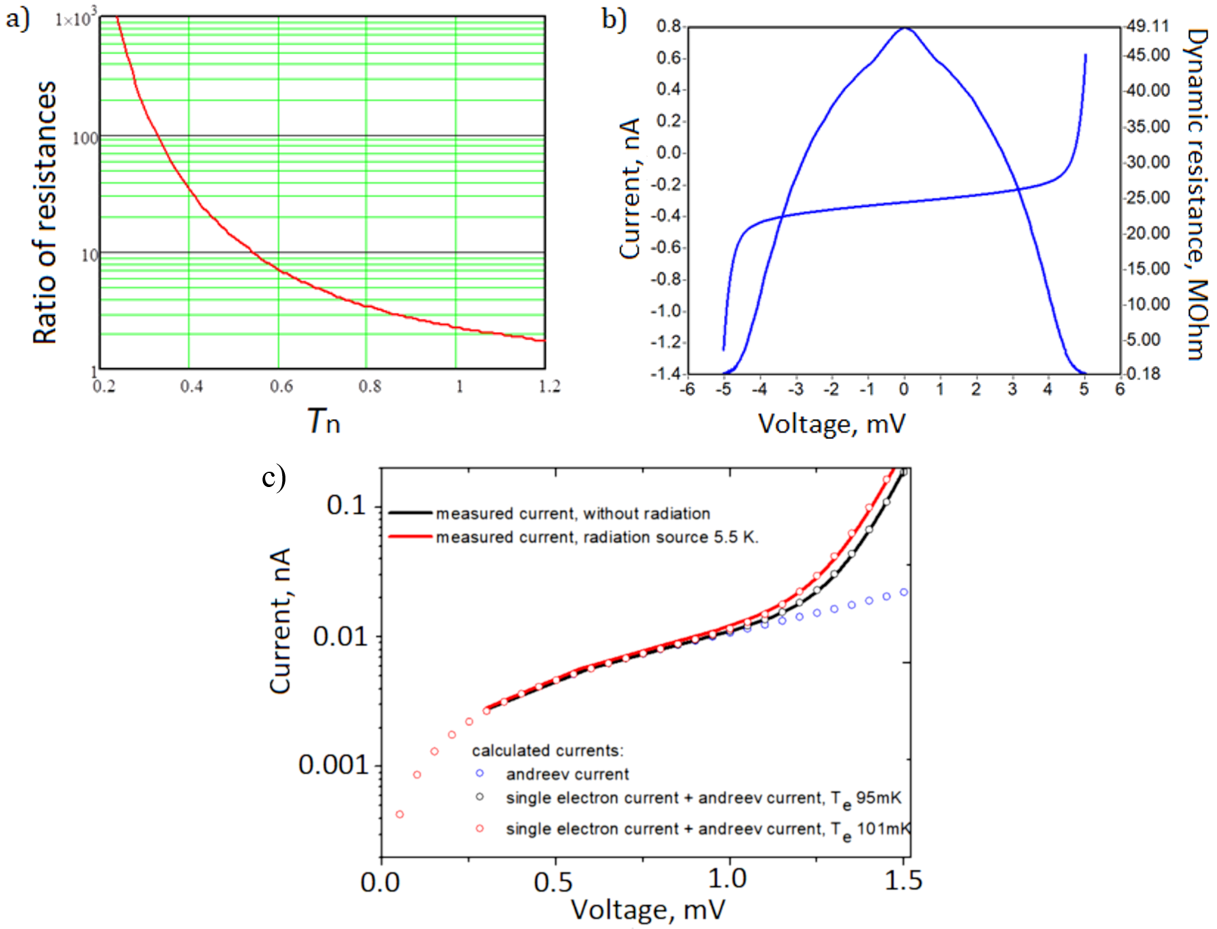

Figure 4: (a) Ratio of resistance at zero bias to the asymptotic resistance using Equation 7, obtained from the general relation in Equation 3. (b) *I*–*V* curve and dynamic resistance for the SINIS thermometer. (c) Measured current with and without radiation. The resistance ratio is R_d/R_n = 15000 at 95 mK and does not respond to radiation at 5.5 K.

problems in explaining results is that, when the injection rate of electrons exceeds the internal relaxation rate in the metal to be cooled, the electrons do not obey the Fermi–Dirac distribution, and the concept of temperature cannot be applied as such. This work is an exciting development towards a fully solid-state, cryogen-free microrefrigerator, which could eventually cover temperatures from the ambient down to the millikelvin range. Figure 5 shows photographs of a two-stage SINIS cooler. The performance of a single-stage SINIS cooler is presented in Figure 6.

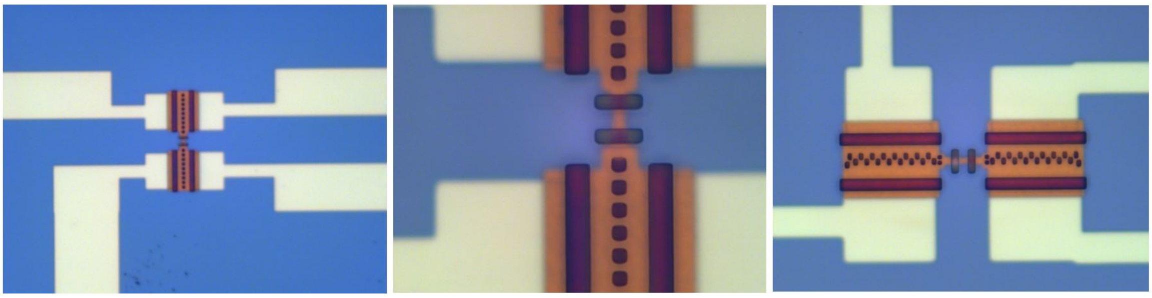

Figure 5: Copper cooler cascade.

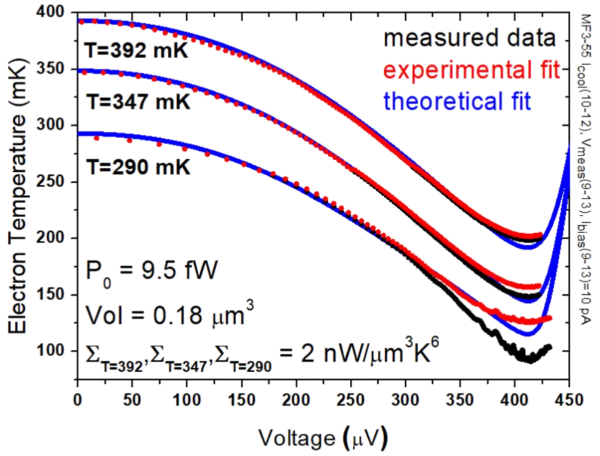

Figure 6: Electron cooling from 392, 347, and 290 mK down to 200, 150, and 95 mK, respectively.

SINIS detectors

The SINIS detector is a thin film of normal metal (the absorber is an element sensitive to incoming radiation) and two NIS junctions that act as a thermometer. An SEM view of the SINIS detector was shown in Figure 1a–f. Often SINIS detectors are considered as classical devices with the optical response equivalent to the electrical response to thermal heating of the absorber by direct current, for example, in [12,14,33-35]. But in practice, the electrical response to heating by direct current is always significantly higher than the optical response for microwave, terahertz, or IR radiation. This is explained by the fact that, in the case of heating the absorber by direct current, the electron temperature of all conduction electrons increases. In the equilibrium state, the electron temperature is determined by the incoming power and the electron–phonon interaction. However, in cases of absorption of a photon with an energy much higher than the thermal energy, the quantum absorption mechanism is already realized, and the real absorption picture becomes much more complicated [19]. It is necessary to take into account many other parameters and relaxation mechanisms. An example of the thermalization process of a radiation quantum with a radiation frequency of 350 GHz is given in [29,36,37]. When an electron absorbs a photon with an energy much higher than the thermal energy, the electron energy will correspond to the electron temperature $hf = kT_e$ of about 16 K for 350 GHz. As a result, a high-energy phonon is created. The process of electron energy relaxation continues until their characteristic times reach the tunneling time determined by the parameters of the SIN transition, that is, the transparency of the barrier, the thickness of the normal metal film, and the diffusion rate of electrons in it. For commonly used structures, this time is of the order of tens of nanoseconds. Typical relaxation times are given in [37,38].

To calculate the sensitivity in the case of heating the absorber with direct current or at low frequencies, the heat balance equation is applicable [12,14]:

$$P_{\text{sig}} + P_{\text{bg}} = \Sigma\Lambda\left(T_{\text{e}}^5 - T_{\text{ph}}^5\right) + P_{\text{cool}}, \tag{8}$$

where P_{sig} is the signal power, P_{bg} is the background radiation power, $\Sigma\Lambda(T_{\text{e}}^5 - T_{\text{ph}}^5)$ is the heat flux from electrons to phonons, Σ is the material constant, Λ is the absorber volume, T_{e} and T_{ph} are, respectively, the electron and phonon temperatures of the absorber, and P_{cool} is the electron cooling power. In other cases, it is necessary to move on to the analysis of collision integrals and the kinetic equation [19,20].

One of the main characteristics of the detector is the noise equivalent power (NEP) [W·Hz$^{-1/2}$], that is, the power of the useful signal in a unit of frequency band, equivalent to the noise power in the device receiving the signal. Approximately, in the simplest case, the NEP of the SINIS detector can be calculated using the following formula:

$$\text{NEP}^2 = \text{NEP}_{\text{e-ph}}^2 + \text{NEP}_{\text{NIS}}^2 + \text{NEP}_{\text{amp}}^2 \tag{9}$$

$\text{NEP}_{\text{e-ph}}$ is the noise equivalent power of electron–phonon interaction, caused by the discreteness of energy exchange between electrons and phonons:

$$\text{NEP}_{\text{e-ph}} = \sqrt{10 k_{\text{B}} \Lambda \Sigma \left(T_{\text{e}}^6 + T_{\text{ph}}^6\right)}, \tag{10}$$

where k_{B} is the Boltzmann constant, Λ is the volume of the absorber, Σ is the constant of electron–phonon interaction, and T_{e} and T_{ph} are the temperatures of the electron and phonon subsystems, respectively. NEP_{NIS} is the noise equivalent power of NIS junction. It is a combination of shot noise that occurs as a result of the charge transfer by electrons during tunneling through the tunnel SIN junction and the thermal noise of these same electrons as heat carriers:

$$\text{NEP}_{\text{NIS}} = \sqrt{\frac{\delta I_\omega^2}{S_V^2}\left(\frac{dV}{dI}\right)^2 + \delta P_\omega^2 - 2\frac{\langle \delta P_\omega \delta I_\omega \rangle}{S_V(i)}\frac{dV}{dI}}. \tag{11}$$

$\delta I_\omega{}^2$ is the power spectral density (PSD) of current fluctuations due to shot noise, $\delta P_\omega{}^2$ is the PSD of thermal fluctuations, and $\langle \delta P_\omega \delta I_\omega \rangle$ is the correlation between the two types of noise. NEP_{amp} is the noise equivalent power of the readout amplifiers. We develop typical characteristics of the detectors based on SINIS structures, namely, volt–watt responsivity no worse than

10^9 V·W^{-1}, noise equivalent power below 10^{-17} W·Hz$^{-1/2}$ (the value is given for measurements with a room-temperature JFET readout system and can be improved by upgrading the readout electronics). As an example, some measured characteristics of the SINIS detectors are given in Figure 7. The amplifier voltage noise is 20 nV·Hz$^{-1/2}$, the optimal input impedance for this amplifier is 500 kΩ, and the maximum response is measured at a bias voltage of 0.5 Δ/e.

The list of designed and fabricated devices contains different arrays of SINIS detectors for frequencies from below 100 GHz to above a few terahertz, broadband detectors integrated with log-periodic antennas, and narrow-band detectors integrated in twin-slot and double-dipole antennas. The miniature size of SINIS detectors allows them to be integrated into antennas of various types. Also, the detector itself is not frequency-selective, but by integrating such devices into various antennas and using additional filter elements, the detecting device can be tuned to the required frequency. Single antennas are convenient to use for test studies or for use under conditions of low background load and signal. This is due to the fact that the saturation level of a single SINIS detector is 0.5–1.0 pW. Under conditions with a high background load (for example, for ground and balloon observations), such detectors are combined into matrices; the power of incoming radiation is distributed between the matrix elements and, accordingly, the dynamic range of the detecting device can be significantly increased.

Deployment at “Big Telescope Alt-azimuthal”

Currently, work is underway to implement the SINIS detectors on a practical instrument, that is, the optical observatory “Big Telescope Alt-azimuthal” (BTA SAO RAS) for observations in the range of 75–110 GHz. The choice of an optical observatory is due to the fact that there are no large-scale subterahertz observatories in Russia, but there are agreements and the possibility of conducting research based on the BTA observatory. Estimates of the possibility of observations, a description of the receiving system, and the current status of the work are given in [39-41]. These works will allow not only to conduct full-scale tests of the SINIS detectors, but will also expand the capabilities of the BTA observatory to the subterahertz range and use it not only for observations, but also for testing new technologies of subterahertz detectors.

According to [42], the thermodynamic temperature of the planets of the solar system at a frequency of 100 GHz can be

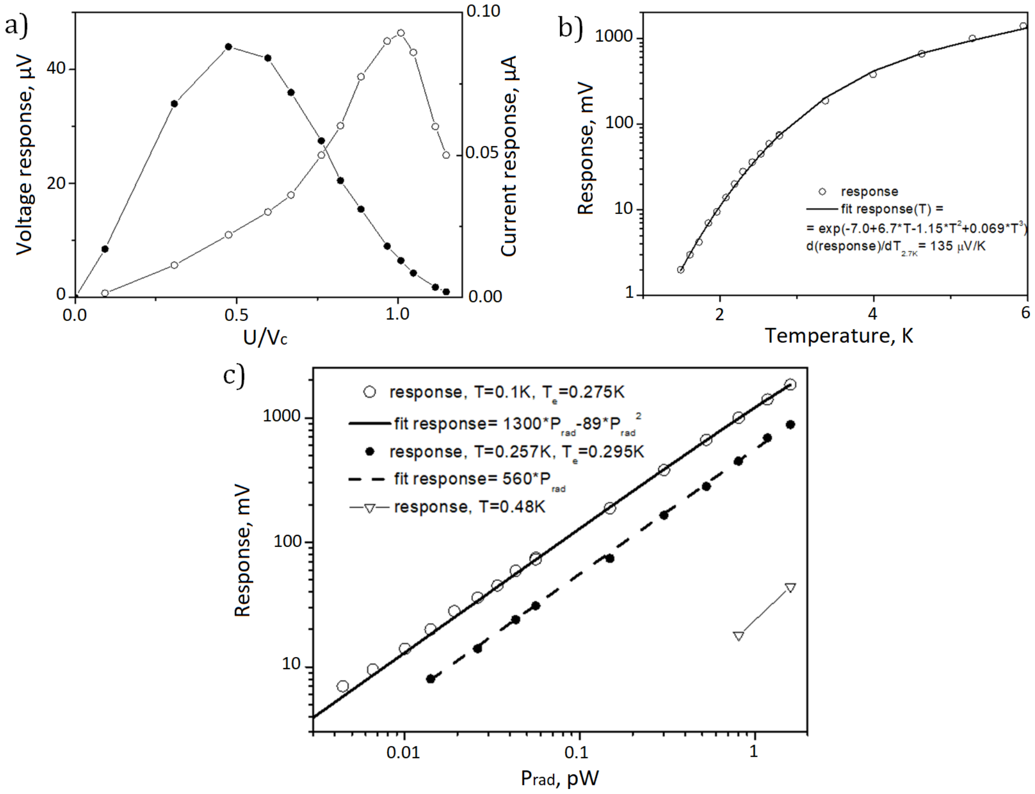

Figure 7: Some of SINIS detectors measured characteristics. (a) Current and voltage response for a parallel array for P_{rad} = 1 pW and maximum current responsivity of dI/dP = 72000 A/W. (b) Voltage response on black body temperature; at 2.7 K, it is dV/dT = 135 µV·K^{-1}, (c) voltage response at temperatures of 0.1, 0.295, and 0.48 K; the maximum response is 3.9 V/nW.

estimated as Mars 198 K, Jupiter 172.6 K, Saturn 145 K, Uranus 121 K, and Neptune 118 K; the brightness temperature of the Moon can vary from 100 to 400 K, depending on the time of day. These values exceed the sky temperature at the zenith for the BTA and can be measured with a signal-to-noise ratio greater than unity by the described receiver even without diagram.

Approximate estimates for observing Jupiter and other planets are made and compared with figures from [42] (central frequency f_c = 100 GHz, bandwidth 10%, Δf = 10 GHz. The thermodynamic temperature of Jupiter at 100 GHz is 172.6 K; the angular diameter of Jupiter is 41.68 arcsec; the BTA main mirror diameter is 6 m, and the aperture efficiency of 0.8 gives an effective area of A_{eff} = 22.6 m^2. The solid angle occupied by Jupiter is of the order of $\Omega = 3.20 \times 10^{-8}$ sr. The spectral flux density is $S = I \times \Omega$ = 1677 Jy = 1.677×10^{-23} W·m^{-2}·Hz^{-1}. For 172.6 K at 100 GHz, we have a blackbody intensity $I = 5.23 \times 10^{-16}$ W·m^{-2}·Hz^{-1}·sr^{-1}. The power density collected by a telescope with an effective aperture of 22.6 m^2 is $P = 3.79 \times 10^{-22}$ W·Hz^{-1}. The total power in the 10% band recorded by the receiver from Jupiter is $P_{\text{tot}} = 3.79 \times 10^{-12}$ W. For planets visible in November 2025 at 100 GHz, the flux densities will be as follows: Jupiter 41.68 arcsec, 172.6 K, 1677.08 Jy; Saturn 18.68 arcsec, 145.7 K, 283.63 Jy; Mars 3.87 arcsec, 192.3 K, 16.13 Jy; Uranus 3.8 arcsec, 120.5 K, 9.67 Jy; and Neptune 2.34 arcsec, 117.4 K, 3.57 Jy.

At this stage, the necessary equipment and elements of the quasi-optical path in the “Nasmyth 1” cabin of the BTA telescope have been installed. Also, primary tests of the quasi-optical path for focusing incoming radiation and irradiation of the source (IMPATT diode) of the detecting matrix in the 75–110 GHz range were carried out. Photos from the expedition are presented in Figure 8. The ratio of resistances on the presented current–voltage characteristic is about 30, which, according to Equation 3, corresponds to an electron temperature of 0.5 K with a physical temperature of 0.26 K.

The array structure was mounted in back-to-back horn matching structure with an optimum for 95 GHz and corresponding quasi-optical band-pass filters (Figure 9). *I*–*V* curves and dynamic resistances are presented in Figure 10a. The resistance ratio is 46, which corresponds to an electron temperature of about 0.36 K. In these measurements, there was no optical window and no strong overheating of the sample by radiation.

a) b)

Figure 8: Installation and initial testing of the receiving system based on SINIS detectors at the BTA SAO RAS observatory. (a) Installed racks with a Heliox AC-V cryostat and (b) measured *I*–*V* characteristics of the SINIS detector matrix installed inside the cryostat with a closed optical window and under irradiation by the source; The lower part demonstrates a PT2 temperature of 2.6 K and a ^{3}He pot temperature of 263 mK.

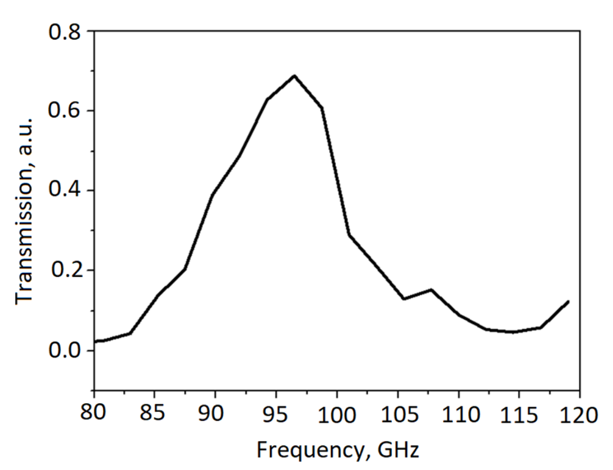

Figure 9: Transmission spectrum of the cold mesh filter.

Discussion

We have designed, fabricated, and experimentally studied a family of aluminum SINIS devices. Microwave detectors at 100 mK demonstrated responsivity up to 10^9 V·W^{-1}, array of NIS thermometers provide sensitivity down to 10 μK, electron coolers can reduce the electron temperature of a normal metal absorber from 280 mK down to 100 mK, and the SINIS receiver for a frequency of 95 GHz was installed on the BTA telescope and tested at a temperature of 260 mK.

Funding

Work is supported by grant from Ministry of science and higher education of Russian Federation No:075-15-2024-482.

Author Contributions

Mikhail Tarasov: supervision. Mikhail Fominskii: data curation. Aleksandra Gunbina: data curation. Artem Krasilnikov: methodology. Maria Mansfeld: data curation. Dmitrii Kukushkin: data curation. Andrei Maruhno: resources. Valeria Ievleva: validation. Mikhail Strelkov: visualization. Daniil Zhogov: investigation. Konstantin Arutyunov: writing – original draft. Vyacheslav Vdovin: writing – review & editing. Vladislav Stolyarov: validation. Valerian Edelman: writing – review & editing.

ORCID® iDs

Mikhail Tarasov - https://orcid.org/0000-0002-8330-9163
Mikhail Fominskii - https://orcid.org/0000-0001-6529-0465
Aleksandra Gunbina - https://orcid.org/0000-0002-0308-142X
Dmitrii Kukushkin - https://orcid.org/0009-0008-2186-3071
Valeria Ievleva - https://orcid.org/0009-0003-1448-0244
Vladislav Stolyarov - https://orcid.org/0000-0001-8151-828X

Data Availability Statement

Data generated and analyzed during this study is available from the corresponding author upon reasonable request.

References

1. Giazotto, F.; Heikkilä, T. T.; Luukanen, A.; Savin, A. M.; Pekola, J. P. *Rev. Mod. Phys.* **2006,** *78,* 217–274. doi:10.1103/revmodphys.78.217
2. Ullom, J. N. *AIP Conf. Proc.* **2002,** *605,* 135–140. doi:10.1063/1.1457613
3. Tarasov, M.; Edelman, V. Nanodevices with Normal Metal—Insulator—Superconductor Tunnel Junctions. In *Functional Nanostructures and Metamaterials for Superconducting Spintronics;* Sidorenko, A., Ed.; NanoScience and Technology; Springer International Publishing: Cham, Switzerland, 2018; pp 91–116. doi:10.1007/978-3-319-90481-8_5
4. Feshchenko, A. V.; Casparis, L.; Khaymovich, I. M.; Maradan, D.; Saira, O.-P.; Palma, M.; Meschke, M.; Pekola, J. P.; Zumbühl, D. M. *Phys. Rev. Appl.* **2015,** *4,* 034001. doi:10.1103/physrevapplied.4.034001
5. Pekola, J. P. *J. Low Temp. Phys.* **2004,** *135,* 723–744. doi:10.1023/b:jolt.0000029516.18146.42

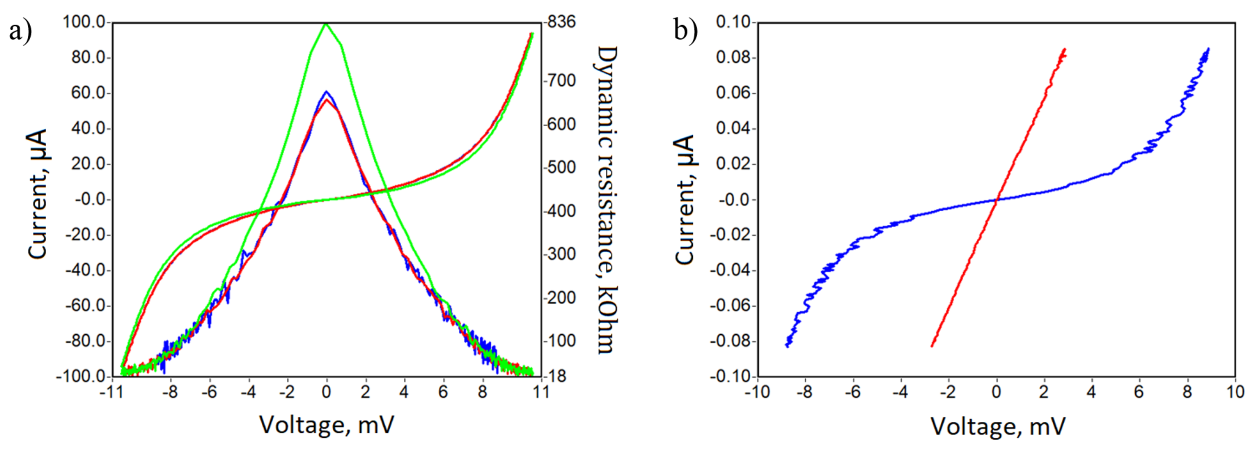

Figure 10: (a) *I–V* curves and dynamic resistance of series SINIS array and (b) *I–V* curve without (blue) and with (red) microwave radiation at 95 GHz.

6. Isosaari, E.; Holmqvist, T.; Meschke, M.; Heinonen, M.; Pekola, J. P. *Eur. Phys. J.: Spec. Top.* **2009,** *172,* 323–332. doi:10.1140/epjst/e2009-01057-y
7. Pekola, J. P.; Manninen, A. J.; Leivo, M. M.; Arutyunov, K.; Suoknuuti, J. K.; Suppula, T. I.; Collaudin, B. *Phys. B (Amsterdam, Neth.)* **2000,** *280,* 485–490. doi:10.1016/s0921-4526(99)01842-6
8. Nguyen, H. Q.; Aref, T.; Kauppila, V. J.; Meschke, M.; Winkelmann, C. B.; Courtois, H.; Pekola, J. P. *New J. Phys.* **2013,** *15,* 085013. doi:10.1088/1367-2630/15/8/085013
9. Clark, A. M.; Miller, N. A.; Williams, A.; Ruggiero, S. T.; Hilton, G. C.; Vale, L. R.; Beall, J. A.; Irwin, K. D.; Ullom, J. N. *Appl. Phys. Lett.* **2005,** *86,* 173508. doi:10.1063/1.1914966
10. O'Neil, G. C. Improving NIS Tunnel Junction Refrigerators: Modeling, Materials, and Traps. Ph.D. Thesis, Boulder, Colorado, 2011.
11. Nahum, M.; Martinis, J. M. *Appl. Phys. Lett.* **1993,** *63,* 3075–3077. doi:10.1063/1.110237
12. Nahum, M.; Richards, P. L.; Mears, C. A. *IEEE Trans. Appl. Supercond.* **1993,** *3,* 2124–2127. doi:10.1109/77.233921
13. Vystavkin, A. N.; Shuvaev, D. V.; Kuz'min, L. S.; Tarasov, M. A.; Aderstedt, E.; Willander, M.; Claeson, T. *J. Exp. Theor. Phys.* **1999,** *88,* 598–602. doi:10.1134/1.558834
14. Kuzmin, L. S.; Devyatov, I. A.; Golubev, D. *Proc. SPIE* **1998,** *3465,* 193–199. doi:10.1117/12.331165
15. Brien, T. L. R.; Ade, P. A. R.; Barry, P. S.; Dunscombe, C.; Leadley, D. R.; Morozov, D. V.; Myronov, M.; Parker, E. H. C.; Prest, M. J.; Prunnila, M.; Sudiwala, R. V.; Whall, T. E.; Mauskopf, P. D. *Appl. Phys. Lett.* **2014,** *105,* 043509. doi:10.1063/1.4892069
16. Schmidt, D. R.; Duncan, W. D.; Irwin, K. D.; Lehnert, K. W.; Miller, N. A.; Ullom, J. N. *Nucl. Instrum. Methods Phys. Res., Sect. A* **2006,** *559,* 516–518. doi:10.1016/j.nima.2005.12.043
17. Schmidt, D. R.; Lehnert, K. W.; Clark, A. M.; Duncan, W. D.; Irwin, K. D.; Miller, N.; Ullom, J. N. *Appl. Phys. Lett.* **2005,** *86,* 053505. doi:10.1063/1.1855411
18. Tarasov, M.; Gunbina, A.; Chekushkin, A.; Yusupov, R.; Edelman, V.; Koshelets, V. *Appl. Sci.* **2022,** *12,* 10525. doi:10.3390/app122010525
19. Devyatov, I. A.; Krutitskiĭ, P. A.; Kupriyanov, M. Y. *J. Exp. Theor. Phys. Lett.* **2006,** *84,* 57–61. doi:10.1134/s0021364006140037
20. Devyatov, I. A.; Kupriyanov, M. Y. *J. Exp. Theor. Phys. Lett.* **2004,** *80,* 646–650. doi:10.1134/1.1857272
21. Giaever, I. *Phys. Rev. Lett.* **1960,** *5,* 147–148. doi:10.1103/physrevlett.5.147
22. Schmidt, V. V. *Introduction to physics of superconductivity,* 2nd ed.; MCCME, 2000.
23. Giaever, I.; Megerle, K. *Phys. Rev.* **1961,** *122,* 1101–1111. doi:10.1103/physrev.122.1101
24. Andreev, A. F. *Sov. Phys. - JETP* **1964,** *19,* 1228–1231.
25. Hekking, F. W. J.; Nazarov, Yu. V. *Phys. Rev. B* **1994,** *49,* 6847–6852. doi:10.1103/physrevb.49.6847
26. Leivo, M. M.; Pekola, J. P.; Averin, D. V. *Appl. Phys. Lett.* **1996,** *68,* 1996–1998. doi:10.1063/1.115651
27. Dolan, G. J. *Appl. Phys. Lett.* **1977,** *31,* 337–339. doi:10.1063/1.89690
28. Aleksandrovich, T. M.; Vladimirovna, N. D.; Anatolevna, G. A.; Yurevich, F. M. Method of making devices with thin-film tunnel junctions. RU 2733330 C1, Oct 1, 2020.
29. Gunbina, A.; Tarasov, M.; Fominsky, M.; Chekushkin, A.; Yusupov, R.; Nagirnaya, D. Fabrication of aluminium nanostructures for microwave detectors based on tunnel junctions. In *Advances in Microelectronics Reviews;* Sergey, Y. Y., Ed.; IFSA Publishing: Barcelona, Spain, 2021; Vol. 3, pp 183–212. ISBN 978-84-09-33338-7/978-84-09-33339-4.
30. Pekola, J. P.; Holmqvist, T.; Meschke, M. *Phys. Rev. Lett.* **2008,** *101,* 206801. doi:10.1103/physrevlett.101.206801
31. Tarasov, M. A.; Kuz'min, L. S.; Fominskii, M. Yu.; Agulo, I. E.; Kalabukhov, A. S. *J. Exp. Theor. Phys. Lett.* **2003,** *78,* 714–717. doi:10.1134/1.1648293
32. Kemppinen, A.; Ronzani, A.; Mykkänen, E.; Hätinen, J.; Lehtinen, J. S.; Prunnila, M. *Appl. Phys. Lett.* **2021,** *119,* 052603. doi:10.1063/5.0060652
33. Clarke, J.; Hoffer, G. I.; Richards, P. L. *Rev. Phys. Appl.* **1974,** *9,* 69–71. doi:10.1051/rphysap:019740090106900
34. Kuzmin, L. S.; Pankratov, A. L.; Gordeeva, A. V.; Zbrozhek, V. O.; Shamporov, V. A.; Revin, L. S.; Blagodatkin, A. V.; Masi, S.; de Bernardis, P. *Commun. Phys.* **2019,** *2,* 104. doi:10.1038/s42005-019-0206-9
35. Gordeeva, A. V.; Zbrozhek, V. O.; Pankratov, A. L.; Revin, L. S.; Shamporov, V. A.; Gunbina, A. A.; Kuzmin, L. S. *Appl. Phys. Lett.* **2017,** *110,* 162603. doi:10.1063/1.4982031
36. Yusupov, R. A.; Gunbina, A. A.; Chekushkin, A. M.; Nagirnaya, D. V.; Lemzyakov, S. A.; Edel'man, V. S.; Tarasov, M. A. *Phys. Solid State* **2020,** *62,* 1567–1570. doi:10.1134/s106378342009036x
37. Tarasov, M.; Gunbina, A.; Yusupov, R.; Chekushkin, A.; Nagirnaya, D.; Lemzyakov, S.; Vdovin, V.; Edelman, V.; Kalaboukhov, A.; Winkler, D. *IEEE Trans. Appl. Supercond.* **2021,** *31,* 2300105. doi:10.1109/tasc.2021.3057327
38. Gershenson, M. E.; Gong, D.; Sato, T.; Karasik, B. S.; Sergeev, A. V. *Appl. Phys. Lett.* **2001,** *79,* 2049–2051. doi:10.1063/1.1407302
39. Balega, Y.; Bubnov, G.; Chekushkin, A.; Dubrovich, V.; Edelman, V.; Gunbina, A.; Kapustin, S.; Khabarova, T.; Kukushkin, D.; Lapkin, I.; Mansfeld, M.; Maruhno, A.; Parshin, V.; Raevskiy, A.; Stolyarov, V.; Tarasov, M.; Valyavin, G.; Vdovin, V.; Yakopov, G.; Yusupov, R.; Zemlyanukha, P.; Zinchenko, I. *Sensors* **2024,** *24,* 359. doi:10.3390/s24020359
40. Stolyarov, V. A.; Balega, Y. Y.; Mingaliev, M. G.; Sotnikova, Y. V.; Vdovin, V. F.; Gunbina, A. A.; Kukushkin, D. E.; Tarasov, M. A.; Fominsky, M. Y.; Chekushkin, A. M.; Edelman, V. S.; Yusupov, R. A. *Astrophys. Bull.* **2024,** *79,* 321–339. doi:10.1134/s1990341324600467
41. Tarasov, M. A.; Gunbina, A. A.; Checkushkin, A. M.; Markina, M. A.; Ysupov, R. A.; Fominskii, M. Y.; Filippenko, L. V.; Edelman, V. S.; Vdovin, V. F.; Stolyarov, V. A.; Zinchenko, I.; Krasilnikov, A. M.; Maruhno, A. S.; Mansfeld, M. A.; Kukushkin, D. E.; Sazonenko, D. A.; Bolshakov, O. S.; Ermakov, A. B.; Lesnov, I. V.; Valeev, A. F. *Astrophys. Bull.* **2025,** *80,* 502–518.

42. Akrami, Y.; Ashdown, M.; Aumont, J.; Baccigalupi, C.; Ballardini, M.; Banday, A. J.; Barreiro, R. B.; Bartolo, N.; Basak, S.; Benabed, K.; Bernard, J.-P.; Bersanelli, M.; Bielewicz, P.; Bonavera, L.; Bond, J. R.; Borrill, J.; Bouchet, F. R.; Boulanger, F.; Bucher, M.; Burigana, C.; Butler, R. C.; Calabrese, E.; Cardoso, J.-F.; Carron, J.; Chiang, H. C.; Colombo, L. P. L.; Comis, B.; Couchot, F.; Coulais, A.; Crill, B. P.; Curto, A.; Cuttaia, F.; de Bernardis, P.; de Rosa, A.; de Zotti, G.; Delabrouille, J.; Di Valentino, E.; Dickinson, C.; Diego, J. M.; Doré, O.; Ducout, A.; Dupac, X.; Elsner, F.; Enßlin, T. A.; Eriksen, H. K.; Falgarone, E.; Fantaye, Y.; Finelli, F.; Frailis, M.; Fraisse, A. A.; Franceschi, E.; Frolov, A.; Galeotta, S.; Galli, S.; Ganga, K.; Génova-Santos, R. T.; Gerbino, M.; González-Nuevo, J.; Górski, K. M.; Gruppuso, A.; Gudmundsson, J. E.; Hansen, F. K.; Helou, G.; Henrot-Versillé, S.; Herranz, D.; Hivon, E.; Jaffe, A. H.; Jones, W. C.; Keihänen, E.; Keskitalo, R.; Kiiveri, K.; Kim, J.; Kisner, T. S.; Krachmalnicoff, N.; Kunz, M.; Kurki-Suonio, H.; Lagache, G.; Lamarre, J.-M.; Lasenby, A.; Lattanzi, M.; Lawrence, C. R.; Le Jeune, M.; Lellouch, E.; Levrier, F.; Liguori, M.; Lilje, P. B.; Lindholm, V.; López-Caniego, M.; Ma, Y.-Z.; Macías-Pérez, J. F.; Maggio, G.; Maino, D.; Mandolesi, N.; Maris, M.; Martin, P. G.; Martínez-González, E.; Matarrese, S.; Mauri, N.; McEwen, J. D.; Melchiorri, A.; Mennella, A.; Migliaccio, M.; Miville-Deschênes, M.-A.; Molinari, D.; Moneti, A.; Montier, L.; Moreno, R.; Morgante, G.; Natoli, P.; Oxborrow, C. A.; Paoletti, D.; Partridge, B.; Patanchon, G.; Patrizii, L.; Perdereau, O.; Piacentini, F.; Plaszczynski, S.; Polenta, G.; Rachen, J. P.; Racine, B.; Reinecke, M.; Remazeilles, M.; Renzi, A.; Rocha, G.; Romelli, E.; Rosset, C.; Roudier, G.; Rubiño-Martín, J. A.; Ruiz-Granados, B.; Salvati, L.; Sandri, M.; Savelainen, M.; Scott, D.; Sirri, G.; Spencer, L. D.; Suur-Uski, A.-S.; Tauber, J. A.; Tavagnacco, D.; Tenti, M.; Toffolatti, L.; Tomasi, M.; Tristram, M.; Trombetti, T.; Valiviita, J.; Van Tent, F.; Vielva, P.; Villa, F.; Wehus, I. K.; Zacchei, A. *Astron. Astrophys.* **2017,** *607,* A122. doi:10.1051/0004-6361/201630311

License and Terms

The definitive version of this article is the electronic one which can be found at:
https://doi.org/10.3762/bjnano.16.134

BEILSTEIN JOURNAL OF NANOTECHNOLOGY

Hartree–Fock interaction in superconducting condensate fractals

Edward G. Nikonov[1,2], Yajiang Chen[*3], Mauro M. Doria[4] and Arkady A. Shanenko[*1]

Full Research Paper

Address:
[1]HSE University, 101000 Moscow, Russia, [2]Meshcheryakov Laboratory of Information Technologies, Joint Institute for Nuclear Research, Dubna, Russia, [3]Zhejiang Key Laboratory of Quantum State Control and Optical Field Manipulation, Department of Physics, Zhejiang Sci-Tech University, 310018 Hangzhou, China and [4]Instituto de Física, Universidade Federal do Rio de Janeiro, 21941-972 Rio de Janeiro, Brazil

Email:
Yajiang Chen[*] - yjchen@zstu.edu.cn; Arkady A. Shanenko[*] - ashanenko@hse.ru

[*] Corresponding author

Keywords:
Fibonacci chain; fractal superconductivity; Hartree–Fock interaction; quasicrystal

Beilstein J. Nanotechnol. **2025,** *16,* 2177–2182.
https://doi.org/10.3762/bjnano.16.150

Received: 29 October 2025
Accepted: 27 November 2025
Published: 04 December 2025

This article is part of the thematic issue "Superconducting artificial neural networks and quantum circuits".

Guest Editor: A. S. Sidorenko

Abstract

It is well known that the Hartree–Fock (HF) interaction does not alter observables in conventional superconductors as its effect is mainly reduced to a chemical potential shift. Deviations from this behavior can only arise in situations of translational symmetry breaking, for example, caused by the presence of external fields that induce spatial variations of the order parameter and electron density. We demonstrate that this scenario changes fundamentally in quasicrystalline systems, where the intrinsic lack of translational symmetry leads to a fractal spatial distribution of the superconducting condensate and electron density. By investigating a Fibonacci chain as a prototype quasicrystal, we numerically solve the Bogoliubov–de Gennes equations and show that, beyond the half-filling, the HF potential significantly enhances the self-similar spatial oscillations of the order parameter while simultaneously reducing its average value and altering its critical exponent. Consequently, the critical temperature is suppressed; for our chosen microscopic parameters, this suppression can reach up to 20%. Therefore, an accurate analysis of condensate distribution and related quantities in quasicrystalline superconductors requires the comparison of results obtained with and without the HF interaction.

Introduction

It is well known, dating back to the classical book by de Gennes [1], that, in conventional superconducting materials, the Hartree–Fock (HF) interaction merely reduces to a shift of the chemical potential, as the observables are not affected due to translational invariance. Hence, the HF field is a kind of “spectator” that defines the single-particle states and chemical potential but does not act on the pair formation and, thus, can be neglected, as in the standard formulation of the BCS model [2,3]. Nevertheless, the HF potential cannot be neglected in the presence of external fields [4], such as impurity potentials [5,6], quantum confinement in nanoscale superconductors [7], and potential barriers at interfaces [8]. Such external fields break the translational invariance, which is the condition for the HF field to make a contribution to the formation of the superconducting condensate.

This raises an interesting question about systems that exhibit an intrinsic lack of translational invariance even in the absence of any applied field. Among those are quasicrystals, which were first discovered in 1984 [9-11]. Quasicrystals exhibit long-range orientational order, such as the fivefold symmetry in $Al_{86}Mn_{14}$ alloys [9,10], but lack the translational invariance [11]. The superconductivity of quasicrystals was established in 2018 with the discovery of superconducting signatures in an Al–Zn–Mg alloy below a critical temperature of $T_c \sim 0.05$ K [12]. More recently, in 2024 and 2025, much higher critical temperatures of $T_c \sim 1$ K and $T_c \sim 5.47$ K were reported in van der Waals-layered dodecagonal quasicrystals $Ta_{1.6}Te$ [13] and in a monoclinic approximant to the decagonal quasicrystal $Al_{13}Os_4$[14], respectively.

Experimental observations of the superconductivity in quasicrystals ignited big interest regarding many open problems related to the superconducting condensate in quasiperiodic systems. Most of the recent results were obtained for a superconducting Fibonacci chain, being a simplified one-dimensional model for superconducting quasicrystals [15]. Using this model, researchers explored a range of phenomena in quasiperiodic systems, including proximity effects in quasicrystal–metal hybrids [16-18], enhanced superconductivity from staggered hopping amplitudes [19], and the interplay between the Josephson effect and quasiperiodicity [20]. The model has also been used to investigate topological superconductivity [21] and anomalous local critical temperatures (at the left end, at the right end, and at the chain center) in quasiperiodic chains [22]. These investigations demonstrate that the spatial distribution of the superconducting condensate in quasiperiodic chains exhibits a distinct fractal character, with significant oscillations of the order parameter along the system. A similar fractal inhomogeneous distribution of the pair condensate has been calculated for Penrose and Ammann–Beenker tilings [23], well-known representations of two-dimensional quasicrystals.

Recent studies confirm that the superconducting condensate in quasiperiodic systems possesses a highly nontrivial spatial structure. This finding naturally raises the question of how sensitive the theoretical predictions for quasicrystalline superconductors are to the inclusion of the HF potential in the fundamental microscopic equations. Our work addresses this open problem through an investigation of the superconducting Fibonacci chain, a standard prototype for quasiperiodic systems.

Bogoliubov–de Gennes Equations for Superconducting Fibonacci Chains

To investigate the superconducting properties of a Fibonacci chain, we use an attractive Hubbard model with the grand-canonical Hamiltonian (absorbing the chemical potential μ) given by [4-6,8,19,22],

$$\hat{H} = -\sum_{ij\sigma} t_{\langle ij\rangle} c^{\dagger}_{i\sigma} c_{j\sigma} - \sum_{i\sigma} \mu \hat{n}_{i\sigma} - g \sum_{i} \hat{n}_{i\uparrow} \hat{n}_{i\downarrow}, \qquad (1)$$

where $c_{i\sigma}$ and $c^{\dagger}_{i\sigma}$ are, respectively, the annihilation and creation operators of an electron with the spin projection $\sigma = (\uparrow, \downarrow)$ at sites $i = 1,\ldots,N$, $t_{\langle ij\rangle}$ is the hopping amplitude between the nearest neighboring sites, $\hat{n}_{i\sigma} = c^{\dagger}_{i\sigma} c_{i\sigma}$, and $g > 0$ is the on-site attractive electron–electron interaction.

Within the mean-field approximation, the Hamiltonian in Equation 1 is reduced [4] to the effective BCS–Bogoliubov Hamiltonian in the form (for the s-wave pairing):

$$\hat{H}_{\text{eff}} = \sum_{ij\sigma} h_{ij} c^{\dagger}_{i\sigma} c_{j\sigma} + \sum_{i} \left[\Delta(i) c^{\dagger}_{i\uparrow} c^{\dagger}_{i\downarrow} + \Delta^{*}(i) c_{i\downarrow} c_{i\uparrow} \right], \qquad (2)$$

where

$$h_{ij} = -t_{\langle ij\rangle} - \delta_{ij} \left[\mu - U_{\text{HF}}(i) \right], \qquad (3)$$

with δ_{ij} the Kronecker delta, and $\Delta(i)$ and $U_{\text{HF}}(i)$ the superconducting order parameter and the HF interaction potential, respectively. The latter obey the self-consistency relations

$$\Delta(i) = g \left\langle c_{i\uparrow} c_{i\downarrow} \right\rangle, \quad U_{\text{HF}}(i) = -g \left\langle \hat{n}_{i\uparrow} \right\rangle = -g \left\langle \hat{n}_{i\downarrow} \right\rangle; \qquad (4)$$

here, we exclude spin-imbalanced regimes in which $\langle \hat{n}_{i\uparrow} \rangle \neq \langle \hat{n}_{i\downarrow} \rangle$.

The effective Hamiltonian is diagonalized by applying the Bogoliubov–Valatin transformation [4],

$$\begin{pmatrix} c_{i\uparrow} \\ c^{\dagger}_{i\downarrow} \end{pmatrix} = \sum_{\nu} \begin{pmatrix} u_{\nu}(i) & -v^{*}_{\nu}(i) \\ v_{\nu}(i) & u^{*}_{\nu}(i) \end{pmatrix} \begin{pmatrix} \gamma_{\nu\uparrow} \\ \gamma^{\dagger}_{\nu\downarrow} \end{pmatrix}, \qquad (5)$$

where $u_\nu(i)$ and $v_\nu(i)$ are, respectively, the particle-like and hole-like quasiparticle (bogolon) wavefunctions, and $\gamma_{\nu\sigma}$ and $\gamma^\dagger_{\nu\sigma}$ are the annihilation and creation operators for bogolon state ν, σ, respectively. The quasiparticle wave functions obey the Bogoliubov–de Gennes equations

$$\begin{aligned}\sum_j h_{ij} u_\nu(j) + \Delta(i) v_\nu(i) &= \varepsilon_\nu u_\nu(i),\\ \Delta^*(i) u_\nu(i) - \sum_j h^*_{ij} v_\nu(j) &= \varepsilon_\nu v_\nu(i),\end{aligned} \tag{6}$$

where ε_ν is the quasiparticle energy. As a result of the diagonalization, one obtains

$$\left\langle \gamma^\dagger_{\nu\uparrow}\gamma_{\nu\uparrow}\right\rangle = \left\langle \gamma^\dagger_{\nu\downarrow}\gamma_{\nu\downarrow}\right\rangle = f_\nu, \quad \left\langle \gamma_{\nu\uparrow}\gamma_{\nu\downarrow}\right\rangle = 0, \tag{7}$$

where f_ν is the Fermi–Dirac distribution of bogolons with the quasiparticle energy ε_ν. The quantum number ν enumerates the quasiparticle states in ascending energy order. In our study, we employ the open-boundary conditions [5,8,22] for the quasiparticle wavefunctions $u_\nu(i)$ and $v_\nu(i)$, which corresponds to the physical scenario of electrons being quantum-confined within the chain.

When using Equation 5 and Equation 7, the self-consistency relations given by Equation 4 are represented in the form

$$\begin{aligned}\Delta(i) &= g\sum_\nu u_\nu(i) v^*_\nu(i)\left[1-2f_\nu\right],\\ U_{\mathrm{HF}}(i) &= -g\sum_\nu\left[\left|u_\nu(i)\right|^2 f_\nu + \left|v_\nu(i)\right|^2\left(1-f_\nu\right)\right].\end{aligned} \tag{8}$$

In addition, the averaged occupation number of electrons is given by

$$n_{\mathrm{e}} = \frac{1}{N}\sum_{i\sigma}\left\langle \hat{n}_{i\sigma}\right\rangle = 2\sum_{i\nu}\left[f_\nu\left|u_\nu(i)\right|^2 + \left(1-f_\nu\right)\left|v_\nu(i)\right|^2\right], \tag{9}$$

which defines the chemical potential μ. The summation in Equation 8 and Equation 9 is over the quasiparticle species with positive energies. In addition, the summation in $\Delta(i)$ is limited to the states in the Debye window around the Fermi level, that is, $0 \le \varepsilon_\nu \le \hbar\omega_{\mathrm{D}}$. However, in the current study, we assume that $\hbar\omega_{\mathrm{D}}$ is much larger than the half-bandwidth. This assumption renders the Debye energy constraint ineffective as all solutions of the Bogoliubov–de Gennes (BdG) equations with positive quasiparticle energies consequently fall within the Debye window.

The self-consistent calculation procedure follows the same protocol as for the periodic Hubbard model. First, we solve the BdG equations (Equation 6) using an initial guess for μ, $\Delta(i)$, and $U_{\mathrm{HF}}(i)$. Second, using the resulting quasiparticle energies and wave functions, we compute new values for $\Delta(i)$ and $U_{\mathrm{HF}}(i)$ from Equation 8. Third, we adjust μ to achieve the desired average occupation number n_{e} from Equation 9. The new values of μ, $\Delta(i)$, and $U_{\mathrm{HF}}(i)$ are then reinserted into the BdG equations, and the entire procedure is repeated until convergence is achieved. The calculation is considered converged when the relative changes in the order parameter and the HF field are below 10^{-7}.

To model quasicrystal superconducting properties, as the first step, we consider a finite Fibonacci sequence (Fibonacci approximant) S_n, with n being the characteristic sequence number [15]. This is a sequence of symbols “A” and “B”, which is the concatenation of sequences S_{n-1} and S_{n-2}, that is, $S_n = [S_{n-1}, S_{n-2}]$, where S_1 = [B] and S_2 = [A] include only one symbol [15]. Based on this Fibonacci rule, we have S_3 = [AB], S_4 = [ABA], S_5 = [ABAAB], S_6 = [ABAABABA] and so on. The number of symbols in S_n is F_n, and $\{F_1, F_2, F_3, F_4, F_5,\ldots\} = \{1, 1, 2, 3, 5,\ldots\}$, which are the Fibonacci numbers. We then map this sequence onto a physical lattice using the off-diagonal model. Each symbol A or B in the sequence defines the hopping parameters t_{A} or t_{B}, respectively, between adjacent lattice sites. This results in a one-dimensional chain with a total of $N = F_n + 1$ sites, following the well-established off-diagonal formulation of the Fibonacci model [15,19,24,25].

All energy-related quantities, that is, $\Delta(i)$, $U_{\mathrm{HF}}(i)$, μ, T, t_{A}, and g, are expressed in units of the hopping parameter t_{B}. We set $g = 2$ and consider two different values of the Fibonacci sequence index, $n = 12$ and $n = 13$, for a more detailed illustration. Furthermore, we investigate two variants of the hopping amplitudes, namely, $t_{\mathrm{A}} = 0.5$ and $t_{\mathrm{A}} = 1.5$ (in units of t_{B}). Our calculations are performed away from the half-filling as this regime was shown to produce a uniform electronic distribution in Fibonacci chains [22], where the HF potential does not alter superconducting properties. Here, we adopt an electron density of $n_{\mathrm{e}} = 0.5$. Our qualitative conclusions are robust and not sensitive to the specific choice of these model parameters.

Results and Discussion

Figure 1 shows results of numerically solving the BdG equations in a self-consistent manner for $n = 12$ and $t_{\mathrm{A}} = 1.5$. In this case, $F_{n=12} = 233$; consequently, the number of atomic sites in

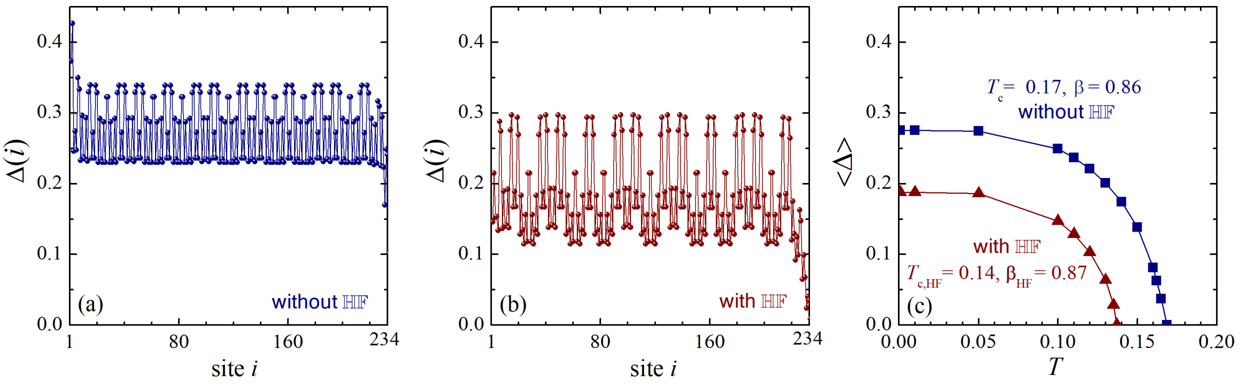

Figure 1: The spatial distribution of the order parameter in the Fibonacci chain with $n = 12$ and $t_A = 1.5$, without the HF potential (a) and with the HF potential (b). Panel (c) represents the temperature-dependence of the average order parameter in the chain center with (triangles) and without (squares) HF interaction. The critical temperatures with and without HF interaction are $T_{c,\mathrm{HF}} = 0.14$ and $T_c = 0.17$; the corresponding critical exponents of the averaged order parameter are $\beta_{\mathrm{HF}} = 0.87$ (with HF) and $\beta = 0.86$ (without HF).

the chain is $N = 234$. In Figure 1a, one can see the spatial profile of the order parameter $\Delta(i)$ calculated at zero temperature by taking into account the HF interaction. The order parameter exhibits significant oscillations due to the quasiperiodic character of the system. These oscillations in the Fibonacci approximant with $n = 12$ are connected with the fractal distribution of the condensate in the infinite Fibonacci chain. In agreement with a previous investigation [22], there are three spatial regions with clearly different averages of the order parameter, namely, the left-end domain, the center of the chain, and the right-end region. The order parameter is enhanced up to 0.43 near the left end, while it is reduced to 0.16 near the right end. The average value of $\Delta(i)$ near the chain center (averaging in the interval from $i = 70$ to $i = 170$) is 0.28. This feature is related to the presence of three critical temperatures, that is, the left-end, the right-end, and the center (bulk) superconducting temperature, as reported in [22].

We now examine the zero-temperature order parameter for the system with the HF potential, as shown in Figure 1b. The oscillations of the order parameter are immediately apparent and are significantly more pronounced than in the system without the HF potential. In Figure 1a, the total range of the oscillations (from their minimum to their maximum in a given region) is approximately 30% of the average order parameter value, whereas in Figure 1b, this value reaches nearly 100%. Furthermore, including the HF interaction qualitatively alters the spatial distribution of the condensate near the chain edges. Specifically, the enhancement of the order parameter near the left end, which is clearly present without the HF potential, is suppressed when the HF interaction is included, as seen in Figure 1b. Concurrently, the suppression of the order parameter near the right chain end becomes even more pronounced in the system with HF interaction.

To further analyze the system, Figure 1c shows the temperature-dependence of the order parameter averaged over the center of the chain, $\langle\Delta\rangle$ (in the interval from $i = 80$ to $i = 160$). The inclusion of HF interaction results in a significant decrease of both the order parameter in the chain center and the corresponding critical temperature. When the HF potential is included, the zero-temperature order parameter is $\langle\Delta\rangle_{T=0,\mathrm{HF}} = 0.19$, compared to a value of approximately 0.28 without it. The critical temperatures are $T_c = 0.17$ and $T_{c,\mathrm{HF}} = 0.14$. The ratio $\langle\Delta\rangle_{T=0,\mathrm{HF}}/T_{c,\mathrm{HF}} = 1.36$ is notably smaller than the corresponding ratio without the HF field, $\langle\Delta\rangle_{T=0}/T_c = 1.64$. Furthermore, both values are smaller than the universal BCS prediction of $\Delta(0)/T_c = 1.76$.

Finally, using the temperature-dependent data from Figure 1c, we calculate the critical exponent β of the order parameter near the critical temperature:

$$\langle\Delta\rangle \propto \tau^{\beta}, \tag{10}$$

where $\tau = 1 - T/T_c$ (or $T_{c,\mathrm{HF}}$ for the chain with the HF interaction). Our analysis shows that $\beta = 0.86$ without the HF field, while $\beta_{\mathrm{HF}} = 0.87$ with it. These values are only slightly different. However, both of them are significantly larger than the BCS order-parameter critical exponent of 0.5. This observation agrees with previous expectations [26,27] of power-law scaling with non-standard exponents for thermodynamic properties of superconducting quasicrystals near T_c. Here, we note an early investigation of another quasiperiodic one-dimensional quantum system, namely, the Ising model on a transverse applied field, which studied the phase transition occurring in its coupling parameter and related critical indexes [28].

For a further illustration, we consider a numerical solution of the BdG equations for a different parametric set, that is, for $n = 13$ and $t_A = 0.5$ (all other microscopic parameters are the same). In this case $F_{n=13} = 377$ and $N = 378$. The corresponding results are shown in Figure 2. This figure shows the order-parameter spatial distribution without (Figure 2a) and with HF interaction (Figure 2b), calculated for zero temperature. Similarly to the previous case, one observes significant oscillations of the order parameter, and these oscillations are notably enhanced when including HF interaction. The maximal difference between the order-parameter minima and maxima in Figure 2a is about 20% of the spatially averaged order parameter. In Figure 2b this values becomes about 60%.

However, despite a significant enhancement of the spatial oscillations of the order parameter in the presence of the HF interaction, its spatially averaged value (in the interval from $i = 140$ to $i = 240$) does not exhibit a significant drop and is reduced by less than 10%. An even smaller difference is observed between the two critical temperatures, $T_c = 0.304$ and $T_{c,HF} = 0.301$. In addition, for the present case, we have $\langle\Delta\rangle_{T=0,HF}/T_{c,HF} = 1.82$, which is larger than the corresponding ratio without the HF field, $\langle\Delta\rangle_{T=0}/T_c = 1.67$. In this case, the BCS value of the ratio between the zero-temperature order parameter and the critical temperature is 1.76, that is, between the two values calculated for the Fibonacci approximant. Finally, the critical order-parameter exponents for the system with HF interaction, $\beta_{HF} = 0.57$, and without HF interaction, $\beta = 0.65$, are still larger than the corresponding BCS value of 0.5; yet, this difference is less pronounced than for the previous parametric choice.

Conclusion

Based on a numerical solution of the BdG equations for superconducting Fibonacci chains, we demonstrate that including the HF interaction significantly enhances the spatial oscillations of the order parameter when the averaged electron density is beyond the half-filling regime. These oscillations are a direct consequence of the system's quasiperiodicity, reflecting a general feature of superconducting quasicrystals. The enhancement of these oscillations leads to a reduction of the critical temperature, which can be pronounced depending on the model's microscopic parameters. We also find that the critical exponent β of the order parameter differs significantly from that of a uniform BCS condensate. Moreover, the value of β changes when the HF interaction is included. Finally, the ratio between the zero-temperature order parameter and the critical temperature is also sensitive to the HF potential and deviates notably from the universal BCS value. Consequently, a rigorous analysis of the condensate distribution in quasicrystalline superconductors requires a direct comparison of results with and without HF interaction.

Finally, we remark that our results are obtained in the regime beyond the half-filling. The half-filling is the special regime with uniform density of electrons so that the HF field appears to be just a shift of the chemical potential, not altering other thermodynamic quantities, see the discussion in [22].

Funding

This work was supported by the project "International academic cooperation" of HSE University.

Author Contributions

Edward G. Nikonov: data curation; investigation; software; validation; visualization. Yajiang Chen: conceptualization; software. Mauro M. Doria: investigation; writing – review & editing. Arkady A. Shanenko: conceptualization; investigation;

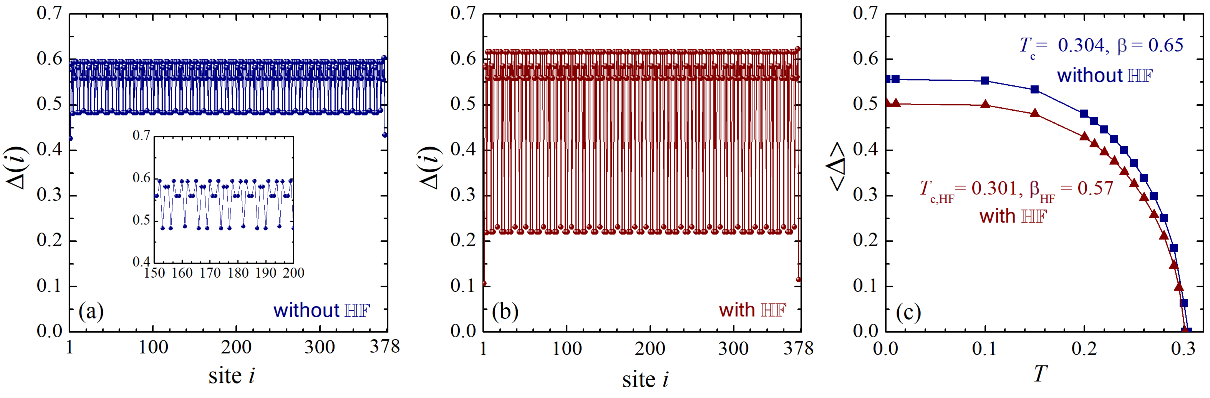

Figure 2: The same as in Figure 1 but for the Fibonacci chain with $n = 13$ and $t_A = 0.5$. Here, the critical temperatures of the systems with and without HF interaction are only slightly different: $T_c = 0.304$ and $T_{c,HF} = 0.301$. However, the order-parameter critical exponent for the case with the HF potential, $\beta_{HF} = 0.57$, is notably smaller than the value of $\beta = 0.65$ for the chain without the HF interaction.

project administration; writing – original draft; writing – review & editing.

ORCID® iDs

Edward G. Nikonov - https://orcid.org/0000-0001-7162-0344
Yajiang Chen - https://orcid.org/0000-0003-1442-4448
Mauro M. Doria - https://orcid.org/0000-0001-7207-7697
Arkady A. Shanenko - https://orcid.org/0000-0002-6031-5106

Data Availability Statement

Data generated and analyzed during this study is available from the corresponding author upon reasonable request.

Preprint

A non-peer-reviewed version of this article has been previously published as a preprint: https://doi.org/10.3762/bxiv.2025.60.v1

References

1. De Gennes, P. G. *Superconductivity of metals and alloys;* W. A. Benjamin: New York, NY, USA, 1966.
2. Bardeen, J.; Cooper, L. N.; Schrieffer, J. R. *Phys. Rev.* **1957,** *108,* 1175–1204. doi:10.1103/physrev.108.1175
3. Ketterson, J. B.; Song, S. N. *Superconductivity;* Cambridge University Press: Cambridge, UK, 1999.
4. Zhu, J.-X. *Bogoliubov-de Gennes Method and Its Applications,* 1st ed.; Lecture notes in physics; Springer International Publishing: Cham, Switzerland, 2016. doi:10.1007/978-3-319-31314-6
5. Tanaka, K.; Marsiglio, F. *Phys. Rev. B* **2000,** *62,* 5345–5348. doi:10.1103/physrevb.62.5345
6. Ghosal, A.; Randeria, M.; Trivedi, N. *Phys. Rev. B* **2001,** *65,* 014501. doi:10.1103/physrevb.65.014501
7. Chen, Y.; Croitoru, M. D.; Shanenko, A. A.; Peeters, F. M. *J. Phys.: Condens. Matter* **2009,** *21,* 435701. doi:10.1088/0953-8984/21/43/435701
8. Chen, Y.; Zhu, Q.; Zhang, M.; Luo, X.; Shanenko, A. A. *Phys. Lett. A* **2024,** *494,* 129281. doi:10.1016/j.physleta.2023.129281
9. Shechtman, D.; Blech, I.; Gratias, D.; Cahn, J. W. *Phys. Rev. Lett.* **1984,** *53,* 1951–1953. doi:10.1103/physrevlett.53.1951
10. Levine, D.; Steinhardt, P. J. *Phys. Rev. Lett.* **1984,** *53,* 2477–2480. doi:10.1103/physrevlett.53.2477
11. Senechal, M. *Quasicrystals and geometry;* Cambridge University Press: Cambridge, MA, USA, 1995.
12. Kamiya, K.; Takeuchi, T.; Kabeya, N.; Wada, N.; Ishimasa, T.; Ochiai, A.; Deguchi, K.; Imura, K.; Sato, N. K. *Nat. Commun.* **2018,** *9,* 154. doi:10.1038/s41467-017-02667-x
13. Tokumoto, Y.; Hamano, K.; Nakagawa, S.; Kamimura, Y.; Suzuki, S.; Tamura, R.; Edagawa, K. *Nat. Commun.* **2024,** *15,* 1529. doi:10.1038/s41467-024-45952-2
14. Meena, P. K.; Verma, R.; Arushi; Jangid, S.; Kushwaha, R. K.; Stewart, R.; Hillier, A. D.; Singh, B.; Singh, R. P. *Commun. Mater.* **2025,** *6,* 226. doi:10.1038/s43246-025-00949-2
15. Jagannathan, A. *Rev. Mod. Phys.* **2021,** *93,* 045001. doi:10.1103/revmodphys.93.045001
16. Rai, G.; Haas, S.; Jagannathan, A. *Phys. Rev. B* **2019,** *100,* 165121. doi:10.1103/physrevb.100.165121
17. Rai, G.; Haas, S.; Jagannathan, A. *Phys. Rev. B* **2020,** *102,* 134211. doi:10.1103/physrevb.102.134211
18. Rai, G.; Haas, S.; Jagannathan, A. *J. Phys.: Conf. Ser.* **2020,** *1458,* 012013. doi:10.1088/1742-6596/1458/1/012013
19. Sun, M.; Čadež, T.; Yurkevich, I.; Andreanov, A. *Phys. Rev. B* **2024,** *109,* 134504. doi:10.1103/physrevb.109.134504
20. Sandberg, A.; Awoga, O. A.; Black-Schaffer, A. M.; Holmvall, P. *Phys. Rev. B* **2024,** *110,* 104513. doi:10.1103/physrevb.110.104513
21. Kobiałka, A.; Awoga, O. A.; Leijnse, M.; Domański, T.; Holmvall, P.; Black-Schaffer, A. M. *Phys. Rev. B* **2024,** *110,* 134508. doi:10.1103/physrevb.110.134508
22. Zhu, Q.; Zha, G.-Q.; Shanenko, A. A.; Chen, Y. *Phys. Rev. B* **2025,** *112,* 134503. doi:10.1103/j8tj-82ty
23. Nagai, Y. *Phys. Rev. B* **2022,** *106,* 064506. doi:10.1103/physrevb.106.064506
24. Piéchon, F.; Benakli, M.; Jagannathan, A. *Phys. Rev. Lett.* **1995,** *74,* 5248–5251. doi:10.1103/physrevlett.74.5248
25. Rüdinger, A.; Piéchon, F. *J. Phys. A: Math. Gen.* **1998,** *31,* 155–164. doi:10.1088/0305-4470/31/1/017
26. Karkut, M. G.; Triscone, J.-M.; Ariosa, D.; Fischer, Ø. *Phys. Rev. B* **1986,** *34,* 4390–4393. doi:10.1103/physrevb.34.4390
27. Kitaev, A. Y.; Levitov, L. S. *Sov. Phys. - JETP* **1989,** *68,* 176–181.
28. Doria, M. M.; Satija, I. I. *Phys. Rev. Lett.* **1988,** *60,* 444–447. doi:10.1103/physrevlett.60.444

License and Terms

BEILSTEIN JOURNAL OF NANOTECHNOLOGY

Electromagnetic study of a split-ring resonator metamaterial with cold-electron bolometers

Ekaterina A. Matrozova[1], Alexander V. Chiginev[1,2], Leonid S. Revin[1,2] and Andrey L. Pankratov*[1,2]

Full Research Paper

Open Access

Address:
[1]Nizhny Novgorod State Technical University n.a. R.E. Alekseev, MininStreet, 24, Nizhny Novgorod, 603155, Russia and [2]Institute for Physics of Microstructures of the Russian Academy of Sciences, Akademicheskaya Street, 7, Nizhny Novgorod, 603950, Russia

Email:
Andrey L. Pankratov* - alp@ipmras.ru

* Corresponding author

Keywords:
cold-electron bolometer; metamaterial; split-ring resonator

Beilstein J. Nanotechnol. **2025,** *16,* 2199–2206.
https://doi.org/10.3762/bjnano.16.152

Received: 02 October 2025
Accepted: 18 November 2025
Published: 05 December 2025

This article is part of the thematic issue "Superconducting artificial neural networks and quantum circuits".

Guest Editor: A. S. Sidorenko

Abstract

We present an electromagnetic study of a metamaterial receiver based on split-ring resonators with integrated cold-electron bolometers. We suggest a modified antenna design that allows one to significantly increase the absorbed power and the bandwidth. The trade-off between the bandwidth expansion due to miniaturization and the reduction in absorption efficiency determined by the Airy spot size of the coupling lens is investigated. To solve this issue, a simultaneous miniaturization of the size of the entire structure with an increase in the number of array elements is proposed. The design with a 37-element array demonstrates an increase in power absorption by a factor of 1.4 compared to the original 19-element single-ring array, as well as an increase in operating bandwidth from 160 to 820 GHz.

Introduction

Highly sensitive receivers with broadband antennas are of significant interest for advanced spectroscopic applications and various radioastronomy tasks [1-5]. In particular, broadband receiving systems are required for use with a Fourier-transform spectrometer based on the Martin–Paplett interferometer that is planned to be used in future missions such as BISOU (Balloon Interferometer for Spectral Observations of the Universe) [3,4] and Millimetron [2,5]. The use of cold-electron bolometers (CEBs) is particularly advantageous for such systems, enabling operation in a wide frequency range from gigahertz frequencies to X-rays [6-8] due to a normal-metal absorber. CEBs offer several advantages over other types of receivers such as transition edge sensors [9-11]. These advantages include their micrometer-scale size, which facilitates direct integration into antenna slots without the need for microwave feed lines (e.g., microstrip or coplanar lines), thus simplifying the design and preventing signal degradation at higher frequencies [12]. Furthermore, the natural electron cooling mechanism in CEBs [13-15] is highly suitable for operation with cryogenic systems such as ^{3}He sorption fridges. Perhaps most critically, CEBs demonstrate exceptional hardness against cosmic rays [16], a paramount requirement for balloon and space missions.

Our group has recently designed, fabricated, and characterized a metamaterial receiver with integrated CEBs, operating in a broad frequency range [17]. In that work, each element represented a ring antenna with two embedded CEBs connected parallel in DC, whereas the antennas in the array were connected in series. In the present work, we propose and numerically investigate a new design of a CEB metamaterial receiver based on double split-ring resonators (SRRs) [18] to increase both the magnitude of the absorbed signal and the working bandwidth. We consider various geometrical modifications of this design and perform a comparative analysis.

Design and Simulation Approach

In our previous work [17], a metamaterial comprising 19-ring antennas enabled the reception of external electromagnetic signals in the broad band from 150 to 550 GHz, as well as in the band from 900 to 1300 GHz. To further enhance signal absorption, we propose replacing simple ring antennas with SRRs [18-21]. The SRR is a well-established magnetic metamaterial element whose resonant properties are governed by its internal inductance and capacitance, allowing for a strong magnetic response and associated current loops at the designed resonance frequency.

The simulations of the metamaterial arrays were performed in the time-domain solver of CST MWS in 3D mode. The simulated receiving structure is placed on a 500 µm thick silicon substrate. A 4 mm-diameter silicon hyperhemispherical lens is placed on the rear side of the substrate to efficiently couple the incident radiation into the planar structure. The external signal is incident from the H_{11} mode of the round waveguide port located behind the Si lens, simulating a realistic excitation source. The electric field of the incident wave is directed perpendicularly to the gaps in the receiving elements.

The signal is received by an array of the proposed ring resonators. Two CEBs are embedded into the outer ring of each SRR element. In the simulations, each CEB is modeled as an RC circuit (see inset in Figure 1), where R_{abs} = 75 Ω represents the resistance of the CEB's normal-metal absorber, and C_{SIN} = 20 fF is the capacitance of the two SIN junctions of the CEB connected in series. The total absorbed power is calculated as the sum of the powers absorbed in these discrete ports repre-

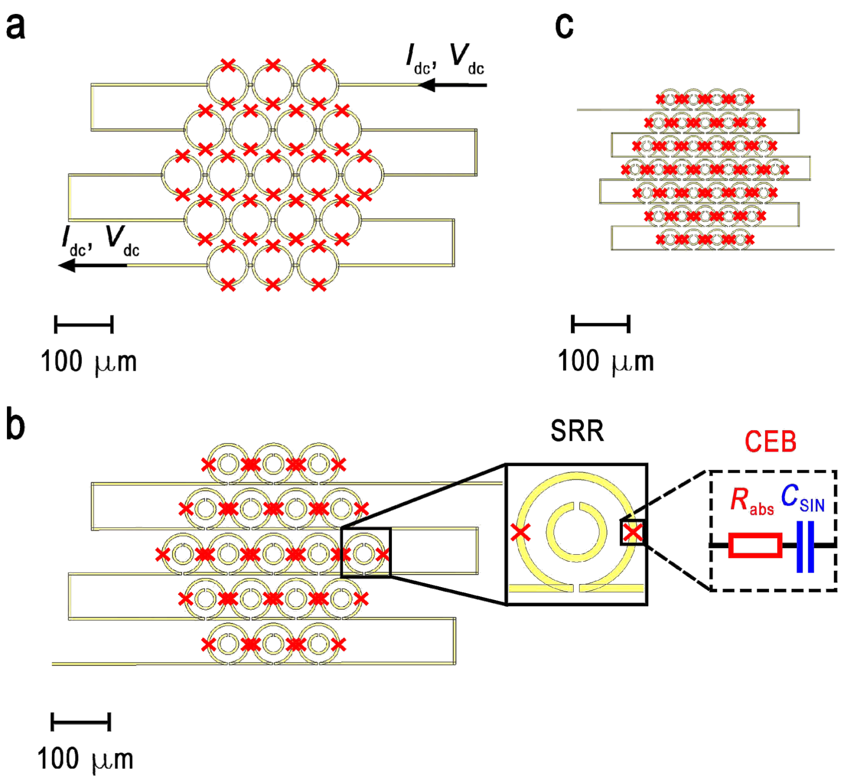

Figure 1: Schematic layout of the investigated metamaterial arrays. (a) 19-element array of single-ring antennas; (b) 19-element array of split-ring resonators; (c) 37-element array of miniaturized SRRs. Inset: a single unit cell with two embedded CEBs represented as an RC circuit.

senting the CEBs. The power in our modeling is normalized to the power outgoing from the waveguide port, which is equal to 0.5 in arbitrary units.

Results

The design of the previously studied metamaterial with CEBs and single-ring antennas is shown in Figure 1a. To increase the absorbed power and the working frequency band, we propose and analyze a new design based on SRRs (Figure 1b,c). The geometric parameters of the structures are as follows: A single ring has an outer ring diameter of d_{ext} = 80 µm and an inner ring diameter of d_{int} = 70 µm. The lattice constant (period) of the metamaterial array is P = 86 µm. The total size of the structure is 424 µm. A large-scale SRR has an outer ring with an external diameter of $d_{\text{ext},1}$ = 80 µm and an internal diameter of $d_{\text{int},1}$ = 70 µm. The inner ring has an external diameter of $d_{\text{ext},2}$ = 40 µm and an internal diameter of $d_{\text{int},2}$ = 30 µm. The period of the metamaterial array is P = 86 µm. The total size of the structure is 424 µm. A small-scale SRR is a scaled-down version with $d_{\text{ext},1}$ = 40 µm, $d_{\text{int},1}$ = 35 µm; $d_{\text{ext},2}$ = 20 µm, $d_{\text{int},2}$ = 15 µm. The lattice period for this dense array is P = 43 µm. The total size of the structure is reduced to 298 µm. This scaling of the SRR geometry is intended to shift the central frequency of the metamaterial to a higher value while maintaining the increasing absorption of the double-ring design.

The transition from a single-ring antenna to a double split-ring resonator design, while keeping the number of elements constant, resulted in a significant improvement in performance. The addition of the inner ring, which increases the total capacitance of the resonant element, leads to a slight reduction of the central frequency [20]. More importantly, it yielded a 1.5-fold increase in the total absorbed power.

The amplitude–frequency characteristics (AFC) for the simulated single-ring and SRR designs are presented in Figure 2. For the single-ring array, the absorbed power in the first resonance maximum reached a value of 0.18 (normalized units, with 0.5 maximal total power) with the bandwidth at half maximum (FWHM) spanning from 100 to 545 GHz (Figure 2, red curve). In contrast, the SRR array demonstrated a higher absorbed power of 0.27 within a bandwidth of 105 to 440 GHz (Figure 2, blue curve). Parameters of metamaterials with CEBs and different designs are given in Table 1.

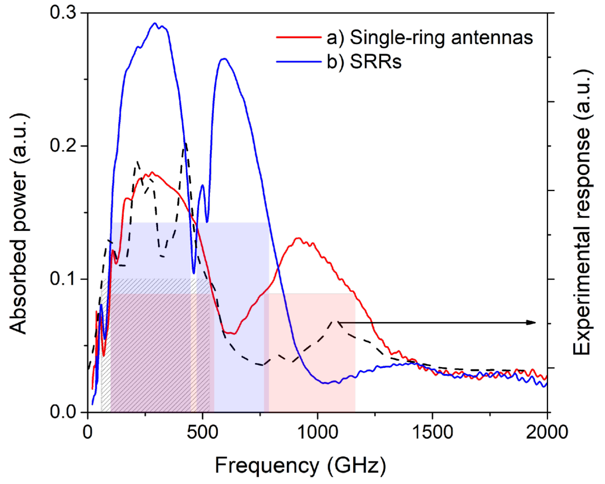

Figure 2: Amplitude–frequency characteristics of the metamaterial receiver. (a) 19-element array of single-ring antennas with a lattice period of P = 86 µm (red curve); (b) 19-element array of SRRs with P = 86 µm (blue curve). The dashed black curve shows the experimentally measured response of the single-ring metamaterial.

As an experimental reference for our simulations, Figure 2 also shows the frequency response measured for a fabricated sample consisting of a 19-element single-ring metamaterial (black dashed curve). This sample had the design described in [17] and was characterized using the same experimental setup described there. This setup employs a YBaCuO Josephson junction oscillator as a broadband source, with the signal delivered to the sample via an oversized waveguide. Therefore, the measured frequency response is the combined frequency response of the entire path (oscillator, waveguide-feeder, lens and the CEB metamaterial itself), with “fingers” due to the used log-periodic antenna of the Josephson oscillator, which was not fully matched to the antenna. Despite this convolution, the experimental data clearly confirm the calculated dual-band behavior of the metamaterial, showing two broad peaks centered at approximately 350 and 1100 GHz. This agreement validates our simulation model.

Table 1: Parameters of metamaterial structures with CEBs.

Design (according to Figure 1)	Type of unit cell	Number of cells	Period of structure, µm	Peak absorption, a.u.	Frequency band, GHz
a	single-ring antennas	19	86	0.18	100–545
b	split-ring resonators	19	86	0.27	105–440
c	split-ring resonators	37	43	0.25	160–820

The AFC of the single-ring and SRR metamaterials with various scaling factors are presented in Figure 3. The optimal number and size of the resonators are governed by the requirement to fill the Airy spot of the silicon lens. If the total array size is smaller than the Airy spot, a portion of the incident signal will not interact with the metamaterial, instead scattering into the surrounding space. Our simulations confirm this principle: A reduction in the SRR dimensions and the array period by 20% led to a broadening of the absorption bandwidth and a small shift of the first resonance maximum towards higher frequencies. A further reduction of dimensions by 40% resulted in an even wider bandwidth; however, the peak absorbed power began decreasing, indicating that the array size was becoming insufficient relative to the Airy spot. A drastic 60% size reduction caused a severe deterioration of absorption.

To achieve the widest possible bandwidth using SRRs, our results shown in Figure 3 suggest prioritizing somewhat smaller unit cell sizes. Simply scaling down a fixed 19-element array leads to less efficient signal reception since the array is becoming smaller than the Airy spot. As an efficient alternative, we propose to halve the SRR dimensions and array period while simultaneously increasing the number of elements from 19 to 37 (Figure 1c). This approach successfully increased the absorbed power to 0.25, which is by a factor of 1.4 higher than that of the single-ring array, while also achieving an ultrawide receiving band from 160 to 820 GHz (Figure 4, black line). If the 37-element array structure occupies the same area as the original single-ring structure, larger absorption efficiency at the first peak can be achieved (Figure 4, red line), but the working bandwidth will be narrower than for the structure with smaller

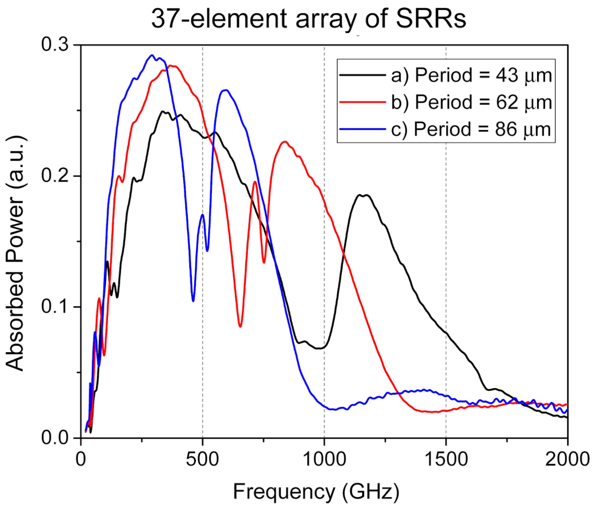

Figure 4: The amplitude–frequency characteristics of the 37-element array of SRR-based metamaterial for different periods of the lattice.

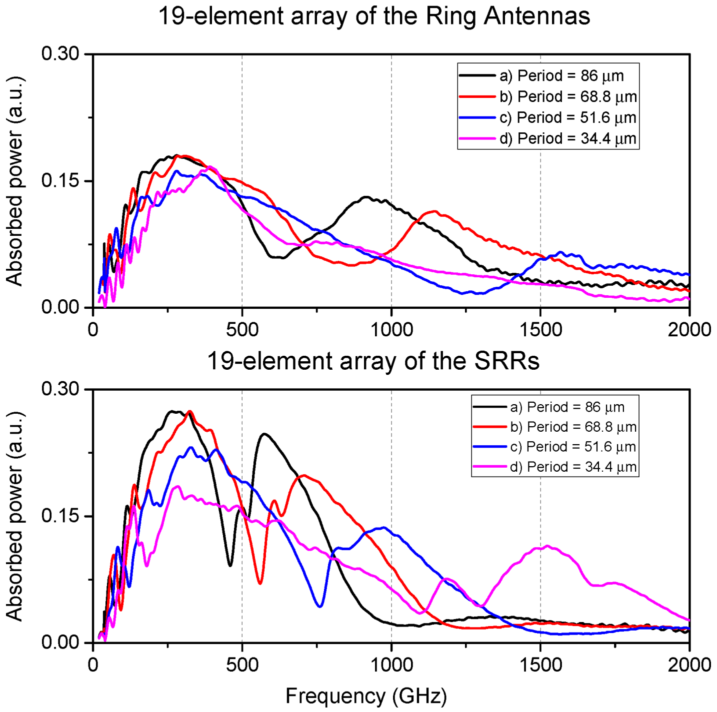

Figure 3: Top: AFC of the 19 single-ring antenna metamaterial for different geometric scaling factors. (a, black curve) outer ring diameter d_{out} = 80 µm, inner ring diameter d_{in} = 70 µm, period P = 86 µm; (b, red curve) d_{out} = 64 µm, d_{in} = 56 µm, P = 68.8 µm; (c, blue curve) d_{out} = 48 µm, d_{in} = 42 µm, P = 51.6 µm; (d, purple curve) d_{out} = 32 µm, d_{in} = 28 µm, P = 34.4 µm. Bottom: AFC of the 19 SRR-based metamaterial for different geometric scaling factors. The design parameters and scaling factors (0%, 20%, 40%, and 60%) correspond to the upper plot.

rings. Thus, by selecting the overall structure size, a compromise can be found between the maximum absorption efficiency and the widest receiving bandwidth.

It is important to note that the choice of the number of receiving antennas should be in a proper balance. Although a larger array can better fill the Airy spot, it also increases the total number of bolometers. This, in turn, increases the differential resistance of the structure at the operating point and increases the current noise contribution of the readout amplifier [17,22]. Furthermore, a larger number of elements increases the fabrication complexity. Crucially, nearly doubling the number of elements (from 19 to 37) does not produce a proportional increase in the absorbed power (Figure 5).

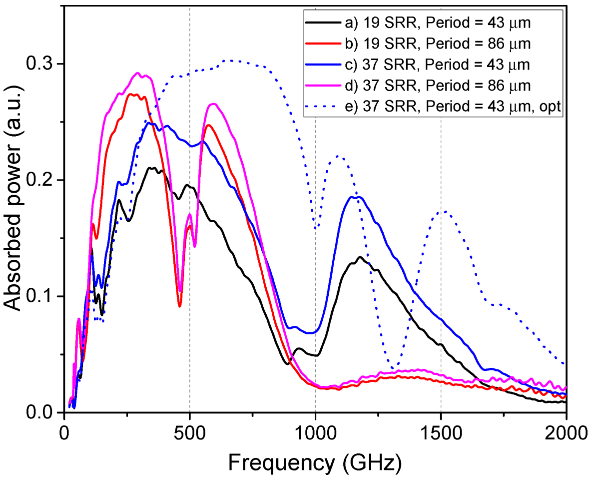

Figure 5: Dependence of the absorbed power on the number of elements in the SRR array.

Figure 5 shows the AFC of the SRR metamaterial with a different number of elements. For the large-scale design (period P = 86 μm, rings: $d_{\text{out},1}/d_{\text{in},1}$ = 80/70 μm, $d_{\text{out},2}/d_{\text{in},2}$ = 40/30 μm), doubling the number of elements increases the absorbed power by about 7% only, with a minor increase in bandwidth. The same doubling for the miniaturized design (P = 43 μm, rings: $d_{\text{out},1}/d_{\text{in},1}$ = 40/35 μm, $d_{\text{out},2}/d_{\text{in},2}$ = 20/15 μm) is more efficient, leading to 17% increase in power. This higher efficiency is directly linked to the Airy spot coverage: Adding elements to the smaller array more effectively increases its total area towards the optimal size. For the already large array, new elements are added at the periphery or outside the most intense part of the Airy spot, which does not actually help.

The obtained results can be further enhanced through optimized design parameters of the structure. Specifically, increasing the substrate thickness to 700 μm enables an increase in absorbed power up to 0.3 a.u. across an ultrabroad frequency range of 200–1200 GHz (Figure 5e). Such a thick substrate can be realized by using commercially available substrates with greater thickness (or by stacking and bonding multiple thinner substrates), or by employing a lens with a pedestal structure.

Discussion

Solving the problem of broadband high-sensitivity reception for terahertz applications naturally entails comparing the metamaterial-based approach presented here with traditional broadband antenna solutions such as the log-periodic [23-25] or spiral antennas [26,27]. These antennas are indeed a well-established technology, providing wideband frequency response and high detection/radiation efficiency. However, their widespread use is subject to a fundamental limitation: The active receiving element is typically a single detector unit located at the antenna's feed point. This configuration can become a bottleneck when detecting ultralow power signals in the presence of high background radiation, as the single detector must handle the entire power load, potentially limiting the dynamic range and complicating the optimization of noise-equivalent power (NEP).

There have been proposals to integrate multiple sensing elements directly into the structure of a log-periodic antenna [28-30]. While promising, such designs face significant challenges in implementation. The complex geometry of the antenna makes it difficult to integrate a large number of detectors and to design complex series–parallel electrical networks necessary for optimal power distribution and impedance matching. In contrast, the metamaterial approach offers a fundamentally more flexible paradigm. A periodic array of resonators, such as our SRR-based design, inherently functions as a multiabsorber system. This architecture allows for the precise engineering of the detector network, that is, the number of CEBs, their individual connection (series or parallel), and the overall array configuration to achieve an optimal balance between power load, responsivity, and total noise [17,22].

This capability is particularly critical for applications like cosmic microwave background polarimetry or high-resolution spectroscopy, where the detector must operate photon-noise-limited under a specific background power load. For CEBs, we have previously demonstrated that the optimal configuration for minimizing the total NEP with a given readout amplifier involves a specific series–parallel combination of bolometers. The metamaterial platform is ideal for implementing such an optimized multiabsorber receiver. By adapting the array geometry and the electrical connection scheme between CEBs, one can precisely control the power absorbed per bolometer and the resulting differential resistance, thereby achieving photon-noise-limited performance across a wide bandwidth. This level of design control is considerably more challenging to realize within the constrained geometry of a single-feed log-periodic antenna.

Conclusion

In this work, we have presented a comprehensive electromagnetic study on the design and optimization of a metamaterial receiver based on split-ring resonators integrated with cold-electron bolometers. The transition from a conventional single-ring antenna design to a double SRR configuration has been demonstrated to be a highly efficient strategy to enhance the receiver performance. This design improvement resulted in a substantial 1.5-fold increase in the absorbed power, confirming the theoretical advantage of SRRs in providing a stronger magnetic resonance and greater field concentration within the capacitive gaps where the CEBs are located.

Our investigation of the scaling of the metamaterial array revealed a critical design trade-off. While reducing the dimensions of the SRR unit cells effectively broadens the operational bandwidth, it also reduces the total absorbed power if the array's physical size becomes smaller than the Airy spot of the coupling lens. We successfully resolved this issue by implementing a strategy of simultaneous miniaturization and increasing the array density. By halving the SRR dimensions and lattice period while nearly doubling the number of elements (from 19 to 37), we achieved an optimal compromise. The resulting receiver exhibits both enhanced absorption (by a factor of 1.4 larger than the original single-ring design) and an ultrawide bandwidth spanning from 160 to 820 GHz.

Furthermore, we quantified the non-linear relationship between the number of array elements and the absorbed power, showing that the benefit of adding elements is significantly higher for a miniaturized array that initially underfills the Airy spot. This provides a crucial practical guideline for designing efficient multiabsorber receivers, balancing performance gains against the increased technological complexity and noise considerations associated with a larger number of bolometers.

This work solidifies the position of CEB-based SRR metamaterials as a highly promising platform for constructing ultrabroadband, high-sensitivity receivers essential for next-generation spectroscopic and radioastronomical applications, particularly in demanding space and balloon-borne environments. One more important potential application for such broadband receiving system is the use for axion search experiments with broadband coaxial dish antennas [31,32]. Future work will focus on the experimental fabrication and characterization of the proposed miniaturized 37-element SRR array to validate these simulation results.

Funding

The work is supported by Russian Science Foundation Grant No. 21-79-20227.

Author Contributions

Ekaterina A. Matrozova: data curation; formal analysis; investigation; methodology; software; visualization; writing – original draft; writing – review & editing. Alexander V. Chiginev: conceptualization; data curation; formal analysis; investigation; methodology; software; validation; writing – original draft; writing – review & editing. Leonid S. Revin: conceptualization; formal analysis; investigation; methodology; software; validation; visualization; writing – original draft; writing – review & editing. Andrey L. Pankratov: conceptualization; formal analysis; funding acquisition; investigation; methodology; project administration; resources; supervision; validation; writing – review & editing.

ORCID® iDs

Ekaterina A. Matrozova - https://orcid.org/0000-0003-1013-1365
Alexander V. Chiginev - https://orcid.org/0000-0002-6676-9141
Andrey L. Pankratov - https://orcid.org/0000-0003-2661-2745

Data Availability Statement

Data generated and analyzed during this study is available from the corresponding author upon reasonable request.

Preprint

A non-peer-reviewed version of this article has been previously published as a preprint: https://doi.org/10.3762/bxiv.2025.58.v1

References

1. Ajito, K.; Nakamura, M.; Tajima, T.; Ueno, Y. Terahertz Spectroscopy Methods and Instrumentation. In *Encyclopedia of Spectroscopy and Spectrometry,* 3rd ed.; Lindon, J. C.; Tranter, G. E.; Koppenaal, D. W., Eds.; Academic Press: Oxford, UK, 2017; pp 432–438. doi:10.1016/b978-0-12-409547-2.12092-x
2. Likhachev, S. F.; Larchenkova, T. I. *Phys.-Usp.* **2024,** *67,* 768–778. doi:10.3367/ufne.2024.03.039662
3. Maffei, B.; Aghanim, N.; Aumont, J.; Battistelli, E.; Beelen, A.; Besnard, A.; Borgo, B.; Calvo, M.; Catalano, A.; Chluba, J.; Coulon, X.; de Bernardis, P.; De Jabrun, C.; Douspis, M.; Errard, J.; Grain, J.; Guiot, P.; Hill, J. C.; Ishino, H.; Kogut, A.; Lagache, G.; Macias-Perez, J.; Masi, S.; Matsumura, T.; Monfardini, A.; O'Sullivan, C.; Pagano, L.; Patanchon, G.; Pisano, G.; Pitre, L.; Ponthieu, N.; Remazeilles, M.; Ritacco, A.; Savini, G.; Sauvage, V.; Shitvov, A.; Stever, S. L.; Tartari, A.; Thiele, L.; Trappe, N.; Aubrun, J.-F.; Bray, N.; Louvel, S. BISOU: a balloon pathfinder for CMB spectral distortions studies. In *Millimeter, Submillimeter, and Far-Infrared Detectors and Instrumentation for Astronomy XII,* Yokohama, Japan, June 18–22, 2024; Zmuidzinas, J.; Gao, J.-R., Eds.; SPIE, 2024; 131020N. doi:10.1117/12.3018371
4. Coulon, X.; Maffei, B.; Aghanim, N. *EPJ Web Conf.* **2024,** *293,* 00012. doi:10.1051/epjconf/202429300012

5. Novikov, D. I.; Doroshkevich, A. G.; Larchenkova, T. I.; Malinovsky, A. M.; Mihalchenko, A. O.; Osipova, A. M.; Parfenov, K. O.; Pilipenko, S. V. *Phys.-Usp.* **2025,** *68,* 987–1000. doi:10.3367/ufne.2025.08.040006
6. Anghel, D. V.; Kuzmin, L. S. *Phys. Rev. Appl.* **2020,** *13,* 024028. doi:10.1103/physrevapplied.13.024028
7. Pimanov, D. A.; Pankratov, A. L.; Gordeeva, A. V.; Chiginev, A. V.; Blagodatkin, A. V.; Revin, L. S.; Razov, S. A.; Safonova, V. Yu.; Fedotov, I. A.; Skorokhodov, E. V.; Orlova, A. N.; Tatarsky, D. A.; Gusev, N. S.; Trofimov, I. V.; Mumlyakov, A. M.; Tarkhov, M. A. *Supercond. Sci. Technol.* **2025,** *38,* 035026. doi:10.1088/1361-6668/adb942
8. Nahum, M.; Martinis, J. M. *Appl. Phys. Lett.* **1995,** *66,* 3203–3205. doi:10.1063/1.113723
9. Irwin, K. D.; Hilton, G. C. Transition-Edge Sensors. *Cryogenic Particle Detection;* Topics in Applied Physics, Vol. 99; Springer: Berlin, Germany, 2005; pp 63–150. doi:10.1007/10933596_3
10. Withington, S. *Contemp. Phys.* **2022,** *63,* 116–137. doi:10.1080/00107514.2023.2180179
11. Safonova, V. Y.; Gordeeva, A. V.; Blagodatkin, A. V.; Pimanov, D. A.; Yablokov, A. A.; Pankratov, A. L. *Beilstein J. Nanotechnol.* **2024,** *15,* 1353–1361. doi:10.3762/bjnano.15.108
12. O'Brient, R.; Ade, P.; Arnold, K.; Edwards, J.; Engargiola, G.; Holzapfel, W. L.; Lee, A. T.; Myers, M. J.; Quealy, E.; Rebeiz, G.; Richards, P.; Suzuki, A. *Appl. Phys. Lett.* **2013,** *102,* 063506. doi:10.1063/1.4791692
13. Gordeeva, A. V.; Pankratov, A. L.; Pugach, N. G.; Vasenko, A. S.; Zbrozhek, V. O.; Blagodatkin, A. V.; Pimanov, D. A.; Kuzmin, L. S. *Sci. Rep.* **2020,** *10,* 21961. doi:10.1038/s41598-020-78869-z
14. Pimanov, D. A.; Frost, V. A.; Blagodatkin, A. V.; Gordeeva, A. V.; Pankratov, A. L.; Kuzmin, L. S. *Beilstein J. Nanotechnol.* **2022,** *13,* 896–901. doi:10.3762/bjnano.13.80
15. Lemziakov, S. A.; Karimi, B.; Nakamura, S.; Lvov, D. S.; Upadhyay, R.; Satrya, C. D.; Chen, Z.-Y.; Subero, D.; Chang, Y.-C.; Wang, L. B.; Pekola, J. P. *J. Low Temp. Phys.* **2024,** *217,* 54–81. doi:10.1007/s10909-024-03144-8
16. Salatino, M.; de Bernardis, P.; Kuzmin, L. S.; Mahashabde, S.; Masi, S. *J. Low Temp. Phys.* **2014,** *176,* 323–330. doi:10.1007/s10909-013-1057-5
17. Revin, L. S.; Pimanov, D. A.; Pankratov, A. L.; Blagodatkin, A. V.; Matrozova, E. A.; Chiginev, A. V.; Gordeeva, A. V.; Fedotov, I. A.; Skorokhodov, E. V.; Gusev, N. S.; Masterov, D. V.; Parafin, A. E.; Sobolev, A. S. *Phys. Rev. Appl.* **2024,** *22,* 064040. doi:10.1103/physrevapplied.22.064040
18. Sydoruk, O.; Tatartschuk, E.; Shamonina, E.; Solymar, L. *J. Appl. Phys.* **2009,** *105,* 014903. doi:10.1063/1.3056052
19. Pendry, J. B.; Holden, A. J.; Robbins, D. J.; Stewart, W. J. *IEEE Trans. Microwave Theory Tech.* **1999,** *47,* 2075–2084. doi:10.1109/22.798002
20. Reddy, A. N.; Raghavan, S. Split ring resonator and its evolved structures over the past decade: This paper discusses the nuances of the most celebrated composite particle (split-ring resonator) with which novel artificial structured materials (called metamaterials) are built. In *2013 IEEE International Conference ON Emerging Trends in Computing, Communication and Nanotechnology (ICECCN),* Tirunelveli, India, March 25–26, 2013; IEEE, 2013; pp 625–629. doi:10.1109/ice-ccn.2013.6528575
21. Marqués, R.; Martín, F.; Sorolla, M. *Metamaterials with Negative Parameters: Theory, Design and Microwave Applications;* John Wiley & Sons: Hoboken, NJ, USA, 2008. doi:10.1002/9780470191736
22. Kuzmin, L. S.; Pankratov, A. L.; Gordeeva, A. V.; Zbrozhek, V. O.; Shamporov, V. A.; Revin, L. S.; Blagodatkin, A. V.; Masi, S.; de Bernardis, P. *Commun. Phys.* **2019,** *2,* 104. doi:10.1038/s42005-019-0206-9
23. Tarasov, M.; Kuzmin, L.; Stepantsov, E.; Kidiyarova-Shevchenko, A. Quasioptical Terahertz Spectrometer Based on a Josephson Oscillator and a Cold Electron Nanobolometer. *Nanoscale Devices - Fundamentals and Applications; NATO Science Series*, Vol. 233; Springer: Dordrecht, Netherlands, 2006; pp 325–335. doi:10.1007/978-1-4020-5107-4_22
24. Stepantsov, E.; Tarasov, M.; Kalabukhov, A.; Kuzmin, L.; Claeson, T. *J. Appl. Phys.* **2004,** *96,* 3357–3361. doi:10.1063/1.1782273
25. Gao, X.; Zhang, T.; Du, J.; Weily, A. R.; Guo, Y. J.; Foley, C. P. *Supercond. Sci. Technol.* **2017,** *30,* 095011. doi:10.1088/1361-6668/aa7cc1
26. Tretyakov, I. V.; Khudchenko, A. V.; Rudakov, K. I.; Ivashentseva, I. V.; Kaurova, N. S.; Voronov, B. M.; Kirsanova, M. S.; Larchenkova, T. I.; Goltsman, G. N.; Baryshev, A. M.; Hesper, R.; Khan, F. V.; Zhukova, E. S.; Chekushkin, A. M.; Melentev, A. V.; Zhivetev, K. V.; Terentiev, A. V.; Koshelets, V. P.; Likhachev, S. F. *IEEE Trans. Terahertz Sci. Technol.* **2025,** *15,* 191–199. doi:10.1109/tthz.2024.3505592
27. Malnou, M.; Luo, A.; Wolf, T.; Wang, Y.; Feuillet-Palma, C.; Ulysse, C.; Faini, G.; Febvre, P.; Sirena, M.; Lesueur, J.; Bergeal, N. *Appl. Phys. Lett.* **2012,** *101,* 233505. doi:10.1063/1.4769441
28. Yu, M.; Geng, H.; Hua, T.; An, D.; Xu, W.; Chen, Z. N.; Chen, J.; Wang, H.; Wu, P. *Supercond. Sci. Technol.* **2020,** *33,* 025001. doi:10.1088/1361-6668/ab5e13
29. Sharafiev, A.; Malnou, M.; Feuillet-Palma, C.; Ulysse, C.; Wolf, T.; Couëdo, F.; Febvre, P.; Lesueur, J.; Bergeal, N. *Supercond. Sci. Technol.* **2018,** *31,* 035003. doi:10.1088/1361-6668/aa9d48
30. Glushkov, E. I.; Chiginev, A. V.; Kuzmin, L. S.; Revin, L. S. *Beilstein J. Nanotechnol.* **2022,** *13,* 325–333. doi:10.3762/bjnano.13.27
31. Knirck, S.; Hoshino, G.; Awida, M. H.; Cancelo, G. I.; Di Federico, M.; Knepper, B.; Lapuente, A.; Littmann, M.; Miller, D. W.; Mitchell, D. V.; Rodriguez, D.; Ruschman, M. K.; Sawtell, M. A.; Stefanazzi, L.; Sonnenschein, A.; Teafoe, G. W.; Bowring, D.; Carosi, G.; Chou, A.; Chang, C. L.; Dona, K.; Khatiwada, R.; Kurinsky, N. A.; Liu, J.; Pena, C.; Salemi, C. P.; Wang, C. W.; Yu, J. *Phys. Rev. Lett.* **2024,** *132,* 131004. doi:10.1103/physrevlett.132.131004
32. Hoshino, G.; Knirck, S.; Awida, M. H.; Cancelo, G. I.; Corrodi, S.; Di Federico, M.; Knepper, B.; Lapuente, A.; Littmann, M.; Miller, D. W.; Mitchell, D. V.; Rodriguez, D.; Ruschman, M. K.; Salemi, C. P.; Sawtell, M. A.; Stefanazzi, L.; Sonnenschein, A.; Teafoe, G. W.; Winter, P. *Phys. Rev. Lett.* **2025,** *134,* 171002. doi:10.1103/physrevlett.134.171002

License and Terms

The definitive version of this article is the electronic one which can be found at:
https://doi.org/10.3762/bjnano.16.152